Microfluidic evaporation, pervaporation and osmosis: from passive pumping to solute concentration

Patrice Bacchin,[†] Jacques Leng,[‡] and Jean-Baptiste Salmon[*,‡]

[†]*Laboratoire de Génie Chimique, Université de Toulouse, CNRS, INPT, UPS, 31000 Toulouse, France.*
[‡]*CNRS, Solvay, LOF, UMR 5258, Université de Bordeaux, 33600 Pessac, France.*

E-mail: jean-baptiste.salmon-exterieur@solvay.com

Abstract

Evaporation, pervaporation, and forward osmosis are processes leading to a mass transfer of solvent across an interface: gas/liquid for evaporation and solid/liquid (membrane) for pervaporation and osmosis. This review provides comprehensive insight into the use of these processes at the microfluidic scales for applications ranging from passive pumping to the screening of phase diagrams and micromaterials engineering. Indeed, for a fixed interface relative to the microfluidic chip, these processes *passively* induce flows driven only by gradients of chemical potential. As a consequence, these passive-transport phenomena lead to an accumulation of solutes that cannot cross the interface and thus concentrate solutions in the microfluidic chip up to high concentration regimes, possibly up to solidification. The purpose of this review is to provide a unified description of these processes and associated microfluidic applications to highlight the differences and similarities between these three passive-transport phenomena.

Contents

1 Introduction

The term *microfluidics* generally refers to the science and toolbox for manipulating fluids in networks of microfabricated channels with cross-sectional dimensions ranging from a few microns to a few hundred microns.[1] The first microfluidic technologies emerged in the 1990s, motivated in particular by the development of miniaturized analysis systems, the concept of *micro total analysis systems* (μTAS).[2] Over the past 20 years, research aimed at developing original microfluidic systems and their use for both fundamental science and advanced applications has blossomed, and there is now a lot of proofs of concept and tangible applications, particularly in biology, chemistry and material science. As an example, the Web Of Science database currently lists nearly 60 000 articles with the word *microfluidic* in their topic. We refer the reader to a short list of reviews[3–11] that provide an overview of different aspects of this vast scientific and technological field.

The benefits of miniaturization go far beyond handling very small volumes of liquid (fL–μL) which is nonetheless particularly relevant for biochemical applications; indeed, typical microfluidic length scales (1–100 μm) offer an unequaled control of the transport phenomena (mass, momentum, and energy) mainly because flows are dominated by viscous forces.[12,13] Such a fine control, associated with new phenomena related to the high surface/volume ratio and coupled with local measurements, permits a fresh look on many physicochemical and chemical engineering issues. In this context, the present review aims to demonstrate how the microfluidic toolbox combined with evaporation, pervaporation, and osmosis processes enables applications as diverse as passive pumping and solute concentration, or even the engineering of advanced micromaterials and the dynamic exploration and manipulation of soft matter systems.

1.1 Passive mass transport

Most microfluidic applications rely on external forces and fields to drive liquid flows inside microchannel networks: pressure sources such as mechanical pumps, electric or magnetic fields, centrifugal forces, acoustic waves, etc.[12] Interestingly, liquid flows can also be passively driven into microfluidic chips, i.e., without the need for external power source, for instance using gravity or capillary action.[14] Among passive-flow mechanisms, those driven by chemical-potential gradients, referred to as *passive mass transport*[15] are key for many phenomena because gradients are ubiquitous in Nature.[16]

Passive mass transport phenomena rely on three essential ingredients that are shown in Figure 1A and commonly encountered in microfluidic experiments:

- solvent molecules present as a liquid or in gas phase, water in the vast majority of cases;
- solutes in the liquid phase, (for simplicity, throughout this review we will use the term *solutes* to describe both dissolved compounds, such as ionic species or macromolecules, and dispersed particles such as colloids); and
- solid materials, such as the walls of the microfluidic channels or a membrane integrated in the chip.

The many combinations within this ternary along with the many possible geometries of microfluidic devices open up various perspectives in terms of passive mass transport. In what follows and for simplicity, we will limit ourselves to isothermal conditions, which are often encountered in microfluidic experiments. As mentioned earlier, liquid flows, and thus mechanical energy, can be passively driven by gradients of chemical potentials. Such gradients can arise from concentration gradients (of solute or solvent) in the liquid phase or in the gas phase, but interfaces also play a key role in locally unbalancing intermolecular interactions.

The interplay of the three ingredients mentioned encompasses the different mechanisms of passive transport in microfluidic systems, as shown in Figure 1B:

- **Capillarity** – The imbalance of molecular interactions at the coexistence of the gas, liquid and solid phases leads to capillary phenomena.[17] Capillarity can be used for example to drive liquid flows in microfluidic devices, such as water spontaneously filling hydrophilic channels as shown in Figure 1B.

- **Marangoni** – A surface tension gradient at a gas/liquid or liquid/liquid interface induces flow along the interface toward the high surface tension, due to the interfacial stresses.[17] Under isothermal conditions, these Marangoni flows are usually observed with amphiphilic solutes adsorbed at interfaces, and play an important role in two-phase flow microfluidics where liquid interfaces are ubiquituous.[18]

- **Diffusion** – In a liquid, a solute concentration gradient induces a flux of solute

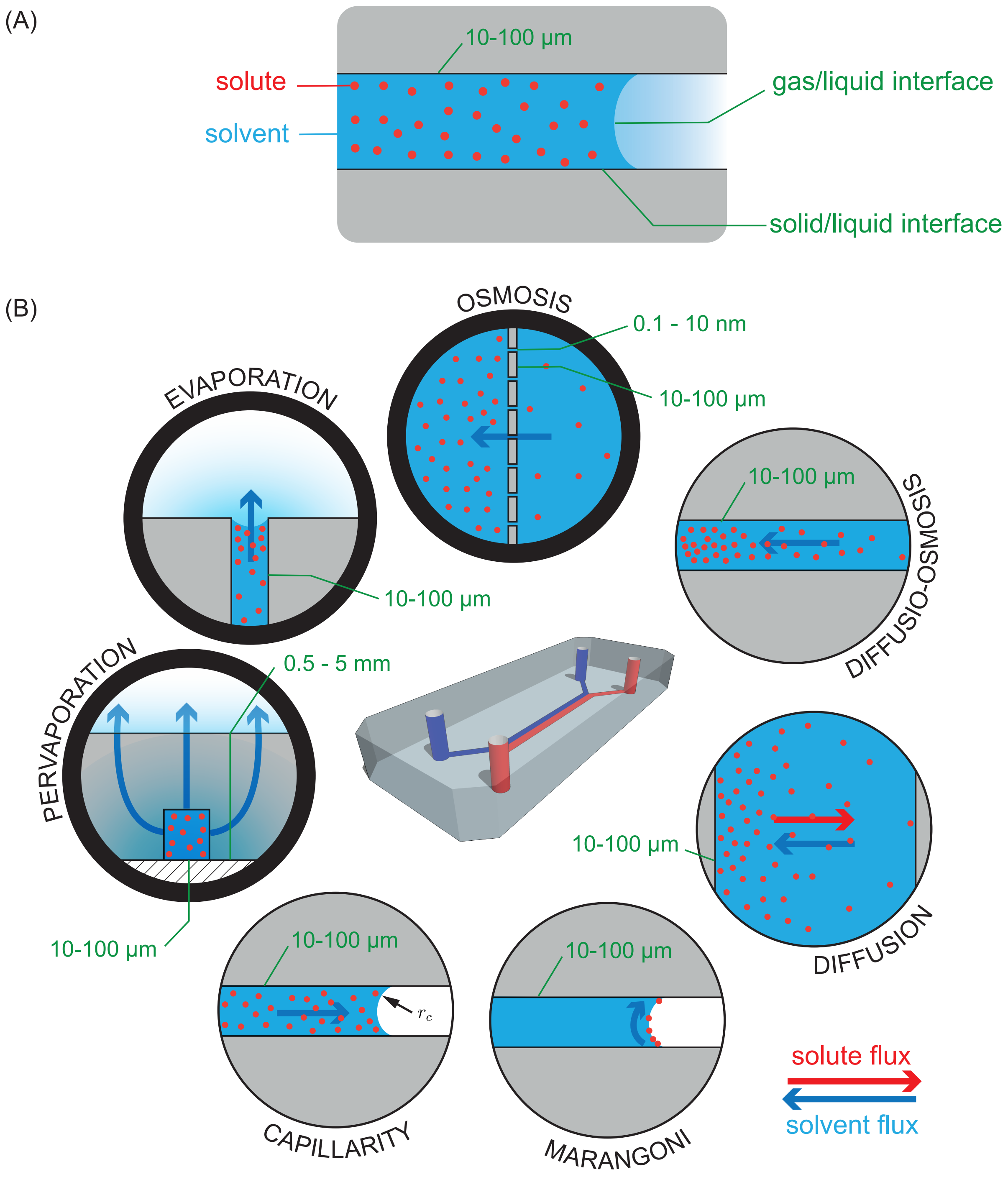

Figure 1: (A) Key ingredients for mass transport phenomena and typical scales of a microfluidic channel. (B) Passive mass transport in microfluidic devices. Only evaporation, pervaporation, and osmosis will be considered in this review. These processes result in a mass transport of solvent through a *physical* interface, which can thus be exploited, among other things, to concentrate the solutes in the liquid phase. In the inset corresponding to capillarity, r_c is the radius of curvature of the interface.

driven by thermal motion, from high to low concentrations. However, this flux is associated to an opposite flux of solvent to ensure the volume continuity, and the liquid remains at rest.[19–22] Molecular diffusion plays a key role in microfluidic systems, particularly because transport by advection is limited by viscous flows at these small scales.[12,13]

- **Diffusio-osmosis** – In the case of the ternary solute/solvent/solid, a solute concentration gradient can induce a solvent flux due to interactions between the solute and the liquid/solid interface, the so-called diffusio-osmosis phenomenon.[23] For neutral solutes having a repulsive interaction with a solid material, the solvent flux is directed toward the high solute concentration, as shown in Figure 1B with a steady solute gradient along a channel. This interfacially-driven transport plays a particularly important role in colloid transport,[24] in an inverted configuration (diffusio-phoresis): the surface of the colloids corresponding to the walls of the channel in the microfluidic case.

- **Osmosis** – Such passive mass transport, precisely called forward osmosis, corresponds to a solvent flux through a semipermeable membrane, induced by a difference in the concentration of solutes. Osmosis comes from the difference in interactions with the membrane between solute and solvent, the interactions between the solute and the membrane being *more repulsive* than for the solvent.[25] Osmotic flows can be observed in any microfluidic system integrating a semipermeable membrane. If the membrane is porous, forward osmosis can be seen as a macroscopic consequence of diffusio-osmosis at the pore scale.[26,27]

- **Evaporation** – A vapor gradient over a gas/liquid interface induces a flow of solvent in the liquid phase to balance the flux of vapor when the interface is held fixed. The example shown in Figure 1B corresponds to a fixed air/solvent meniscus trapped by capillary forces at the outlet of a microfluidic chip. Evaporation in ambient air induces a flow of liquid in the channel.

- **Pervaporation** – Likewise, pervaporation describes the transport of molecules from a liquid which dissolve in a solid material, diffuse through it and evaporate into the external gas phase.[28] In the case shown in Figure 1B, since the microfluidic chip matrix is assumed to be permeable to solvent, pervaporation of solvent molecules induces a liquid flow in the channel.

As we will show throughout this review, the mechanisms listed here can occur simultaneously and lead to complex interactions because interfaces and concentration gradients are omnipresent at the microfluidic scale.

1.2 Scope of this review

Except for diffusion in a liquid, Figure 1B shows that gradients in concentration in either a gas, liquid, or solid phase can be used to passively induce a solvent flux through a *physical* and *fixed* interface, relative to the microfluidic chip. These configurations correspond to *evaporation* for a fixed gas/liquid interface, *pervaporation* across a solid material separating a liquid from a gas phase, and *forward osmosis* across a membrane separating two liquid phases. This review will focus specifically on these three processes, as they can be used not only to passively pump liquids into microfluidic chips but also to concentrate solutes when they are retained by the interface, see Figure 2. Although we focus primarily on evaporation, pervaporation and osmosis, we will see throughout the review that other passive transport mechanisms, more particularly diffusion, capillarity, and diffusio-osmosis can also play a role in these processes.

In section 2, we will first underline and explain the key role played by the interfaces for evaporation, pervaporation, and forward osmosis, and then give some theoretical elements to describe quantitatively these passive transport phenomena. Section 3 will then show how these processes have been used to passively pump liquids, as shown schematically in Figure 2A, mainly for applications that require low yet stable and nonpulsating flow rates. Section 4 will then show how these processes have been har-

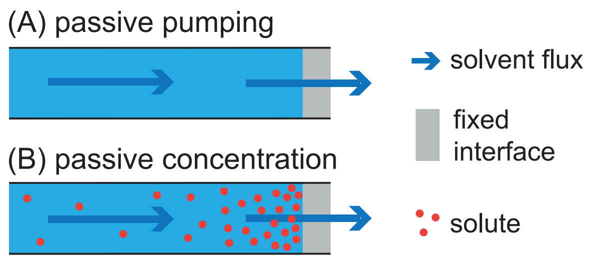

Figure 2: Schematic framework of the present review regarding (A) pumping and (B) solute accumulation in microfluidic chips. The solvent flux is passively driven through a fixed and physical interface, gas/liquid in the case of evaporation, and solid/liquid in the cases of pervaporation and osmosis.

nessed to passively concentrate solutes in microfluidic chips, as shown schematically in Figure 2B. These solutes can be nonvolatile species in the case of evaporation, or solutes fully rejected by the membrane in the cases of osmosis and pervaporation. Section 4 will not only highlight the similarities between these phenomena in different microfluidic geometries, but also present the associated applications, from preconcentration of analytes to phase diagram screening, or even micromaterial fabrication.

2 Evaporation, pervaporation, and osmosis at the microfluidic scale

2.1 Interfaces and microfluidics

Figure 1 shows that interfaces play a particularly important role for the passive transport phenomena considered in this review: gas/liquid interfaces for evaporation and solid/liquid interfaces for pervaporation and osmosis. Because microfluidics are made up of networks of channels of small transverse dimensions, $\sim 10\ \mu$m, within chips of a few cm^2, the surface/volume ratios are high and thus can bring a significant enhancement of these transport phenomena. As shown in Figure 1, two main categories of interfaces are relevant for these three processes in microfluidic systems: interfaces that delimit a volume of fluid and membranes integrated in the chip that separate fluids.

2.1.1 Interfaces delimiting the volume of the fluid

Microfluidics deals with the manipulation of liquids in microfabricated channels in solid materials, so solid/liquid interfaces are intrinsically important. Figure 1B shows that these interfaces play a key role for evaporation to fix gas/liquid interfaces by capillary action but also for pervaporation when the solid matrix is permeable to solvent molecules. In the latter case, the solid/liquid interface that delimits the fluid volume also acts as a membrane.

Likewise, most microfluidic applications involve gas/liquid interfaces that delimit the liquid volume. Figure 1B shows, for example, the cases of a meniscus pinned at the outlet of a microfluidic chip and that of a meniscus moving under the action of capillary forces in a channel. In these examples, the gas/liquid interface is limited to the transverse dimensions of the microchannel, but there are many other cases for which these interfaces reach the chip dimensions, namely a few cm×cm: paper-based microfluidic chips,[11] microchannels sealed by microporous hydrophobic membranes,[29] etc. We will come back to these cases in detail, as solvent evaporation inevitably occurs from these interfaces.

Gas/liquid and liquid/liquid interfaces can also be used to compartmentalize liquids using two-phase flow microfluidics (droplet microfluidics and segmented gas/liquid flows), see for example the following nonexhaustive list of reviews.[5,6,9,30,31] However, because this review only focuses on passive mass transport phenomena (and their application) through *fixed* interfaces with respect to the microfluidic chip, we will not devote a prominent place to two-phase flow microfluidics.

2.1.2 Membranes and microfluidics

By definition, a membrane is a physical barrier, often solid, that some species can cross more easily than others because of different physicochemical properties. Such physical barriers constitute the fixed interfaces for pervaporation and osmosis, but membranes are also essential for evaporation as in the case of a hydrophobic membrane that can retain liquid water and remain permeable to vapor through its pores. In the following, we will focus on artificial (also called synthetic) membranes and will not consider biological membranes such as cell or tissue membranes, which also play an essential role in many current microfluidic fields of investigation, including organs-on-chips,[32–34] microfluidic generation of unilamellar lipid vesicles,[35,36] etc.

The integration of artificial membranes into chips makes it possible to combine the wide range of applications of membrane processes with the many possibilities offered by the microfluidic toolbox. Because of their functionalities, membranes provide various applications such as separation of chemicals, gas/liquid exchanges (contactors), dialysis (i.e., separation of solutes in a liquid phase by means of their unequal transport through a membrane), emulsification, catalytic reactions, cells culture, energy recovery, etc.[37] Semipermeable membranes, which fully retain solutes while allowing solvent to pass through, will play a major role in what follows, as they allow solutes to be concentrated in a microfluidic chip, from ions to colloidal species depending on the membrane.

In 2001, Wang et al. provided one of the first reviews on the use of membranes in microfluidic chips, mainly focused on bioanalytical applications.[38] A few years later, de Jong et al. provided a comprehensive review concerning membranes and microfluidics, written from the membrane science point of view.[39] As mentioned by de Jong et al., two main classes of membranes can be distinguished among the various membrane processes: dense vs porous membranes.

Dense vs porous membranes – Dense membranes are used to transport selectively single molecules, and play an important role for pervaporation, as well as reverse osmosis and dialysis. For these membranes, molecular transport is due to both dissolution of molecules in the membrane and their diffusion through it. Selectivity results from the differences in affinity of the membrane material with the molecular species (solubility) and the differences regarding their diffusivity. Transport mechanisms in such membranes are generally described by the solution-diffusion model.[40,41]

Porous membranes, on the other hand, have fixed pores with sizes ranging from a nanometer to a few microns, through which solvent or solutes can be transported. Selectivity does not rely at first order on specific molecular interactions but rather on long-range or steric interactions (electrostatic repulsions and exclusion by size). Membrane morphology (e.g., pore size distribution and tortuosity) and surface charges are thus critical, and transport mechanisms are generally modeled using convection-diffusion models possibly including electrokinetic phenomena, with a partition coefficient to account for the selective interaction.[42,43]

Although the distinction between porous and dense membranes is commonly used in the field of membrane science, it becomes fuzzy as soon as the size of the rejected solutes reaches the nanometer range. In all cases, the selectivity mechanisms are always due to selective interactions between solutes and the membrane material which are accounted for in the transport models by solubility or partition coefficients, leading to possibly similar equations for porous and dense membranes. We refer the reader to ref[40] for more insights into the transition occurring in the nanofiltration range between pore-flow models and solution-diffusion mechanisms, possibly related to the lifetime of the free-volume elements (pores) that exist in the membrane.

Membrane materials – For most applications, polymers are the largest family of membrane materials. For instance, this is the case for polyamide thin films obtained by interfacial polymerization, mainly for desalination by reverse osmosis,[44] cellulose acetate,[45] polysulfone or sulfonated polysulfone[46] prepared by phase inversion techniques to allow a microstructure for porous membranes used in dialysis, nano-, ultra- or microfiltration.[47] Pervaporation membranes are also often made from polymers with different chemical affinities depending on the application; hydrophilic polymers such as poly(vinyl alcohol) are used for solvent dehydration,[48] or hydrophobic polymers such as poly(dimethylsiloxane) (PDMS) or polyamide/polyether block copolymers are used for the removal of organic compounds from water or separation in organic mixtures.[49]

The more recent development of inorganic membranes (silica, metal-organic framework, etc.), hybrid mixed-matrix membranes (inorganic fillers in a polymeric matrix), and membranes made of two-dimensional materials such as graphene oxide, also opens very promising prospects in terms of separation efficiency and permeability, see e.g., the recent reviews[48,49] focused on pervaporation. Likewise, biomimetic membranes integrating either biological water channel proteins or artificial water channels (e.g., carbon nanotubes) are paving the way for unprecedented performance in permeability and selectivity, especially for water purification and energy conversion (see e.g., refs[27,50–52]), but they still face the problem of large-scale and defect-free production.[53]

Membrane integration – Since the advent of microfluidic technologies, the integration of membranes into chips has quickly become a major technological challenge, and only a few solutions exist to date.[39] The first approach, and probably the simplest, is when the material of the chip itself constitutes a membrane. This case is commonly observed with polymeric materials that sometimes present high permeability for some organic solvents, but also a nonzero permeability for water. In this review, PDMS plays a key role because this material allows rapid prototyping of microfluidic chips using soft lithography,[54] and also because PDMS is slightly permeable to water and retains a wide range of solutes, such as most salts, polymers, and biomolecules.[55] In what follows, PDMS thus acts as a semipermeable membrane for water, an unusual role for this hydrophobic material that is often used for the removal of trace organic compounds from water in large-scale pervaporation processes.[28] The case described in Figure 1B in which water passes through a PDMS chip, retaining solutes in the channel, may thus lead to confusion with conventional pervaporation processes, but we will nonetheless use the term pervaporation throughout this review to describe this configuration.

The second membrane integration technique consists of a mechanical clamping or chemical bonding of a membrane (often commercial), between two layers containing microchannels.[38,39] Chemical bonding can be achieved by surface treatments of the chip and the membrane leading to the formation of covalent bonds (plasma activation, silanization, etc.), or by means of a third layer, such as a simple double-sided adhesive that was previously cut. Even though there are commercial chips that use mechanical clamping, this technique, which seems simple at first glance, remains delicate with a problem of recurring leaks. In addition, most membranes are not perfectly transparent, thus preventing the use of accurate monitoring techniques such as transmission microscopy.

An elegant alternative consists of the *in situ* fabrication of membranes; it overcomes most of the difficulties because membranes can be integrated into the transverse dimensions of the microchannels. Such methods are mainly based on spatially-resolved photopolymerization or interfacial polymerization, and we again refer the reader to the review of de Jong et al. for more details.[39] Since that review, other groups have published reviews concerning membranes and microfluidics, see in particular refs[56,57] which are mainly oriented toward chemical and bioanalytical applications, ref[58] which concerns membrane filtration and points out the specific challenges related to on-chip nanofiltration and reverse osmosis, and ref[59] for a comprehensive and up-to-date review of membrane integration techniques into PDMS-free chips.

Toward nanofluidics – In recent years, the development of nanofluidics has made it possible to manipulate flows in submicron geometries of controlled architecture.[60] These fascinating tools now allow one to revisit membrane processes at the nanopore scale, thus opening the way to innovations, notably concerning water treatment or energy harvesting.[61–64] Again, the present review focuses on mass transport in microfluidic systems, passively driven by evaporation, pervaporation or osmosis, for applications ranging from passive pumping to solute accumulation (Figure 2), and we will not describe nanofluidics but instead keep it as an expected perspective.

2.2 Driving force and kinetic models

2.2.1 The driving force

Figure 1B shows that gradients of concentration are essential for passive mass transport: gradient of vapor for evaporation, solvent concentration gradient in a dense material for pervaporation, and solute concentration difference across a membrane for forward osmosis. As demonstrated earlier by Eijkel and van den Berg in a tutorial review,[65] a convenient way to describe flows in microfluidic systems, including these passive transport phenomena, is to use the concept of solvent chemical potential μ. Because water is the solvent in the vast majority of applications, only the water potential Ψ will be considered here without loss of generality. We choose the following definition of the water potential Ψ (Pa):

$$\Psi = \frac{\mu - \mu_0(T)}{V_m}\,, \tag{1}$$

where $\mu = \mu(P,T)$ is the water chemical potential expressed in units of J/mol at pressure P (Pa) and absolute temperature T (K), $\mu_0(T)$ is its standard value at atmospheric pressure P_0 and sea level, and $V_m(P,T)$ is the liquid water molar volume ($V_m \simeq 1.8 \times 10^{-5}$ m^3/mol at P_0 and room temperature).

This definition of Ψ with pressure as the unit allows a unified description of any water fluxes in a microfluidic system, independently of the thermodynamic state of water: pure liquid, solution or vapor.[65] As this quantity encompasses the different contributions that generate flows, including hydrostatic pressure, capillary action, evaporation, pervaporation, osmosis, etc., water potential is thus widely used in the plant science and membrane science communities.[66]

In the pure liquid state, the molar volume is almost independent of pressure, and the water potential is given by:

$$\Psi_l = \rho_w g(h - h_0) + P - P_0\,. \tag{2}$$

The first term corresponds to the contribution of gravity, with ρ_w being the density of water (kg/m^3), g being the acceleration due to gravity (m/s^2), and h being the height above sea level at height h_0.

For aqueous solutions, entropy also contributes to the free energy of water, and the water potential is given by:

$$\Psi_{\text{ent}} = -\Pi = \frac{RT}{V_m}\ln(a_w)\,, \tag{3}$$

where Π is the osmotic pressure of the solution, a_w is the water chemical activity and R is the universal gas constant. For a dilute aqueous solution at a concentration C (mol/m^3), $a_w \simeq 1 - V_m C$, so that $\Psi = -\Pi \simeq -RTC$. As mentioned in section 1.1, a solute concentration gradient in an aqueous solution, and thus a gradient of the entropic contribution Ψ_{ent}, does not lead to an overall liquid flow, as the water flux is compensated by a solute flux to ensure the volume continuity of the mixture.[19–22] It is no longer the case when there is a barrier to diffusion, such as a semipermeable membrane, which then leads to a net water flux by osmosis.[27] For aqueous solutions in a microfluidic chip, these contributions add up, so the water potential is often written as:[65]

$$\Psi = \rho_w g(h - h_0) + P - P_0 - \Pi\,. \tag{4}$$

As shown in Figure 1, the microfluidic systems are also in contact with a gas phase in most cases, so that one should also consider a possible water transport between the chip and its surroundings. The water potential in the gas phase, considered as a perfect gas, is given by:

$$\Psi_{\text{vap}} = \frac{RT}{V_m}\ln\left(\frac{p}{p_{\text{sat}}}\right) = \frac{RT}{V_m}\ln(\text{RH})\,, \tag{5}$$

with p being the water partial pressure in the gas phase (Pa), p_{sat} being its value at saturation, and $\mathrm{RH} = p/p_{\mathrm{sat}}$ (RH = the relative humidity).

Finally, when air/liquid interfaces are present, the molecular interactions with the walls, either hydrophilic or hydrophobic, also modify the hydrostatic water pressure P, which is mechanically balanced by the curvature of interfaces. In the case of a liquid water slug confined in a cylindrical capillary with hydrophilic walls such as in Figure 1B, the pressure drop ΔP across the interface (liquid pressure minus exterior pressure) is given by the Young-Laplace law:

$$\Psi_{\mathrm{cap}} = \Delta P = -\frac{2\gamma}{r_c}\,, \tag{6}$$

with $\gamma \simeq 0.07$ N/m being the water/air surface tension, $r_c \geq 0$ being the radius of curvature of the interfaces as defined in Figure 1B, and Ψ_{cap} being the corresponding contribution to the water potential due to capillarity according to the notation of the didactic review by Eijkel and van den Berg.[65]

Similarly to ref,[65] Table 1 displays the order of magnitude of the different contributions of the water potential for the liquid phase as given in eq 4, the corresponding RH for Ψ_{vap} given by eq 5, and r_c for the capillary contribution given by eq 6. We refer the reader to ref[65] for a more detailed discussion, including in particular the case of adsorbed water in thin films, which is essential for describing nanofluidic systems.

The driving force of water flux in a microfluidic system including its surroundings is given by any difference of water potential $\Delta\Psi$, and the water flux is always directed from a high water potential to a lower one. Table 1 allows one to estimate the sign of the driving force $\Delta\Psi$ and thus the direction of the water flux. For example, evaporation or pervaporation inevitably occurs for pure water in microfluidic chip when the latter is placed in a typical laboratory atmosphere, because $\Delta\Psi \simeq -(RT/V_m)\ln(\mathrm{RH}) \gg 0$. This remains true even for a saturated aqueous solution of sodium chloride in relative humidity RH $< 75\%$, as its water chemical activity is $a_w \simeq 0.75$ ($\Psi \simeq -40$ MPa at room temperature).[67] Note that the magnitude of this passive transport also depends on the resistance to mass transfer, and fortunately pervaporation and evaporation can often be neglected in most microfluidic configurations, despite the possibly high values of $\Delta\Psi$.[65]

We will make use of Table 1 throughout this review, in particular for evaluating the impact of capillary phenomena on evaporation in microfluidic chips, section 3.1, or to compare the mechanisms of solute accumulation induced by evaporation, pervaporation or osmosis in section 4.

2.2.2 Simplified 1D kinetic models

The knowledge of the driving force $\Delta\Psi$ alone does not allow one predict the intensity of the mass transport, which can only be done by a kinetic description in the framework of nonequilibrium thermodynamics[21] of the phenomena of evaporation, pervaporation and osmosis for a given geometrical configuration. To address this point and highlight the similarities between these three processes, we consider the 1D geometry shown in Figure 3, similarly to the configuration shown in Figure 2. In each case, evaporation, pervaporation, and forward osmosis, we assume that there is a flat, homogeneous interface through which a steady mass solvent flux $\rho_w J$ [kg/(m^{2}s)] is driven by a drop in the water potential, $\Delta\Psi$.

Again, we emphasize that we only consider in this review fixed interfaces relative to the microfluidic chip, and we will address in section 3.1 what this point implies as constraints in the case of a gas/liquid interface and evaporation. We assume local thermodynamic equilibrium and the continuity of the water potential Ψ, and we simplify the general context by assuming isothermal conditions and binary liquid mixtures (solvent + solute), with the solute being unable to cross the interface.

Evaporation – In the simplified picture shown in Figure 3A for evaporation in ambient air, the water potential $\Psi^\star$ in the liquid phase at the interface, eq 4, sets the local water potential in the gas phase, eq 5, and thus the local relative humidity. In this 1D model, the

Table 1: Water potential Ψ and corresponding values of the relative height for the contribution due to gravity, eq 2, of the radius of curvature r_c for the capillary contribution given by eq 6, and of the chemical activity a_w for the entropic contribution, eq 3. The fifth column shows the corresponding solute concentration $C \simeq -\Psi/(RT)$ only valid for dilute solutions. The last column shows the corresponding relative humidity RH in the gas phase eq 5 ($T = 22°\text{C}$).

Ψ (MPa)	$h - h_0$	r_c	a_w	C	RH
0	0 m	∞	1	0	100%
-0.01	-1 m	14 μm	0.9999	4 mM	99.99%
-0.1	-10 m	1.4 μm	0.999	40 mM	99.9%
-1	-100 m	140 nm	0.993	0.4 M	99.3%
-10	-1 km	14 nm	0.93	4 M	93%
-40	-4 km	3.5 nm	0.75	n/a	75%
-100	-10 km	1.4 nm	0.48	n/a	48%
-200	-20 km	0.7 nm	0.23	n/a	23%
-400	-40 km	0.35 nm	0.05	n/a	5%

water potential is dominated by its entropic contribution (see eq 4 and Table 1). Therefore, it is the water chemical activity at the interface $a_w^\star$ that sets the local partial vapor pressure, and the water concentration in the gas phase $c^\star = a_w^\star c_{\text{sat}}$, with $c_{\text{sat}} = M_w p_{\text{sat}}/(RT)$ (kg/m^3) being its value at saturation with M_w being the molar mass of water (kg/mol). Far from the interface, the vapor concentration in the ambient air is $c_\infty = \text{RH}c_{\text{sat}}$, which results in a concentration gradient of water molecules in the gas. This concentration gradient is associated with a solvent flux in the gas phase, which leads to a solvent mass flux across the gas/liquid interface due to mass conservation. For slightly volatile solvents such as water, this flux is given by:

$$\rho_w J = k c_{\text{sat}}(a_w^\star - \text{RH}) \tag{7}$$

where J (m/s) is the water flux in the liquid phase, and k (m/s) a mass transfer coefficient that accounts for the mechanisms of the transport of the vapor in the gas phase.[19] In the case of diffusive transport across a boundary layer of thickness λ, $k = D_w^{\text{air}}/\lambda$ where D_w^{air} is the diffusion coefficient of water as vapor in the gas phase.[19]

Pervaporation – Figure 3B shows the steady case of pervaporation across a dense membrane of thickness δ. For this process, the mechanisms are described by the solution-diffusion model,[40,41] and the solvent flux results from a three-step process: (i) dissolution of water molecules in the membrane from the liquid phase (feed side) (ii) diffusion across the membrane, and (iii) evaporation in the gas phase (permeate side). Importantly, molecular absorption and desorption from both sides of the membrane are implicitly assumed not to be limiting steps.[40] Henry's law as a guide for the water sorption in the membrane shows that there exists a concentration discontinuity at the membrane/gas interface (permeate side): the water concentration in the membrane is $\text{RH}c_{\text{sat}}^p$ where c_{sat}^p (kg/m^3) is the concentration at saturation in the membrane and RH the relative humidity in the gas phase (p denotes water concentration in the pervaporation membrane). The water concentration difference across the membrane is thus $c_{\text{sat}}^p(a_w^\star - \text{RH})$, where $a_w^\star$ is the water chemical activity in the liquid phase at the interface (feed side); again, we implicitly assume here that Ψ is dominated by its entropic contribution. For a constant diffusion coefficient D_w^p (m^2/s) of water in the material, the mass solvent flux through the membrane is then given by Fick's law:

$$\rho_w J = \frac{D_w^p c_{\text{sat}}^p}{\delta}(a_w^\star - \text{RH})\,. \tag{8}$$

We refer to refs[40,41] to go beyond the simplified assumptions used earlier.

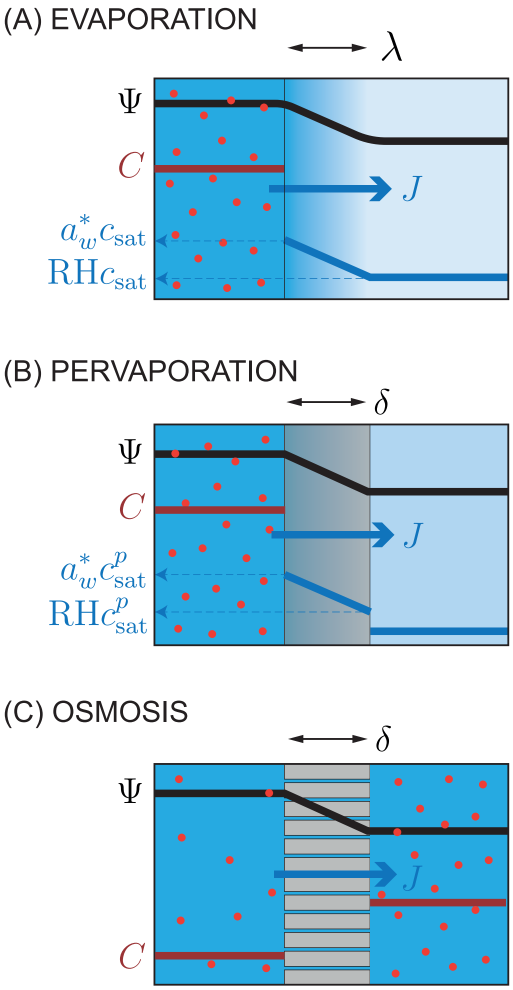

Figure 3: 1D passive mass transport for evaporation (A), pervaporation (B), and osmosis (C). Dark lines show the continuous water potential Ψ, while blue lines show the water concentration c in (A) and (B), and red lines show the solute concentration C.

Forward osmosis – Figure 3C shows the case of osmosis through a membrane separating two aqueous solutions at different concentrations C (mol/m^3). We consider that the solutes, referred to as *osmotic agents*,[25] are totally rejected by the membrane due to repulsive interactions. For this ideal case, the water flux J varies linearly with the difference of water potential $\Delta\Psi$ across the membrane (eq 4), and J is given by the Kedem-Katchalsky equations, which reduce to:

$$J = \mathcal{L}_p(\Delta P - \Delta\Pi)\,, \tag{9}$$

with ΔP being the transmembrane pressure drop, $\Delta\Pi$ being the osmotic pressure difference across the membrane, and $\mathcal{L}_p$ being the membrane permeability [m/(Pa s)][68] (with Δ defined here as upstream minus downstream). As this review focuses on passive transport phenomena, the water potential Ψ is dominated by its entropic contribution so that $\Delta P \ll \Delta\Pi$ (forward osmosis) and eq 9 now reads as follows:

$$J = -\mathcal{L}_p \Delta\Pi\,. \tag{10}$$

The osmotic pressure difference is due to a solute concentration difference ΔC across the membrane with the well-known limit $\Delta\Pi \simeq RT\Delta C$ for dilute solutions. Because the Kedem–Katchalsky model is derived from general arguments in the framework of irreversible processes, it does not describe the molecular mechanisms of membrane transport. For osmosis through dense membranes, the permeability $\mathcal{L}_p$ can then be estimated using the solution-diffusion model described by eq 8. For porous membranes, the permeability $\mathcal{L}_p$ can be estimated using pore-flow or electrokinetic models,[42,43] and we refer the reader to the review of Marbach and Bocquet[27] for more physical insights into osmosis through porous membranes, and in particular its relationship to diffusio-osmosis as mentioned in section 1.1.

Analogy – In the case of forward osmosis and for moderate osmotic pressures verifying $\Pi \ll RT/V_m$ ($\simeq$ 135 MPa at room temperature), eq 3 shows that $\Delta\Pi \simeq -(RT/V_m)\Delta a_w$ with Δa_w being the difference of water chemical activity across the membrane. In this case, the solvent flux given by eq 10 becomes:

$$J = \mathcal{L}_p \frac{RT}{V_m} \Delta a_w\,. \tag{11}$$

Equations 7, 8, and 11 make it possible to highlight the strong analogy between evaporation, pervaporation, and forward osmosis, as the solvent flux J in these three processes is strictly proportional to a difference of water chemical activity Δa_w; it is exactly $\Delta a_w = (a_w^\star - \text{RH})$ in the case of evaporation and pervaporation, with the water flux always being directed from high to low water chemical activity.

2.2.3 Orders of magnitude

For evaporation, pervaporation, and osmosis, the solvent flux J through the interface is proportional to a difference of water chemical activity, but its exact value depends on the mass transport resistance. Below, we estimate typical orders of magnitude of J in experimental cases relevant to this review using the 1D model shown in Figure 3 and described by eqs 7, 8, and 11.

In the case of evaporation and assuming vapor diffusion across a boundary layer of thickness λ ranging from $\lambda = 1$ mm down to 10 μm (typical of microfluidic dimensions, see later Section 3.1), eq 7 yields J ranging from $\simeq 20$ μm/s down to $\simeq 200$ nm/s, respectively, for room temperature conditions ($T = 20$°C and RH $=$ 50%) ($\rho_w \simeq 1000$ kg/m^3, $p_{\text{sat}} \simeq 2.3$ kPa[69] and $D_w^{\text{air}} \simeq 2.5 \times 10^{-5}$ m^2/s[70]).

With respect to pervaporation, PDMS plays a particularly important role because this water-permeable material is the material of many microfluidic chips, and also because soft lithography makes it easy to integrate thin PDMS membranes into microfluidic systems. Assuming as in Figure 3B, a PDMS membrane of thickness δ separating pure water ($a_w = 1$) from ambient air of relative humidity RH $= 50\%$, eq 8 leads to water flux ranging from $J \simeq 35$ down to $\simeq 3.5$ nm/s for thicknesses ranging from $\delta = 10$ to 100 μm ($D_w^p \simeq 10^{-9}$ m^2/s and $c_{\text{sat}}^p \simeq 0.73$ kg/m^3, see section 3.2). For organic solvents that are highly soluble in PDMS, the fluxes estimated by eq 8 can be significantly higher, related to the fact that PDMS is a material of choice for pervaporation membranes to remove organic compounds from water.[28]

Finally, considering forward osmosis through a nanoporous dialysis membrane of typical permeability $\mathcal{L}_p \simeq 2 \times 10^{-12}$ m/(s Pa) separating pure water ($a_w = 1$, equivalently $\Pi = 0$) from a solution of osmotic agents at concentration C ranging from $C = 0.1$ to 1 M ($\Pi \simeq RTC =$ 0.25–2.5 MPa at $T = 22$°C), eq 11 leads to a solvent flux J ranging from $\simeq 0.5$ to $\simeq 5$ μm/s through the membrane.

These fluxes, which are only driven by chemical potential gradients thus range from a few nm/s to a few μm/s, values that can be relevant to many microfluidic systems and applications especially because surface/volume ratios are high. For instance, section 3 demonstrates the benefits of the combination of these processes and miniaturization to passively pump liquids at relatively low flow rates in various applications.

2.2.4 Solute accumulation and resistances to mass transport

A very fruitful consequence of these passively-driven flows is the possibility to concentrate solutes in controlled manner in microfluidic chips, as discussed in depth throughout section 4. For example, Figure 2B illustrates the passive accumulation of solutes upstream of the interface in a microfluidic channel, regardless of the process considered: evaporation, pervaporation, or osmosis.

This accumulation of solutes is associated with the development of a solute concentration gradient in the liquid phase, which, in turn, can add a resistance to mass transfer and impact the solvent flux across the interface.[71] Similarly, the 1D kinetic model shown in Figure 3 does not take into account the presence of concentration gradients downstream of the interface (except obviously for evaporation), also possibly adding resistances to mass transfer. These points are illustrated in Figure 4 showing both local and global views of the 1D processes across flat and homogeneous interfaces.

Downstream resistance – The concentration gradients downstream of the interfaces (on a length scale λ or λ_o, Figure 4) represent a possible resistance to mass transfer: for pervaporation, the humidity in the gas phase in the vicinity of the membrane is higher than the ambient humidity; for forward osmosis, a depletion layer of osmotic agents downstream of the membrane, the so-called external concentration polarization (ECP),[25] reduces the driving force of the osmotic flux in eq 10; and for evapora-

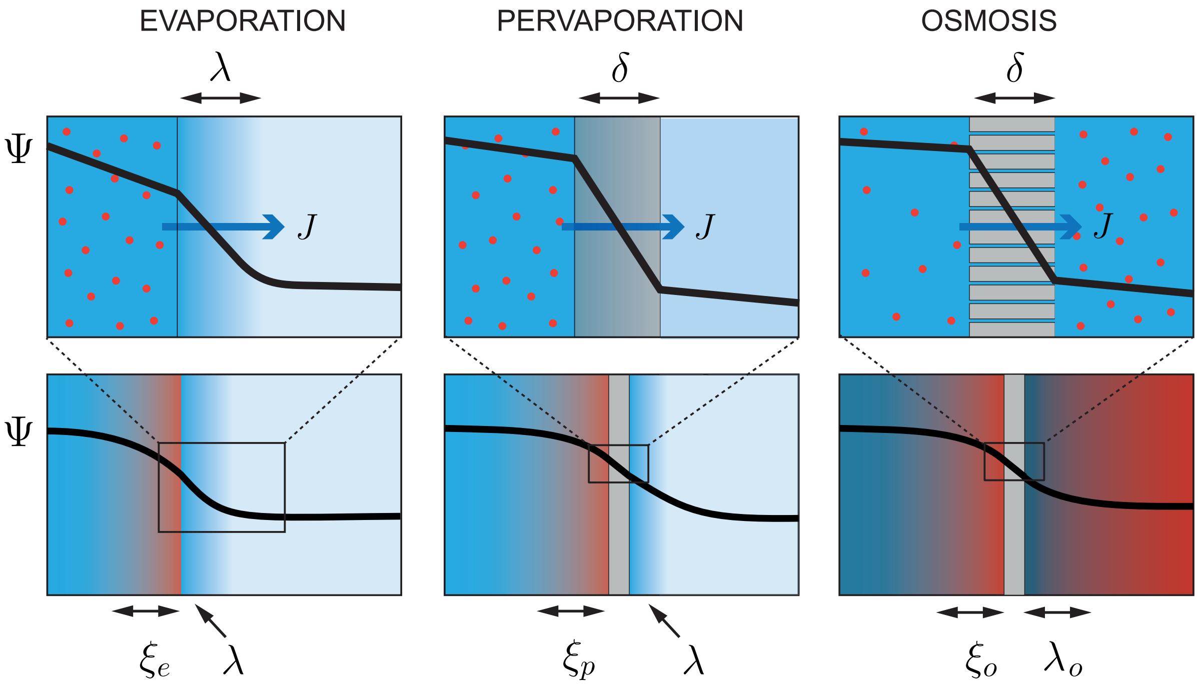

Figure 4: Evaporation, pervaporation, and osmosis seen at two different scales. (Top) A very local scale highlights the local equilibrium and the subsequent solvent flux across the interface due to the drop of water potential Ψ. (Bottom) On a larger scale, concentration gradients upstream and downstream of the interface have an impact on the overall solvent flux. ξ_e, ξ_p, and ξ_o are the extents of the solute concentration gradient upstream of the interface for evaporation, pervaporation, and osmosis, respectively. λ is the extent of the diffuse layer in the gas phase for evaporation and pervaporation, and λ_o is the downstream concentration polarization for osmosis.

tion, it is the vapor gradient in the boundary layer of extent λ that limits the mass transport downstream of the interface in this 1D configuration, see eq 7. The spatial extent λ or λ_o of these gradients depends on the transport conditions in the gas phase for evaporation and pervaporation, and in the liquid phase for osmosis (fluid velocity, geometry, fluid properties). Forced convection downstream of the interface can be used to minimize these resistances and thus maximize the efficiency of these passive transport phenomena. This strategy, which is potentially easy in the cases of evaporation and pervaporation (e.g., air sweeping downstream of the interface), can be difficult in the case of forward osmosis, especially for microfluidics, because viscous forces strongly limit the flows in the liquid phase. We will return to these points specifically when they are relevant to the works listed in this review.

Upstream resistance – The case of an added resistance due to the accumulation of solutes upstream of the interface raises a singular and particularly relevant point that is at the heart of this review (section 4). Equations 7, 8, and 10 show that the increase in solute concentration upstream of the interface decreases the water chemical activity at the interface $a_w^\star$. Table 1 therefore becomes a useful guide to evaluate the possible decrease of the driving force of the solvent flux J. For instance, only solute accumulation significantly decreasing $a_w^\star$ down to the ambient relative humidity RH is able to decrease the driving force for pervaporation and evaporation, see eqs 7 and 8. Meanwhile, it may well happen for (highly soluble) solutes at high concentrations because the chemical activity of a dilute solution at concentration C is $a_w \simeq 1 - V_m C$, it never occurs for dispersions of colloidal hard particles for which $a_w \simeq 1$, regardless of the colloid concentration.[72] This is not the case anymore for forward osmosis, as a significant decrease of the driving force $\Delta\Pi$ can occur even for dilute solutions, depending on the osmotic pressure imposed on the permeate side.

As for the downstream resistance discussed earlier, the extent of the gradient, ξ_e, ξ_p, or ξ_o depending on the process considered as shown in Figure 4, depends on mass transport upstream of the interface and thus in the liquid phase. ξ_e, ξ_p, or ξ_o can thus be determined from the balance between solute diffusion and solute advection by the flows often dominated by viscous forces within the microfluidic chip. In the 1D configurations sketched in Figure 4, for example, ξ_e, ξ_p, and ξ_o are proportional after a transient to $\propto D/J$ for a dilute solution, with D being the diffusion coefficient of the solute; see e.g., refs[73,74] and section 4.5.1 for more detailed discussions. These solute gradients can range from a few cm down to a few μm or less, depending on the magnitude of the flow J, and especially also on the chemical nature of the solute, through the D values. We will return to these points in more detail throughout section 4 and highlight the differences and similarities between the mechanisms of solute accumulation in the microfluidic chip, regardless of the process (evaporation, pervaporation, or osmosis) and the chemical nature of the solutes considered.

3 Microfluidic passive pumping

This section addresses the use of evaporation (section 3.1), pervaporation (section 3.2), and forwards osmosis (section 3.3) for microfluidic pumping applications. It presents not only the mechanisms involved and the specificity due to microfluidic scales but also the associated applications and limitations.

3.1 Evaporation-driven pumping

3.1.1 Simplified view of the mechanisms

Passive evaporation to induce flows in a microfluidic chip has many analogies to water transpiration in vascular plants, as shown in Figure 5A. This mechanism allows plants to remain hydrated while capturing CO_2 from the atmosphere to perform the photosynthesis necessary for their survival.[66,75,76] Water transpiration is at stake in the xylem, a vascular circuit with transverse dimensions from tens to hundreds of microns that connects the roots to the leaves, following the so-called *cohesion-tension theory* which dates back to the end of the 19th century.[77] In this mechanism, the only driving force for transpiration is the evaporation of water from the leaves into the atmosphere, literally pulling water from the soil through the xylem. A particularly astonishing feature is that the water pressure measured in the xylem is negative, typically approximately -2 MPa, with the water thus being in a thermodynamic metastable state with respect to its vapor phase.[66,75,76]

The analogy between water transpiration in plants and evaporation pumping is captured minimally in Figure 5B showing a horizontal and cylindrical microfluidic channel of radius h, the inlet of which is connected to a water tank at atmospheric pressure P_0, and the outlet exposed to the ambient air. As long as the air/water interface remains trapped by capillary forces at the outlet of the channel, the difference between the water potential in the reservoir ($\Psi = 0$) with that imposed in the ambient air (Ψ_{ext}), drives a steady flow at a rate Q (m^3/s) in the channel, whose amplitude depends on the different resistances to mass transfer.

Viscous forces in the channel of hydrodynamic resistance R_h induce a pressure drop in the liquid $\Delta P = \Psi^\star = -R_h Q$, with $\Psi^\star$ being the water potential in the liquid phase at the interface. This pressure drop is mechanically balanced by the curvature of the meniscus given by the Young-Laplace law (eq 6). Continuity of

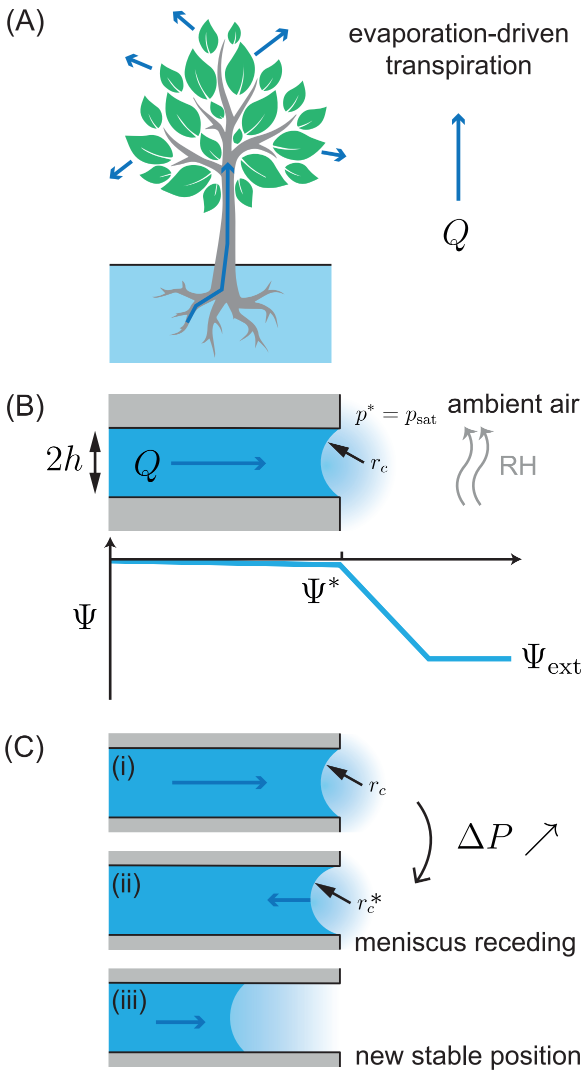

Figure 5: (A) Schematic illustration of water transpiration in plants.[66] (B) Evaporation-induced pumping in a microfluidic capillary of radius h. r_c is the radius of curvature of the meniscus pinned at the outlet. For microfluidic dimensions, the partial vapor pressure close to the interface is almost at saturation $p^\star \simeq p_{\mathrm{sat}}$, and evaporation is limited by the vapor transport in the gas phase. (C) Drying out mechanism. (i) The evaporation-induced pressure drop is mechanically balanced by the curvature r_c of the interface, and the meniscus is trapped by capillarity. (ii) Capillary forces cannot accommodate the strong curvature of the meniscus imposed by a higher pressure drop, and the channel dries out until the meniscus finds a new stable position (iii).

the water potential at the liquid/gas interface (local equilibrium) makes it possible to relate the radius of curvature r_c to the partial vapor pressure $p^\star$ in the gas phase given by eq 5, the so-called Kelvin-Laplace equation:

$$\Psi^\star = -\frac{2\gamma}{r_c} = \frac{RT}{V_m} \ln\left(\frac{p^\star}{p_{\mathrm{sat}}}\right) . \qquad (12)$$

In most microfluidic cases, h ranges from a few hundred to a few microns and $r_c \gg 10$ nm, so that the local partial vapor pressure in the gas phase is almost at saturation, $p^\star \simeq p_{\mathrm{sat}}$ (see also Table 1). The evaporation-driven flow rate Q in this case is therefore limited by the transport of the vapour in the gas phase, and is given by:

$$\rho_w Q = \pi h^2 k \, c_{\mathrm{sat}} (1 - \mathrm{RH}) , \qquad (13)$$

similarly to eq 7 derived in section 2.2.2 for the 1D model shown in Figure 3A with $a_w^\star = 1$. For diffusion-limited transport in the gas phase, $k \simeq 4D_w^{\mathrm{air}}/(\pi h)$ for a flat meniscus,[78] with D_w^{air} the diffusion coefficient of water in air. For RH $= 50\%$ at $T = 22$°C, Q is on the order of a few nL/min for radii h ranging from 10 to 50 μm.

For high hydrodynamic resistances R_h or high flow rates Q, the capillary forces may no longer allow the pinning of the interface, as the curvature radius r_c reaches a critical value $r_c^\star$ of the order of the channel transverse dimension, $r_c^\star \propto h$. In that case, the air/water interface recedes, the channel begins to dry out, and the pumping mechanism stops until the meniscus again finds a mechanically stable position, as shown in Figure 5C. Similar mechanisms are at the basis of the phenomenology of the drying of porous media,[79] see in particular the paper by Chauvet et al.[80] showing an analogy between the drying of a porous medium and that of a single capillary with a square section. We will return in section 3.1.4 to the criteria for avoiding the receding of the meniscus and thus making the most of passive evaporative pumping.

3.1.2 Passive pumping in a single microfluidic channel

The first experimental realization of evaporation pumping as shown in Figure 5B for a single microchannel was reported in 2000 by Namasivayam et al. for studies on stretching DNA molecules that require both nonpulsating flows and low velocities (≤ 50 μm/s).[81] In this work, the air/water interface is trapped by a hydrophobic micropatch at a given location in a silicon-glass microchannel (height $h \simeq 50$ μm) as shown in Figure 6. Evaporation-induced flow rates Q of a few nL/min were reported, in accordance with the estimates given by eq 13. Importantly, the control of the evaporation conditions offered by the microfluidic scale, notably imposing a fixed distance between the liquid/gas interface and an air flow in the chip, makes it possible to quantitatively predict Q by modeling the vapor transport in the gas phase.[82]

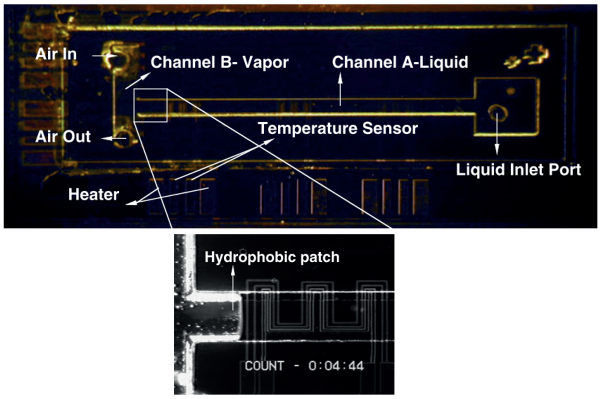

Figure 6: Evaporative pumping in a single microfluidic channel. The meniscus is trapped using a hydrophobic patch at a fixed distance from an air stream. Adapted with permission from ref.[82] Copyright 2003 Institute of Physics Publishing.

At almost the same time, evaporation-driven chromatography was demonstrated using electrokinetic sample injection in microfluidic channels.[83] Interestingly, this work shows that the outlets of a glass microfluidic chip also allow the air/water menisci to be trapped, as shown in Figure 1B and 5B, without the need for built-in hydrophobic patches.

The schematic representation of passive evaporation-driven pumping given in Figure 5B is also relevant for any microfluidic device based on capillary phenomena to move and process small quantities of liquids.[14] In the case of capillary pumps[87] (see Figure 7 for examples), the flow is induced by the capillary pressure difference at the curved air/liquid menisci at the inlet and outlet, but evaporation-induced flows also play a role, in particular once the mechanical balance is reached.[84,88–90] These flows often cannot be neglected owing to the high surface/volume ratios and the small volumes involved, often submicroliter in microscale assays.[91,92] Precise control of the microfluidic geometries (including those of the reservoirs connected to the chip) allows a quantitative description of these flows by numerical modeling of solvent evaporation (assuming vapor diffusion) from the interfaces whose shapes are controlled by capillarity[85,86] (Figure 7B). The accuracy and stability of these flows at very low flow rates ($Q \simeq$ 1-10 nL/min), however,

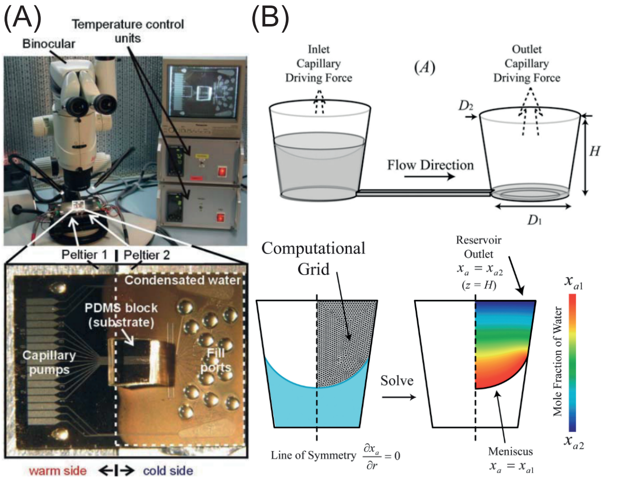

Figure 7: Evaporation and capillary pumps. (A) Microfluidic immunoassays in parallel capillary pumps. Peltier modules are used to control evaporation from the outlets and minimize it at the inlets. Adapted with permission from ref.[84] Copyright 2004 Royal Society of Chemistry. (B) Passive pumping in a microchannel by capillary action and solvent evaporation using reservoirs of known geometry (top). Adapted with permission from ref.[85] Copyright 2009 Royal Society of Chemistry. Numerical modeling makes it possible to quantitatively take into account both capillary phenomena and solvent evaporation from the reservoirs (bottom). Adapted with permission from ref.[86] Copyright 2009 Royal Society of Chemistry.

are limited by external fluctuations affecting the evaporation conditions and the shape of the interfaces, as well as by the emptying of the inlet reservoirs at long times.

3.1.3 Control using temperature and/or forced convection

The mechanisms illustrated in Figure 5B show that solvent evaporation from a microfluidic channel is limited by the transport of the water vapor in the gas phase ($r_c \gg 10$ nm, eq 12). A possible way to increase the evaporation rate is therefore to either increase the saturation vapor pressure p_{sat} by increasing, for instance, the temperature; decrease the ambient relative humidity; or increase the mass transfer coefficient k in eq 13, for instance, by forcing convection in the gas phase.

Control of the local temperature of the menisci was demonstrated multiple times using integrated microfabricated heaters[81] (e.g., Figure 6), surface acoustic waves,[93] or photothermal effects induced by an IR laser.[94] For capillary-driven microfluidic systems, localized cooling of the inlet reservoirs close to the dew point was also conversely used to limit evaporation and the unavoidable change of concentration of the dissolved analytes, notably for miniaturized immunoassays involving submicroliter volumes as shown in Figure 7A.[84,89] Importantly, the fine control of heat transfer at the microfluidic scale, associated with the use of materials with high thermal conductivity (e.g., glass/silicon chips as in Figure 6), opens up the possibility to tune evaporation-driven pumping with short response times, down to ~ 1 s.[82]

Forced convection at the air/liquid interface was also reported multiple times using for instance air directly flowing in a microchannel at a distance of the meniscus fixed by the design of the microfluidic network,[81] an air fan for menisci trapped at the outlets of the chip,[83] or even localized nitrogen flows to control and maintain a steady flow rate once the mechanical balance is reached in a capillary pump.[90]

3.1.4 Increasing the evaporation surface for a higher pumping rate

Basic mechanisms and constraints – In the above-mentioned works, evaporation is limited by the transport of water in the gas phase, and evaporation-induced flow rates up to only a few tens of nL/min were reported, in agreement with eq 13. Beyond forced convection and temperature control, another possibility to achieve higher pumping rates consists of significantly increasing the evaporation surface A, limited before to the cross-sectional dimensions of a single microfluidic channel. This is illustrated schematically in Figure 8, showing the division of a main microchannel into a branched network where the many outlets improve evaporative pumping.

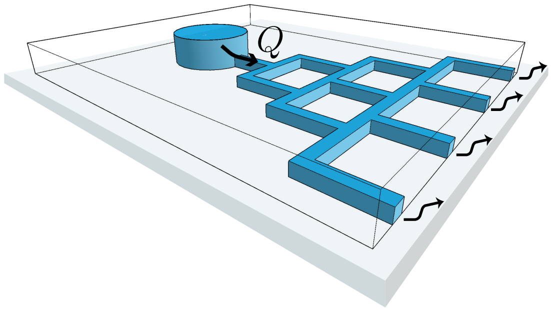

Figure 8: Splitting of one channel into N open channels to increase the evaporation area. Menisci are trapped by capillary forces at the open outlets.

This idea again shares a strong analogy with trees, which use the large surface of the leaves to increase the rate of water transported through the xylem. Note, however, that the flow rate Q does not necessarily vary linearly with the evaporation surface A. Indeed, cross-talking in the gas phase from each outlet or enhanced evaporation from the side channels may invalidate the linearity $Q \propto N$ with N being the number of outlets (Figure 8); see, for instance, ref[84] and Figure 7A. Even for a unique circular microfluidic outlet of radius h with a solvent flush with the surface (as in Figure 5B), Q does not vary as $\propto h^2$, as eq 13 might suggest, but rather as $\propto h$ due to the 3D nature of the diffusion of the vapor in the gas phase; see ref[78] for more insights into this law in the context of sessile drops. The mechanisms of vapor transport can also be affected by the size of the evaporation surface, as natural convection due to the density difference between the ambient air and the saturated water vapor phase can also play a role even for small surfaces (a few mm^2 in ref[95]). Thus, there are rules for an optimal design of the evaporation surface A in order to obtain the highest pumping rate, and the transport mechanisms of the vapor in the gas phase must be considered on a case-by-case basis.

Using the picture shown in Figure 8, and as discussed earlier by Goedecke et al.[83] in the context of microfluidic chromatography that requires large pressure drops, increasing the evaporation surface A unavoidably increases the flow rate Q and thus the pressure drop ΔP due to the viscous forces in the microfluidic system. Passive pumping at higher rates Q therefore requires larger capillary forces $\propto \gamma/r_c$ to prevent the chip from drying out, following the basic mechanisms shown schematically in Figure 5C for a single channel. This constraint imposes that the optimal evaporation surface is composed of hydrophilic *pores* with radii r_p that are sufficiently small to avoid the receding of the menisci and to offer the maximum rate of vapor transport in the gas phase.

Experimental strategies – Various strategies were developed over the past 20 years to design and integrate such evaporation surfaces in order to enhance the efficiency of evaporation-based microfluidic pumps. One can cite for instance microporous hydrophilic membranes,[96] filter papers,[97–103] hydrophilic porous materials[104] as shown in Figure 9, microfabricated arrays of micropores,[105,106] or even simply splitting the main channel into an array of open channels with small transverse dimensions[83,107] as illustrated in Figure 8. In these examples, the pore size r_p ranges typically from 1 to 10 μm, and the associated capillary pressure $P_c = 2\gamma/r_p \simeq$ 10–100 kPa ensures optimal pumping efficiency (i.e., without the receding of the menisci; see Figure 5C) for a wide range of applications.

These interfaces can be either directly integrated within the chip, in a separate device that acts as an autonomous pump connected to the chip using tubes,[96,97] or directly plugged at the outlet of the chip.[98,108] To keep the advantages offered by the microfluidic toolbox (miniaturization, portability, etc.) the chip dimensions nevertheless limit the maximum size of the evaporation area to a few of cm^2, and enhancement of evaporation pumping rates up to a few μL/min have been reported often.

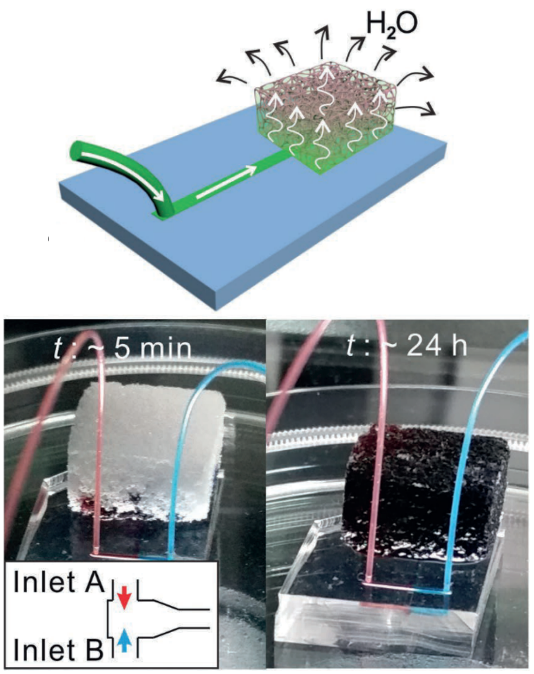

Figure 9: Increasing the evaporation surface for a higher pumping rate; in this case, a hydrophilic microporous PDMS sponge plugged at the outlet of a microfluidic chip. Adapted with permission from ref.[104] Copyright 2017 Wiley under CC BY 4.0 license.

Many developments of these pumps are motivated by microfluidic applications requiring nonpulsatile flows with rates up to a few μL/min, see for instance refs.[97,98] These pumps working without using any external power find also numerous applications in the biomedical domain such as continuous glucose monitoring,[96] sweat sensing and monitoring[102,106] or drug delivery,[108] which also require autonomous slow flows that are stable over a possible long usage time (days). Such pumps are also useful in the context of energy harvesting from water evaporation,[109] which obviously requires passive pumping.[107]

As for the case of a single channel, the porosity of the evaporation surface ($r_p \simeq$ 1–10 μm) ensures that evaporation remains limited by the vapor transport in the gas phase, eq 12. Fluctuations of the ambient conditions (temperature, relative humidity, air convection) thus limit the pump stability over a long time, which is a crucial issue, especially for biomedical applications. Again, active control of the temperature of the evaporation surface using integrated heaters, as well as the use of enclosed chambers with humidity sorption agents,[96] helps to control and enhance the evaporation performance.[99]

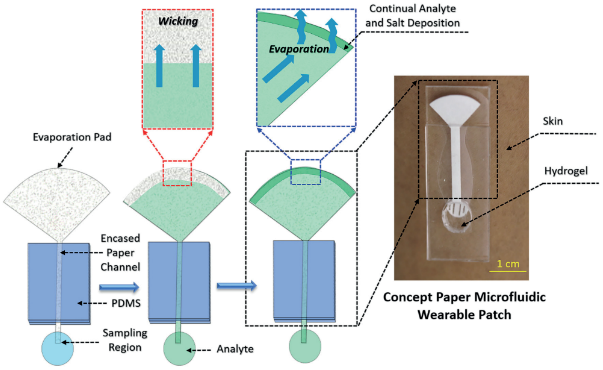

Figure 10: Evaporation pumping in paper-based microfluidics. In this example, a paper-based microfluidic device interfaced with skin for continuous sweat collection. Adapted with permission from ref.[102] Copyright 2020 American Institute of Physics.

3.1.5 Passive pumping in paper-based microfluidics

Among the examples cited earlier, evaporation plays a particularly important role for paper-based microfluidic devices, especially in the context of diagnostic or monitoring applications (except obviously when plastic sheets covering the paper-based chips are used to prevent evaporation[110,111]). For these microfluidic systems, the hydrophilic porous paper wicks aqueous solutions by capillary action, and specific chip geometries (often designed by simple cutting) allow for the specific management of the flows.[112,113] However, water evaporation from the paper matrix induces a flow in the chip that is superimposed on the transient flow induced by the capillary forces, as shown in Figure 10 for example. This flow in turn increases the pressure drop associated with viscous forces and can modify the imbibition dynamics. In the case of a simple strip of paper partially immersed in a water tank, for example, evaporation can stop the dynamics of liquid imbibition at a given position,[100,102,114,115] as detailed in section 4.4.5.

Hydrophilic microporous materials such as filter papers externally connected to a microfluidic chip also offer a simple way to passively pump fluids using evaporation,[96–98,103,104] see, for example, Figure 9 and 10. However, maximal efficiency and steady conditions are expected only when the external microporous interface is fully saturated with water. Thus, strategies to distribute the fluids rapidly and homogeneously over the surface were developed inspired again by the venation pattern in real leaves that ensures an optimal distribution of water from the stem to the surface of the leaf.[101]

3.1.6 Passive pumping limitation due to solute accumulation

Another aspect strongly limits the use of microfluidic pumps based on evaporation, especially for biomedical applications (monitoring, sensing, etc.): the unavoidable accumulation of nonvolatile solutes at the evaporation interface. These solutes can in turn decrease the water chemical activity at the interface $a_w^\star$, and, thus, the driving force for evaporation $\propto (a_w^\star - \mathrm{RH})$, as shown by eq 7 discussed in section 2.2.2. In the case of biological liquids (sweat, for example[116]), thus containing ionic species in solution, the accumulation of the latter on the evaporation interface inevitably leads to a decrease in the driving force of evaporation when $a_w^\star$ decreases down to values close to the ambient humidity (RH). As shown in Table 1, this mechanism can eventually lead to the formation of crystals under most conditions, thus stopping the passive pumping mechanism. For example, the water activity of a saturated sodium chloride solution is $a_w \simeq 0.75$,[67] and evaporation in conditions RH $< 75\%$ thus unavoidably leads to crystallization. Such effects were demonstrated early on in many passive pumping systems: single capillary pumps,[88] external autonomous micropumps,[96] and paper-based microfluidic devices[102] as shown in Figure 10. This effect undoubtedly limits the scope of application of the passive pumping devices listed earlier to very dilute solutions for which $a_w \simeq 1 - V_m C$ with $C \ll 1/V_m$ being the concentration of the considered species (mol/m^3), and only at short times because the solutes accumulate continuously. We will return to this point in detail in section 4.5.1, showing in particular how simple mass transport arguments allow one to estimate the typical rate of solute accumulation on the evaporation interface and, thus, for what conditions and up to what times evaporation-induced pumping remains nearly steady.

Some groups have also shown how to overcome this issue by placing a large reservoir of water upstream of the evaporation interface, thus diluting the solution pumped by the system,[96] but at the cost of a certain complication of use. On the other hand, we will see in section 4.5 that this passive concentration mechanism can be cleverly exploited not only to preconcentrate solutes but also to obtain useful physicochemical information or to manufacture micromaterials. In the case of crystallization, for example, section 4.5.2 will show that evaporation-induced microfluidic pumping can be harnessed to study the mechanisms of nucleation and growth of crystals in confined geometries (even possibly at the gas/liquid interface), which is an important issue for many applied problems (scaling in water treatment, crystallization in porous media, etc.)[117]

3.1.7 Evaporation from nanoscale pores

The transpiration of water by trees, which can lead to large tensile stresses and negative liquid pressures within the xylem, is a source of inspiration for the realization of microfluidic pumps that can withstand very high pressure drops ΔP, as required by certain applications such as chromatography.[83] On the other hand, these high pressures imply high capillary pressures $P_c \propto \gamma / r_c$ to trap the menisci and, therefore, very small pores, possibly down to a few nanometers.

The basic picture illustrated in Figure 5B actually remains valid even for channels with nanometric transverse dimensions, as demonstrated by Vincent et al. using experiments of evaporation-driven flows at extreme negative tensile stresses (down to approximately -100 MPa) in nanofabricated porous materials with pores of a few nanometers.[118] In this case, however, evaporation turns from a regime limited by the transport in the gas phase to a *flow-limited* regime for which the flow itself is the limiting step, as shown in Figure 11. Indeed, the viscous forces due to the high hydrodynamic resistance R_h of the nanochannels can impose a curvature r_c of the menisci down to a few nm, thus affecting the partial vapor pressure at the interface, as shown by the Kelvin-Laplace equation (eq 12) and Table 1. In this case, the ambient relative humidity RH directly sets the curvature r_c of the nanomenisci and the water potential at the interface is $\Psi^\star \simeq \Psi_{\text{ext}}$ as shown in Figure 11. The overall evaporation-induced flow rate is limited in this regime by the viscous forces in the channel and thus is given by:[118]

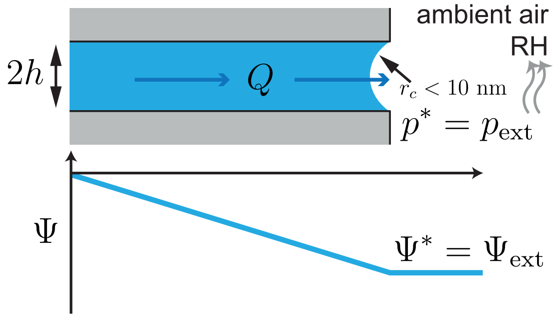

Figure 11: Evaporation-driven pumping at nanoscale ($h \sim$ nm) in the flow-limited regime. The ambient conditions set the water potential $\Psi^\star$ at the interface and, thus, the local partial vapor pressure $p^\star$.[118]

$$Q \simeq -\frac{\Psi_{\text{ext}}}{R_h} = -\frac{RT}{R_h V_m} \ln(\text{RH}) \,, \qquad (14)$$

independently of the transport of the vapor in the gas phase. The transition between the vapor transport-limited and flow-limited regimes has been also discussed in ref[119] in the context of water transpiration in trees using parameter maps demarcating these regimes in a specific configuration (array of pores including also the hydrostatic contribution due to gravity). To our knowledge, no microfluidic experiments have been reported to explore the continuous transition between these two regimes, and there is no experimental evidence of a vapor transport-limited regime that could possibly exist for nanosized pores for very small pressure drops (e.g., at very high relative humidity).

Vincent et al.[118] demonstrated that the receding of the meniscus as shown schematically in Figure 5C can also occur in the flow-limited regime for channels with nanoscale dimensions, but the critical capillary pressure in that case only depends on the external water potential, and receding can thus occur at low relative humidity. As shown in Table 1, the critical capillary pressure $P_c = 2\gamma/h$ for pure water ranges from $P_c \simeq 10$ MPa for nanochannels of height $h \simeq 10$ nm down to $\simeq 100$ kPa for $h \simeq 1$ μm, allowing one to set the accessible pressure range according to the envisaged microfluidic application.

3.1.8 Evaporation from hydrogels: toward synthetic microfluidic trees

Different groups have used micro- and nanofabrication tools to achieve controlled architectures to mimic tree water transpiration, sometimes withstanding high negative pressures. The realization of a synthetic tree and the first experimental proof of passive pumping at a negative pressure in a microfluidic channel were provided by Wheeler and Stroock.[120]

In this pioneering work, these authors fabricated a single microfluidic channel as shown in Figure 12A into a hydrogel-based chip to minimally mimic a tree consisting of a trunk connecting the leaves to the root system. As with the mesophyll cells on the surface of real leaves, hydrogels are water permeable materials and have a nanoporosity that allow them to remain hydrated under low ambient humidity conditions. These materials are then good candidates to mimic the pumping mechanisms shown in Figure 11 with nanoscale pores and thus possibly high induced pressure drops. Wheeler and Stroock used soft lithography techniques to fabricate a synthetic tree made of poly(hydroxyethyl methacrylate) hydrogels, and they report passive pumping at negative pressure of approximately -1 MPa, estimated from measurements of the evaporation-induced flow rate Q and the channel hydrodynamic resistance R_h.

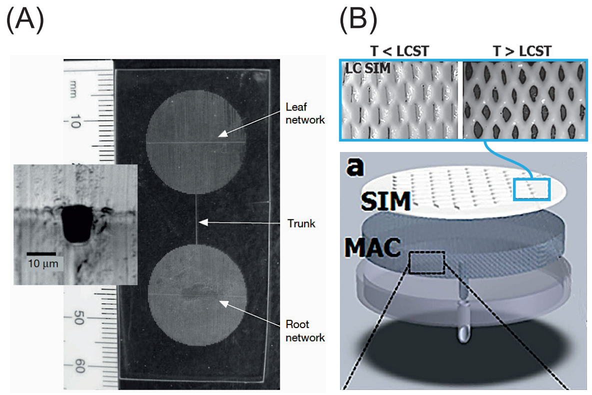

Figure 12: Toward synthetic trees and leaves. (A) Microfluidic tree in a hydrogel chip leading to transpiration at negative pressures. Adapted with permission from ref.[120] Copyright 2008 Springer Nature. (B) Leaf-inspired micropump composed of a macroporous cryogel superimposed by a thermosensitive membrane, with micropores in the form of stomata whose opening depends on the temperature (above pictures). Adapted from ref.[108] Copyright 2016 Springer Nature under CC BY 4.0 license.

Such negative pressures raise the question of possible cavitation instability because water is then metastable with respect to its vapor phase (boiling) but also with respect to any dissolved gas; see refs[121,122] for related studies on cavitation in hydrogels and ref[123] on the role of colloidal particles on the cavitation of water droplets. These issues are again very important for water transpiration in plants, as cavitation can occur in the xylem, e.g., during extreme drought, resulting in air-filled ducts and thus a loss of conductance for water transport.[66,75,76]

Following Wheeler and Stroock, many groups have reported hydrogel-based evaporation pumping in microfluidic devices again for applications that require nonpulsatile passive pumping.[108,124–127] In these cases, however, one should go beyond the simple mechanical picture shown schematically in Figure 11 and take into account a proper description of the water mass transport in the hydrogel[128] to quantitatively predict the limiting resistances to evaporation-driven pumping.

Inspired by the mechanisms of controlled stomata transpiration in true leaves, various works have also reported controlled evaporation from hydrogels[105,108,126] or microporous materials[125,129] using microfabricated arrays of slit-like micropores ($\sim 100\ \mu$m) mimicking stomatal apertures on real leaves as shown in Figure 12B. Such architectures can be made using perforated polymeric films covering a microporous membrane clamped at the outlet of a microfluidic chip,[105] using microstructured polymeric coatings[108] or microfabricated apertures etched through a silicon wafer.[129] In particular, these microapertures limit the evaporation surface and thus make it possible to adjust the pumping rate.[125] Active control also has been demonstrated by Kim et al. using a microstructured thermosensitive porous polymeric layer,[108] see Figure 12B. Synthetic stomatal apertures coupled to microfabricated cavities playing the role of stomatal chambers covering a nanoporous artificial leaf were also reported by Shi et al.[129] This hierarchical architecture was used to study the role of the synthetic stomatal chambers on the interplay between humidity variations in the ambient air and evaporation from the nanoporous leaf.[129]

3.2 Pervaporation-driven pumping

As explained in section 2, pervaporation is a separation process that uses a dense membrane to selectively transport molecules from a liquid phase to a vapor phase. Pervaporation is commonly used by the chemical industry for a wide range of operating units, such as dehydration of organic solvents, removal of traces of volatile organic compounds from water, or separation of organic mixtures.[28] Very little work reports the use of pervaporation as a separation process as such to separate the components of a solution in a microfluidic chip; see section 4.2 for a few examples. Beyond chemical separations, pervaporation shares strong analogies with evaporation from a fixed gas-liquid interface (section 2); therefore, flows driven by pervaporation are expected in any microfluidic system that integrates a dense membrane.

3.2.1 First experimental evidences

The first experimental evidences of flows induced by pervaporation in a microfluidic chip were reported in 2004 and 2005 by three different groups.[130–132] Eijkel et al. fabricated an array of parallel microfluidic channels with small transverse dimensions (thickness $\simeq 500$ nm, width 2–30 μm) embedded in a polymide film that was a few microns thick (Figure 13A). Water pervaporation occurs through the polymide *roof* of the channels, thus playing the role of a thin membrane, over an area defined by microfabrication, $\simeq 350 \times 300\ \mu\text{m}^2$. This pervaporation flux is compensated by a water flow rate from two reservoirs connected to the array of microfluidic channels. For quantitative measurements, Eijkel et al. used conductimetry and a KNO_3 aqueous solution to relate the pervaporation-induced flow to the increase of the ionic species in the channels. Velocities of a few μm/s from both reservoirs were estimated, in a quantitative agreement with the 1D picture shown in Figure 13B, assuming that pervaporation is limited by the transport through the thin polyimide membrane and knowing the permeability of water through this material.[130]

In 2004-2005, Verneuil et al.[131] and Randall and Doyle[132] reported similar phenomena for a single linear channel filled with water in a PDMS chip, although surprisingly without any membrane, as shown in Figure 13C. As explained in section 2, silicone-based materials such as PDMS are used for pervaporation separation processes at the macroscale, and these two works clearly identified that flows occur in the microfluidic channel because of pervaporation of water through the whole PDMS chip itself. These observations were supported by measurements using particle tracking velocime-

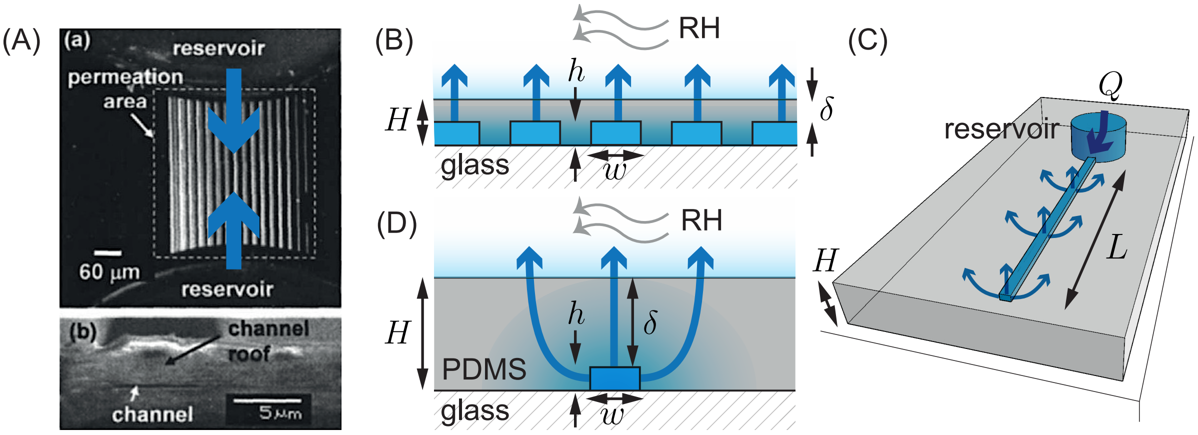

Figure 13: Pervaporation-driven microfluidic pumping. (A) Water pervaporation in an array of submicrometer channels in a polymide chip, top and sectional views. The blue arrows indicate the net water flux to compensate from pervaporation. Adapted with permission from ref.[130] Copyright 2005 American Institute of Physics. (B) Cross-sectional view of an array of parallel channels in a film of thickness H sealed by a glass slide. The color gradient indicates the steady solvent concentration inside the film. (C) Water pervaporation in a single dead-end channel in a thick PDMS chip. Q is the flow rate compensating the water loss by pervaporation along the channel. (D) Cross-sectional view of a microchannel in a thick PDMS slab, with the same indications as for (B).

try of dispersed fluorescent tracers showing flow rates $Q \simeq 0.5$ nL/min within dead-end channels of $\simeq 1$ cm long, almost independently of their transverse dimensions. These observations and the magnitude of the flows were explained by both groups using the solution-diffusion model[40,41] as will be explained later.

3.2.2 Models for pervaporation-driven flows in PDMS channels

Pervaporation-driven flows in PDMS chips were rationalized both by both Verneuil et al.[131] and Randall and Doyle[132] assuming the geometry shown in Figure 13C and D: a single linear channel of length L with transverse dimensions that are much smaller than the thickness H of the PDMS block. Water pervaporation from the filled channel occurs through a 3-step mechanism as explained in section 2: (i) dissolution of water molecules within the matrix at a concentration c^p_{sat} (kg/m^3), (ii) diffusion of the water molecules through the PDMS layer, and (iii) water evaporation in the surrounding air of relative humidity RH.

For a sufficiently long dead-end channel, water pervaporation along the channel's length L is expected to drive a flow at a rate:

$$Q = Lq\,, \qquad (15)$$

where q (m^2/s) corresponds to the pervaporation flux (per unit length) described by the 2D diffusion configuration shown in Figure 13D. In the model derived by Verneuil et al. and Randall an Doyle, the resistance to mass transfer in the gas phase is considered negligible (an assumption probably valid for a PDMS block of centimeter thickness; see further discussion on this point later), the diffusion of water molecules within PDMS is assumed to follow Fick's law with a constant diffusion coefficient D^p_w (m^2/s), and the water concentration in PDMS is assumed to follow Henry's law. The water concentration at the external boundary is thus $c^p_{\mathrm{edge}} \simeq \mathrm{RH}\, c^p_{\mathrm{sat}}$, with c^p_{sat} (kg/m^3) being the concentration of water at saturation in the PDMS matrix and RH being the relative humidity of the ambient air.

On the length scale H of the mass transfer, the transverse channel dimensions are small, and diffusion occurs almost radially. In this 2D configuration, Randall and Doyle and Verneuil et al. recognized that the external boundary plays only a logarithmic role, and provided the following approximate estimate of the pervaporation mass flux (per unit channel length), $\rho_w q$ [kg/(m s)]:

$$\rho_w q \simeq \frac{\pi}{\mathcal{L}} D_w^p c_{\text{sat}}^p (1 - \text{RH}) \,, \tag{16}$$

where $\mathcal{L}$ is a logarithmic factor that takes into account the actual geometry, e.g., $\mathcal{L} = \ln[w/(4R)]$ for a thin channel ($h \ll w$) in a semicircular PDMS block of radius R.[132] Equation 16 was demonstrated to account quantitatively for the measurements done using particle tracking velocimetry,[131,132] with $c_{\text{sat}} \simeq 0.72$ kg/m^3 ($\simeq 40$ mol/m^3) and diffusivity of water in PDMS of the order of $D_w^p \simeq 10^{-9}$ m^2/s, see section 3.2.4 below. The same expression also explains the weak dependence of the pervaporation-driven flow rate Q to the transverse dimensions of the channel (height h ranging between 2 and 125 μm and width w ranging from $\simeq 25$ μm to $\simeq 500$ μm were studied in ref[131]).

More recently, Dollet et al.[133] used conformal mapping techniques to provide an exact analytical solution of the diffusion equation governing the water concentration in PDMS for the case of a rectangular channel filled with water and embedded in an infinite PDMS layer of thickness H, as in Figure 13D. From this analytical solution, the same authors also provided the following approximate solution for the pervaporation rate (per unit channel length):

$$\rho_w q \simeq \left[\frac{w}{\delta} + \frac{2}{\pi}\left(\ln\frac{(H+\delta)h}{\delta^2} + \frac{H}{\delta}\ln\frac{H+\delta}{h}\right)\right] \times D_w^p c_{\text{sat}}^p (1 - \text{RH}) \,, \tag{17}$$

which correctly accounts for the limiting regime described by eq 16 for $w \ll \delta$, but with an accurate expression of the logarithmic correction $\mathcal{L}$. This expression also shows that, when $w \gg \delta$, pervaporation turns to a simple 1D mass transfer with:

$$\rho_w q \simeq \frac{w}{\delta} D_w^p c_{\text{sat}}^p \; (1 - \text{RH}) \,, \tag{18}$$

similarly to eq 8 for the 1D model described in section 2. It is this last relation that was used by Eijkel et al. to estimate pervaporation-induced flows through the thin polyimide membrane[130] shown in Figure 13A. The comparison between eq 17 and the 2D case given by eq 16 shows that q can be geometrically enhanced only when considering a thin membrane over a wide channel ($w \gg \delta$), an experimental configuration, however, that is prone to mechanical issues for PDMS due to its possible elastic deformation.

In these models, the resistance to mass transfer in the vapor phase is also likely to play a role, as previously discussed in section 2.2.4 (Figure 4). To illustrate this point we consider for simplicity the 1D configuration shown in Figure 13B. The resistance to mass transfer through the PDMS membrane $R_p \sim \delta/(D_w^p c_{\text{sat}}^p)$ has to be compared to the resistance to mass transfer in air $R_a \sim \lambda/(D_w^{\text{air}} c_{\text{sat}})$ assuming 1D diffusive transport over a boundary layer of thickness λ ($D_w^{\text{air}} \simeq 2.5 \times 10^{-5}$ m^2/s the diffusion coefficient and $c_{\text{sat}} \simeq 19 \times 10^{-3}$ kg/m^3 is the concentration of water vapor in air at saturation at $T = 22$°C[69,70]). For a membrane thickness of $\delta = 20$ μm, mass transfer is limited by the PDMS ($R_p > 10 R_a$) only for a boundary layer $\lambda < 1$ mm, showing that blowing air over the membrane (as, for instance, in refs[133–135]) can be relevant in some cases. This criterion, estimated assuming 1D transport, cannot *a priori* be applied to any configuration for which 2D or 3D effects can be expected, but it allows one to conclude that gas-phase transport must be considered precisely as soon as the PDMS membrane is thin.

3.2.3 Transition between 1D and 2D regimes: toward complex networks

The transition between 1D (eq 18) and 2D (eq 16) regimes was illustrated by Noblin et al.[134] who considered pervaporation-driven flows in a *biomimetic leaf* constituted by an array of parallel dead-end channels embedded in a PDMS layer, as shown in Figure 14. For a high channel density ($d \ll \delta$, d being the center-

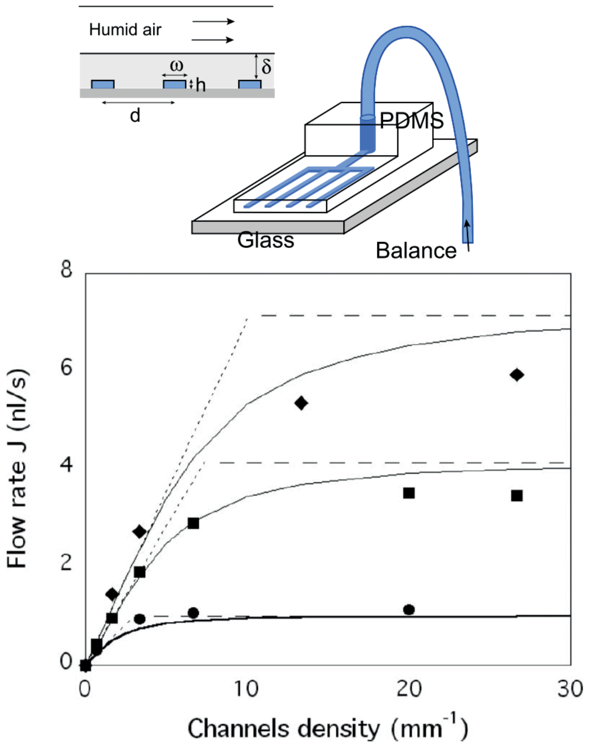

Figure 14: Transition between 1D and 2D regimes in an array of parallel dead-end channels (biomimetic PDMS leaf, top). The graph shows that the overall pervaporation-driven flow rate saturates for high channel density $\propto 1/d$, and that the transition between 1D and 2D regimes occurs for $d \sim \delta$. Symbols correspond to different δ (diamonds, 45 μm; squares, 78 μm; disks, 320 μm), and continuous lines correspond to simulations using the solution-diffusion model. Adapted from ref.[134] Copyright 2008 National Academy of Sciences, U.S.A.

to-center distance between channels), the overall pervaporation-induced mass flux (per unit length) is mainly 1D, and given by:

$$\rho_w q \simeq \frac{W}{\delta} D_w^p c_{\mathrm{sat}}^p \left(1 - \mathrm{RH}\right), \tag{19}$$

with W the width of the array independently of the channel density. For small channel density ($d \gg \delta$), the overall pervaporation-induced flow rate increases linearly with the channel density as there are no couplings between each channels, and pervaporation rates from each channel are given by eq 16. Note also that Noblin et al. showed in the same work that the pervaporation-induced flow rates vary as $Q \propto (1 - \mathrm{RH})$, in agreement with the theoretical predictions given earlier, suggesting that the slight deviations from Henry's law at small and high vapor activities evaluated by vapor sorption measurements at equilibrium,[136] remain negligible and that the assumption of a constant diffusion coefficient D_w^p is also sufficient; see refs[137–139] for this issue.

The study by Noblin et al. shows how physical arguments explain the vascular architecture of the leaves for an optimal vein density for water transpiration. This result was validated by measurements on real leaves indeed showing a linear relationship between the mean distance between leaf veins and leaf thickness ($d \propto \delta$).[134] In a similar context, the precise control of pervaporation-induced flows mainly due to the diffusive transport of water through the PDMS opens exciting perspectives to study the mechanisms of gas embolism development in the venous network of leaves, as shown in Figure 15,[140] see also ref.[141] Beyond these results that are relevant for plant biology, the same considerations can also be used to properly design channel geometries to minimize the couplings by pervaporation between neighboring channels.[142]

3.2.4 Toward quantitative pervaporation-induced flows?

Equation 17 shows that it is possible to predict quantitatively the flow rate Q induced by pervaporation in a single linear channel, and to control it through the geometry of the chip. This prediction is valid for a long channel because it ignores edge effects due to geometric amplification of the pervaporation flux at the tip and entrance of the channel.[142]

Such a quantitative description is also only possible if values of c_{sat}^p and D_w^p are precisely known. Water saturation in PDMS Sylgard 184 traditionally used for making microfluidic chips was reported by Randall and Doyle using gravimetric measurements at $T = 21$°C: $c_{\mathrm{sat}}^p \simeq 0.72$ kg/m^3 ($\simeq 40$ mol/m^3).[132] The same value was found by Harley et al.[136] also for Sylgard 184 using water vapor sorption mea-

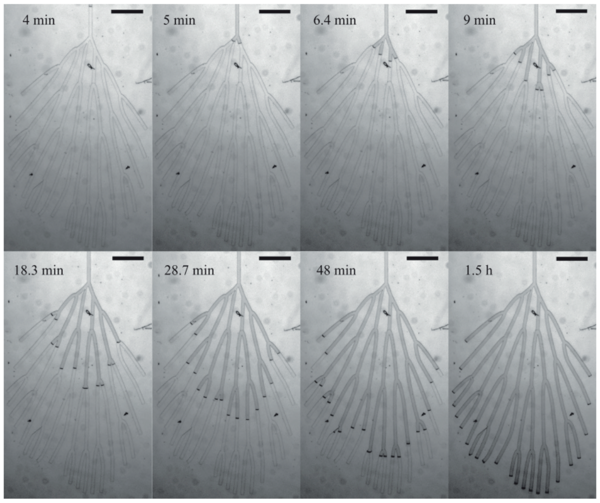

Figure 15: Pervaporation in complex PDMS channel networks. Snapshots of the drying out of a network mimicking an Adiantum leaf in a thin PDMS layer. The dead-end channels are initially filled with water through a single inlet on top of the images (not visible). The darker areas correspond to the dried out parts of the channels, and the lighter ones are filled with water. In this experiment, the evaporation of water from the meniscus and the pervaporation in the air-filled parts of the channels are not negligible compared to pervaporation from the liquid-filled parts. Scale bar 1 mm. Adapted with permission from ref.[140] Copyright 2020 Cambridge University Press.

surements at $T = 30°\text{C}$ ($\simeq 0.95$ cm^3 (STP) per g of PDMS, leading to $c^p_{\text{sat}} \simeq 0.73$ kg/m^3 assuming a density of $\simeq 965$ kg/m^3). Using these values, the groups cited earlier have shown a quantitative agreement between the measured pervaporation-induced flow rates and the corresponding theoretical predictions for linear channels by adjusting the diffusion coefficient D^p_w of water in PDMS. Values in the range $D^p_w \simeq 0.8\text{–}1.1 \times 10^{-9}$ m^2/s were reported, in a good agreement with dynamic vapor sorption measurements in cross-linked Sylgard 184,[136] but also with many other estimations of this transport coefficient using permeability measurements through PDMS membranes (possibly in the microfluidic context) or silicone-based rubbers, they were sometimes extrapolated from measurements of gas permeability.[137–139,143–146]

A closer comparison, however, shows that the values of the coefficient D^p_w can vary from work to work up to ±20%. Beyond the measurement uncertainties, several factors can explain this deviation to a more accurate prediction of the pervaporation-induced flows, notably the dependence of the parameters on temperature, the precise composition of the PDMS formulation (see, for instance, the variations of the permeability[145,147] and the water absorption[148] due to the mixing ratio of PDMS and its curing agent), or the role played by surface modifications such as plasma treatment leading to a silica-like surface that acts as a barrier as shown for oxygen permeation.[149]

In turn, microfluidic tools could be used to finely measure the diffusion coefficient D^p_w in PDMS and identify the parameters governing its variations (water activity, temperature, pretreatment, etc.). These measurements would perhaps provide a better understanding of the molecular mechanisms of water transport in silicone elastomers,[137–139,144,146] an issue that remains important, especially in the context of moisture permeation.[136] It would also be relevant to explore the possibility of controlling D^p_w using another solvent (possibly in the gas phase) that is capable of swelling PDMS and thus significantly increasing the diffusivity of water D^p_w, as shown in the context of permeation of organic solvent mixtures through elastomers.[150]

3.2.5 Dynamic control and pervaporation-driven pumping

Verneuil et al.[131] and Randall and Doyle[132] recognized early that the unavoidable pervaporation-driven flows in PDMS can be detrimental for applications that require highly controlled conditions (e.g., no flows or constant concentration in aqueous solutions with solutes that are not permeable in PDMS). Both groups also showed that a simple way to mitigate these flows consists of supersaturating the PDMS matrix with water by presoaking the chip in a water bath or by directly immersing it. When the chip is fully immersed in a water bath, the pervaporation-driven flows decrease within a few hours for a centimeter-sized PDMS block,[131] thus suggesting that the time scale $\sim H^2/D_w^p$ of the 2D picture shown in Figure 13D limits the temporal evolution of the flows to any change in the external conditions.

For accurate temporal control of the pervaporation-induced flows, Leng et al. used multilayer soft lithography to integrate a thin PDMS membrane (thickness in the range $\delta \simeq$ 10–30 μm) separating two microfluidic channels: one filled with pure water, and the other filled with a dry sweep gas to remove actively the water vapor.[135] With such devices as shown in Figure 16A, pervaporation-induced flows can be controlled with response times down to a few seconds by controlling the flow of the sweep gas as seen in Figure 16B. This time scale is in line with the theoretical pictures given earlier because the characteristic diffusion time across the membrane is only $\simeq \delta^2/D_w^p \leq 1$ s for $\delta \simeq 20$ μm.

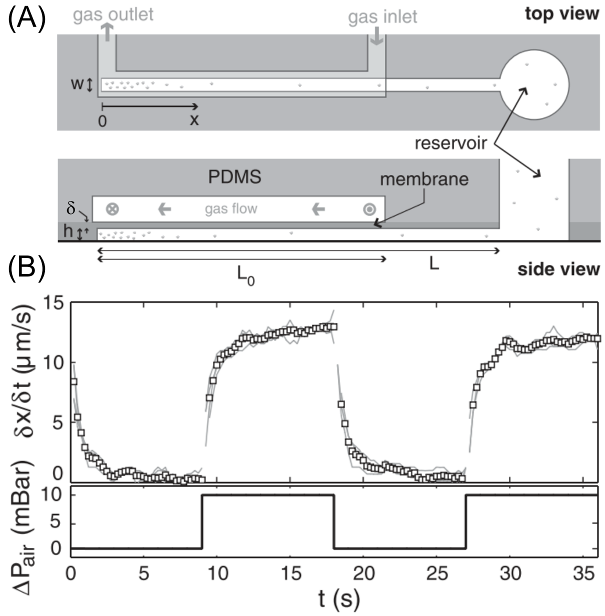

Figure 16: Dynamic control of microfluidic pervaporation. (A) Multilayer PDMS chip incorporating a thin PDMS membrane separating the water-filled dead-end channel from a channel with a gas sweep for vapor removal. (B) Pervaporation-induced flows, measured using particle tracking velocimetry, in response to the switching on and off of the sweep gas. Adapted with permission from ref.[135] Copyright 2006 American Physical Society.

Quite surprisingly, no group has exploited pervaporation through microstructured PDMS sheets for passive pumping, as in the many applications using evaporation listed in section 3.1. However, we note the study in ref[151] that exploits the pervaporation of organic solvents through a dead-end plastic tube connected to a miniaturized liquid fuel cell to induce passive pumping. On the other hand, the recent theoretical developments discussed earlier show that a precise control of the pumping flow rates can be obtained for water, simply by playing on the geometries of the channels in PDMS chips, a major asset in particular for low flow rates compared to evaporation. As in the case of evaporation, one of the major obstacles to the use of pervaporation in applications also concerns the associated accumulation of insoluble solutes, eventually leading to a decrease in the driving force of pervaporation and ultimately to irreversible clogging of the channels. However, Verneuil et al.[131] and Randall Doyle[132] pointed out that the flows induced by pervaporation constitute an original way of concentrating solutes in a controlled manner, and open the possibility of multiple studies such as the exploration of phase diagrams or the fabrication of micromaterials; see further details in sections 4.3 and 4.4.

3.3 Osmosis-driven pumping

3.3.1 Generalities

Driving force – Forward osmosis allows a passive mass transfer as soon as a difference of osmotic pressure $\Delta\Pi$ exists across a fixed and semipermeable membrane (section 2); as for evaporation and pervaporation, osmosis can thus be exploited to passively pump solutions in microfluidic applications. Figure 17A illustrates this simple picture: a semipermeable membrane integrated within a microfluidic chip separates two channels thus generating an osmotic pressure difference $\Delta\Pi$ between a *draw* solution, typically a concentrated solution of osmotic agents, and a more dilute solution, referred to as the *feed* solution. The osmotic pressure difference induces a net solvent flow rate Q

as long as the solutes are rejected by the membrane. For an ideal semipermeable membrane (i.e., for a full solute rejection), and neglecting the transmembrane pressure difference ΔP (see below), the volumetric solvent flux Q (m^3/s) through the membrane is given by:

$$Q = A\mathcal{L}_p(\Delta P - \Delta\Pi) \simeq -A\mathcal{L}_p\Delta\Pi\,, \tag{20}$$

with A being the membrane surface and $\mathcal{L}_p$ being its permeability in m/(s Pa), similarly to eq 9 discussed in section 2.2.2 for the same 1D configuration (Figure 3C).

Dense membranes – Microfluidic osmosis-driven flows can be observed with dense membranes, commonly used for pervaporation processes, such as PDMS,[131,132] polyimide,[130] or any other polymeric material. The permeability $\mathcal{L}_p$ can be estimated in that case by the solution-diffusion model using the 1D picture described by eq 8 and eq 11 in section 2.2.2:

$$\mathcal{L}_p \simeq \frac{D_w^p c_{\mathrm{sat}}^p}{\rho_w \delta}\frac{V_m}{RT}\,, \tag{21}$$

with δ being the membrane thickness. For such dense membranes, the difference of osmotic pressure can be obtained with any solute (e.g., salts, polymers, etc.) that does not dissolve in the membrane. Passive pumping has been demonstrated, for instance, by Eijkel et al. in a microfluidic chip integrating a thin polyimide membrane ($\delta \simeq 2.3$ μm, Figure 13A) using pure water and a sodium chloride solution.[130] Nevertheless, forward osmosis through dense PDMS membranes is not the most efficient method for pumping applications in the case of aqueous solutions, because their permeability can be small, for instance, $\mathcal{L}_p \simeq 10^{-16}$ m/(s Pa) for pure water using the estimate given by eq 21 for a membrane of thickness $\delta = 40$ μm. This statement is no longer valid for high performance membranes having a thin, dense, hydrophilic layer supported by a porous substrate that allow both high water permeability and selectivity in the current applications of forward osmosis.[152] On the other hand, we will return to this later in section 4.3 to show that the small permeability of PDMS membranes to water does not prevent the use of osmosis in PDMS chips for applications such as the screening of phase diagrams or protein crystallization conditions.

Liquid membranes – Osmosis-driven flows can also occur through liquid interfaces, such as thin liquid oil films separating two aqueous compartments in a microfluidic channel. In this case, water molecules dissolve and diffuse in the oil phase, as for pervaporation or osmosis through a dense membrane, leading possibly to a net water flow rate relative to the liquid interface. Such mechanisms play an important role in the context of enhanced oil recovery using low-salinity water flooding, as demonstrated for instance by Bremond and co-workers using microfluidic experiments at the pore scale level,[153] see also refs[154,155] for other related works using porous micromodels. Even if the mechanisms are clearly based on osmotic effects, we will not make an extended review of such works because they do not strictly correspond to the scope of the present review focused on passive mass transport through a fixed interface.

Porous membranes – Larger osmosis-driven flows can be obtained *a priori* with porous semipermeable membranes due to their higher permeability $\mathcal{L}_p$. There is, however, a compromise, because the gain in efficiency associated with a more permeable membrane, while allowing full rejection of the osmotic agents, can be offset by a drop in the driving force $\Delta\Pi$. Indeed, as the osmotic pressure depends on the molar concentration of the solute, the highest driving forces are reached only for highly soluble solutes with small molecular weights. On the other hand, the pore size has to decrease with the size of the rejected solute, thus imposing *a priori* a small permeability $\mathcal{L}_p$ for rejecting small osmotic agents, the so-called selectivity-permeability trade-off.[156] One way to overcome this trade-off is to use asymmetric membranes with a thin selective layer mechanically supported by an underlying porous layer. Another possibility would be to use solutes not fully rejected by the membrane but which could induce transiently a higher osmotic force

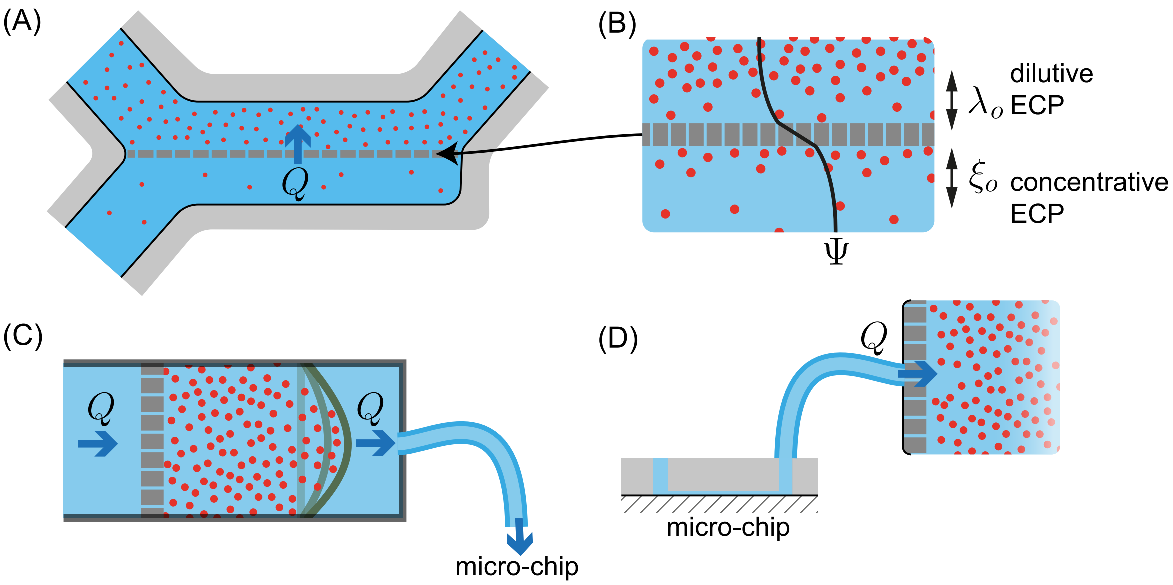

Figure 17: Microfluidic osmotic pumping. (A) Sketch of microfluidic forward osmosis. The osmotic pressure difference $\Delta\Pi$ between the draw solution (top) and the feed solution (bottom) induces a flow through the membrane at a rate Q given by eq 20. (B) Zoom-in on the membrane evidencing external concentration polarization (ECP), on either the feed or draw sides (concentrative vs dilutive ECP). (C) Osmosis-driven actuation of a movable partition, and (D) osmotic suction for microfluidic pumping.

or even flows driven by diffusio-osmosis, as recently demonstrated through fully permeable nanopores.[26] These configurations would merit further investigation in the more specific context of microfluidic osmosis-driven pumping reviewed here.

Most of the passive osmotic microfluidic pumps referenced below use dialysis membranes with homogeneous porosity across their thickness. The corresponding molecular weight cut-off (MWCO) range up to several kDa with a hydraulic permeability $\mathcal{L}_p \simeq 0.5\text{–}5 \times 10^{-12}$ m/(s Pa) for pure water at room temperature. However, some studies report the use of asymmetric membranes commonly used in reverse osmosis and nanofiltration for which higher permeability can be expected.[156] In the applications listed below, osmotic agents are typically small ions (sodium chloride [Na^+, Cl^-]), small molecules (e.g., sucrose), or short-chain polymers such as dextran or polyethylene glycol, and the driving force ranges from $\Delta\Pi \simeq 0.1$ to $\simeq 50$ MPa, which is therefore much higher than the pressure differences induced by the viscous forces or due to the hydrostatic contributions, $\Delta P \ll \Delta\Pi$ (forward osmosis, see also Table 1).

Concentration polarization – In the microfluidic applications reviewed below, mass transfer limitations are also likely to play a role due to the development of concentration gradients at the membrane surface, the so-called concentration polarization (CP)[25] mentioned in section 2.2.4. More precisely, the osmosis-driven flow through the membrane *a priori* induces a depleted layer of draw molecules close to the membrane surface, thus decreasing the osmotic driving force (dilutive ECP, Figure 17B). Similarly, the same flow can concentrate any osmotic active solutes present in the feed solution (as soon as the latter are rejected by the membrane), thus decreasing the driving force (concentrative ECP, Figure 17B).

The extents λ_o and ξ_o of these layers are given by a balance between molecular diffusion and advection by the osmotic flow but also by any other flow close to the membrane surface,[25] so that it is not possible to give generic values for λ_o and ξ_o because they depend strongly on the experimental configuration. In the frontal configuration shown in Figure 4, for instance, the flow J due to forward osmosis continuously accumulates the solutes upstream of the membrane in a boundary layer of extent $\xi_o \propto D/J$ (with D being the diffusion coefficient of the solute), therefore possibly decreasing the osmotic driving force (concentrative ECP), see section 2.2.4. In any case, microfluidic tools allow a direct visualization of the ECP phenomenon in particularly well controlled flow conditions as demonstrated by Jiao et al. using a dye and fluorescence microscopy in a microfluidic chip integrating a nanofiltration membrane.[157] Such studies make it possible to directly validate the ingredients of the convection-diffusion models in particular used to optimize large-scale forward osmosis processes.

For asymmetric membranes having a thin active layer mechanically supported by a thicker porous layer, CP can also occur within the pores of the support layer (internal CP, ICP) making it little dependent on flows near the membrane surface.[158] Fouling of the membrane surface by adsorption of large molecules can also occur, which also reduces its overall permeability,[159,160] but in most cases the relatively low permeate flows ($J < 10$ μm/s) make it possible to work under subcritical conditions thus limiting fouling.[161] We will come back to these questions when they are raised in the work reviewed below.

Geometrical pumping configurations – As for the case of evaporation, many groups developed autonomous osmosis-driven pumps for microfluidic applications that require nonpulsatile low flow rates or for applications that cannot integrate external macroscale pumps or that require power free pumps, such as portable applications, *in vivo* drug delivery, continuous monitoring, energy harvesting, etc. Among the published works on microfluidic osmotic pumps, two main configurations emerge as shown in Figure 17C and D, and we focus in the following section on the osmotic actuation of a movable partition by means of osmosis shown in Figure 17C.

3.3.2 Osmotic actuation

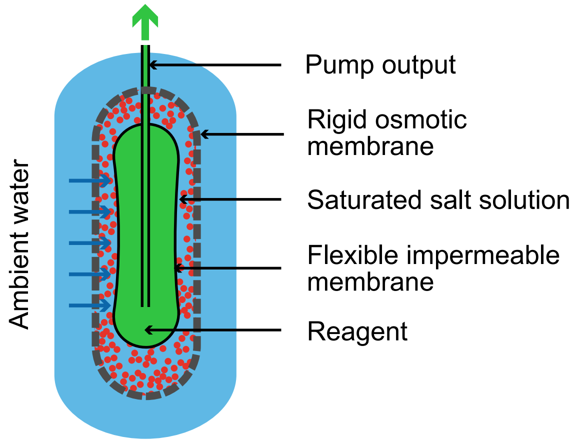

Figure 18: Operating principle of the miniaturized osmotic pump developed by Theeuwes and Yum for *in situ* delivery of a drug.[162] Adapted with permission from ref[163] in the application context of continuous monitoring of nitrate. Copyright 1994 American Chemical Society.

Initial concept– This type of pump dates back to a series of works in the mid-1970s concerning the development of biocompatible microsystems for autonomous delivery of small quantities of drugs (≤ 1 mL) at low flow rates $Q < 10$ μL/h.[162] This type of osmotic pump is also found for continuous nitrate analysis, when submersed in water, on time scales of several months.[163] The principle of such miniaturized pumps is illustrated schematically in Figure 18: it consists of a reservoir containing the drug or a reagent in contact with a movable partition with a closed reservoir of osmotic agents (e.g., a concentrated salt solution). This reservoir is itself encapsulated by a rigid semipermeable membrane and plunged in an aqueous bath. Because liquids are not compressible, the osmosis-driven flow through the membrane at a rate Q displaces the movable partition, thus pumping out the drug solution through the delivery orifice at the same volumetric rate.

Beyond leaks, concentration polarization, and membrane fouling, the conditions to ensure a constant delivery rate Q (see eq 20) consist of a negligible pressure difference ΔP induced by the flow itself and a constant driving force

$\Delta\Pi$.[162] These conditions are fully ensured by using a saturated solution of salts with an excess of solid, thus inducing a constant osmotic pressure that is much larger than the pressure drop induced by viscous forces, e.g., $\Delta P \ll \Delta\Pi \simeq 40$ MPa for a saturated sodium chloride solution (water activity $a_w \simeq 0.75$; see Table 1).[67] The elasticity of the membrane-bound compartment containing the osmotic agents can itself impact the dynamics, as shown by Bruhn et al., who measured the dynamics of pressure generation in deformable dialysis cassettes containing a draw solution and immersed in a water reservoir.[164] Similar concepts of osmotic passive pumps are now found in various commercial applications, see, for example, the push-pull osmotic tablets for the controlled release of possibly poorly water-soluble drugs or the miniaturized implantable pumps for research in laboratory animals, with drug volumes ≤ 1 mL and release durations up to weeks.[165,166]

Miniaturization – With the advent of microfabrication techniques, several protocols were developed to miniaturize such pumps at the microfluidic scales. Su et al., for instance, fabricated microchambers containing salt crystals in cellulose acetate chips to make microactuators.[167] In contact with a water reservoir, a large osmotic pressure difference was established, leading to a significant hydrostatic pressure that was able to deform mechanically the microdevice, as shown in Figure 19A.[167]

Using similar microfabrication techniques combining PDMS soft lithography and semipermeable membranes in cellulose acetate, the same group later designed a miniaturized version of the pump shown in Figure 18.[168] The pumps shown in Figure 19B can provide extremely low but stable flow rates ($Q \simeq 0.2$ μL/h) from small reservoirs ($\simeq 2$ μL) for potential biomedical applications. Following similar ideas, Chen et al. also developed protocols based on multilayer soft lithography to trap a concentrated sucrose solution within a closed microfluidic chamber.[170] Using the osmotic pressure difference between the sucrose solution and an external drop of water, a thin PDMS membrane was deformed and acted as a microfluidic valve. Again using similar concepts and microfabrication methods, but this time integrating a dense thermoplastic membrane in polyurethane, Peng et al. developed a microfluidic system only driven by an osmotic pressure difference for preprogramming sequences of constant-rate pumping alternating with pauses for minutes.[171]

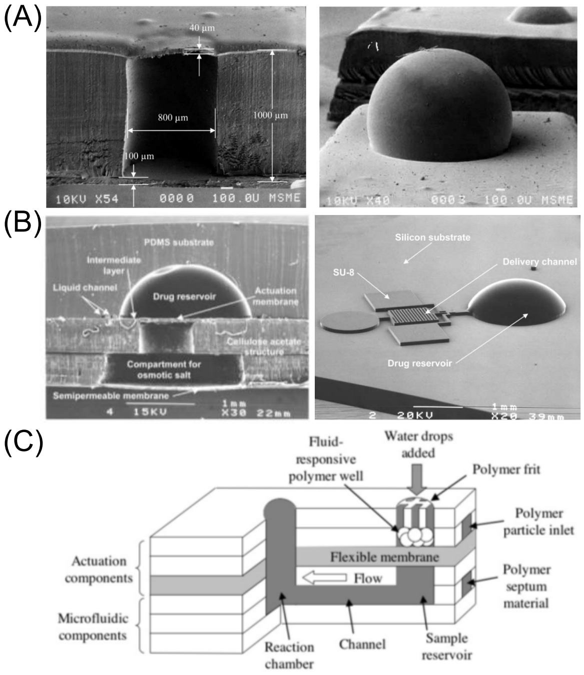

Figure 19: Osmosis-driven actuation. (A) (Left) cross-sectional scanning electron microscopy (SEM) image of a cellulose acetate microcompartment bounded on top by a thin membrane. (Right) SEM image of the microactuator immersed in water showing the deformation of the membrane; adapted from ref.[167] Copyright 2002 IEEE. (B) Water-powered drug delivery system. (Left) cross-sectional SEM image of the chip with the actuation and the semipermeable membranes. (Right) SEM image of the SU-8 mold for PDMS casting showing the hemi-spheric 2 μL reservoir; adapted from ref.[168] (C) Osmotic pumping with fluid-responsive polymer particles. Adapted with permission from ref.[169] Copyright 2007 Elsevier.

Fluid-responsive polymer particles – In the same spirit, osmosis-driven actuation using fluid-responsive polymer particles was also developed for pumping liquids at much higher flow rates and for shorter delivery times, $Q \simeq 10$-$20\ \mu$L/min for a few minutes,[169,172] Figure 19C. The driving force leading to the swelling of the hydrogel particles trapped in a reservoir in contact with a movable partition is due to the osmotic pressure difference between the interior of the polymer particle and the surrounding fluid. This osmotic pressure comes from the counterions associated with the ions bound to the polymer chains.[169,172] This driving force is, on the other hand, counterbalanced by the elasticity of the polymer network, which therefore plays a role in the swelling dynamics of the hydrogel and ultimately leads to an equilibrium state.

Many other demonstrations of the use of stimulus-responsive hydrogels have been reported for various microfluidic applications (valves, pumps, actuators, etc.), see, for instance, the review in ref[173] and refs[174–178] for examples of micropumps (not always passively-driven).

3.3.3 Osmotic passive pumping

Another class of pumping mode emerges among the works reviewed in the framework of autonomous osmosis-driven pumps: the use of a draw solution reservoir to pump fluids out of a microfluidic chip, as shown in Figure 17D. This pumping mode shares strong analogies with the works reviewed in section 3.1.4 using evaporation through (often external) microporous membranes or materials.

Remote reservoirs – In this context, Park et al. developed a protocol to bind a semipermeable cellulose membrane with small cutoffs (MWCO 2 kDa) on a PDMS cubic chamber ($10 \times 10 \times 10$ mm^3) as shown in Figure 20A. This device is capable of generating suction pumps for various microfluidic applications when submerged in a macroscopic reservoir ($\simeq$ 10 mL) of aqueous solutions of polyethylene glycol (PEG).[179] Such pumps were used to passively deliver pulse-free flow rates down to $Q \simeq 0.1\ \mu$L/h and thus generate stable chemical gradients of signaling molecules over an extended period of time (without renewing the external PEG bath) to study stem cell differentiation[180,181] or for mimicking *in vitro* perfusion culture.[182] Similar micropumps have been also used for microfluidic fuel cells to generate stable flows for several days without any energy input;[183] see also ref[151] cited earlier in the same context but using pervaporation. For this specific application, an air bubble in the outer tube connecting the pump to the chip prevents the mixing between the pure water (in contact with the draw solution through the membrane) and the fuel/oxidizer waste from the chip.

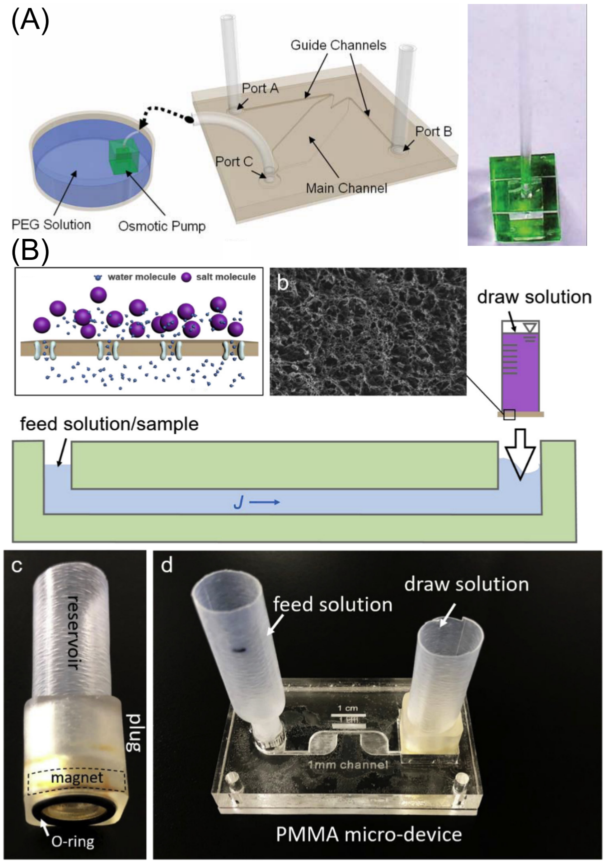

Figure 20: Osmotic suction for microfluidic pumping. (A) PDMS cubic osmotic micropumps (right) capable of generating suction pumping for microfluidic applications when immersed in a PEG solution (left). Adapted with permission from ref.[179] Copyright 2007 Royal Society of Chemistry. (B) Portable osmosis-driven micropump developed by Chuang et al. including magnetic assembly and sealing at the outlet of a chip. Adapted with permission from ref.[184] Copyright 2019 Elsevier.

Minimizing dead volumes – The examples cited earlier require a tube connecting the chip outlet to the PDMS cubic chamber and, thus, possibly large volumes of the liquid sample of interest. To minimize these volumes, called *dead volumes* in the following, Xu et al. made similar osmotic pumps in the context of microfluidic perfusion cell by directly integrating the semipermeable dialysis membrane (regenerated cellulose, MWCO 3.5 kDa) and the osmotic agents reservoir ($\simeq 3$ mL) at the outlet of a PDMS microfluidic chip.[185] Stable flows of culture medium for cell perfusion culture were demonstrated for days with polyvinylpyrrolidone (PVP) draw solutions leading to pumping rates down to $Q \simeq 0.1\ \mu$L/min.

Always with the idea of minimizing dead volumes, Chuang et al. developed a portable osmotic pressure drawing plug sealed at the outlet of a chip with simple magnetic assembly[184] as shown in Figure 20B. Such a plug integrates a semipermeable polyamide asymmetric membrane containing water channel proteins (aquaporins) and a $\simeq 5$ mL reservoir with NaCl as osmotic agents. Chuang et al. demonstrated that these plugs can generate stable flow rates up to $Q \simeq 30\ \mu$L/min for several hours.

Stability and mass transfer limitations – In the earlier works, the large volumes of the draw reservoir (a few mL) prevent significant dilution by the relatively low flow rates induced by osmosis (μL/h–μL/min); these remain stable for several hours without renewing the reservoir. Interestingly, stable osmotic flows are observed even when pumping liquids containing ions, as is often the case in many biological applications: phosphate-buffered saline (PBS), culture medium, etc.[185] This differs greatly from the evaporation-based micropumps discussed in section 3.1.4 for which the accumulation of nonvolatile solutes at the evaporation interface unavoidably limits the pumping efficiency at long time scales.[96] This is clearly an advantage for osmotic pumps because the molecular contaminants dissolved in the feed solution can pass through the membrane as soon as its pores are large enough. On the other hand, a decline in pumping efficiency may occur for feed solutions containing large biomolecules such as proteins that foul the membrane.[185] Similar effects were also reported for PEG molecules used as osmotic agents that block the pores of a dialysis membrane, thereby decreasing their permeability.[164]

It is also worth noting that most of the earlier works do not mention any mass transfer limitation due to dilutive ECP on the draw side, despite transmembrane osmotic fluxes up to several μm/s and osmotic agents possibly with small diffusion coefficients (e.g., aqueous polymer solutions such as PEG or PVP). Free convection within the draw reservoirs (with volumes of a few mL in the earlier-mentioned applications) is likely to play a role, preventing the formation of unstirred layers adjacent to the membrane. Correlations calculated, for instance, using boundary layer film theory could then be used to estimate the extent λ_o of the dilutive ECP as a function of the nature of the flow in the reservoir,[158] but we are not aware of any work along these lines in the context of the works presented earlier.

Reaching higher pumping rates – Because dilutive ECP does not appear to limit the transmembrane flow in the earlier works, the pumping efficiency can be simply increased by increasing the membrane surface A, often limited to a few cm^2 by the targeted microfluidic application. Jajack et al., on the other hand, performed a comparative study of different membranes commonly used for forward osmosis, nanofiltration, or dialysis applications, to maximize osmosis-driven flows up to a few μL/min for $\sim$ cm^2 membrane area,[186] see also section 4.2.

To reach significantly higher pumping rates, Chen et al. also integrated a dialysis membrane at the outlet of a PDMS chip but with a larger MWCO (20 kDa) and used water absorbing polymer particles instead of a draw solution.[170] Flow rates up to $Q \simeq 30\ \mu$L/min were reported but for shorter times ($\simeq 30$ min) due to the swelling equilibrium of the particles. Following a similar concept, Seo et al. also designed a hydrogel-based suction microfluidic pump using superabsorbent polymers to reach flow rates up to $Q \simeq 80$ μL/min for several hours.[178]

Osmotic pumping with hydrogels – Again using hydrogels but now directly integrated into a PDMS microfluidic chip, Shay et al. developed an osmotic microfluidic pump as shown in Figure 21 for portable health monitoring applications based on sweat collection at small flow rates ($Q \leq \mu$L/min).[187]

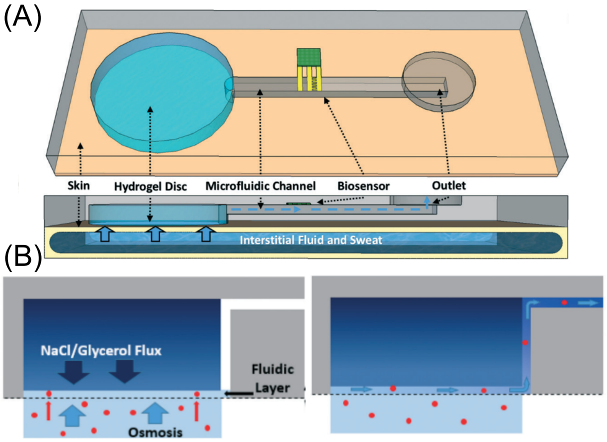

Figure 21: (A) Top and cross-sectional views of the chip developed by Shay et al. for continuous monitoring of sweat. The skin is modeled using a dialysis membrane. (B) *Push and pull* mechanism using a hydrogel saturated with mobile draw agents (NaCl/glycerol) inducing forward osmosis to draw a sweatlike fluid and pump it in the PDMS chip. Adapted with permission from ref.[187] Copyright 2017 Royal Society of Chemistry.

In this device, a hydrogel disk with a semicircular notch on its edge is inserted into a PDMS chip and sealed on one side by a dialysis membrane to mimic skin (MWCO 12-14 kDa). The entire device is then clamped onto a cell containing a PBS solution acting as sweat. As mentioned by the authors, fixed species attached to the hydrogel backbone, such as acrylate moieties, induce high osmotic pressure that causes fluid flow into the hydrogel, thereby swelling the hydrogel, but does not lead to a net flow to the microchannel in the PDMS device. When mobile osmotic solutes are previously dissolved in the hydrogel (NaCl or glycerol), the authors reported passive pumping of the liquid for a few hours, from the cell through the membrane and notch and toward the microchannel. This surprising mechanism, called *push and pull* by the authors, capable of continuously pumping the collected fluid in the microfluidic chip, cannot be simply explained by forward osmosis alone, and further studies are needed to understand its functioning.

3.3.4 Osmosis-driven sugar transport in plants

Generalities – Beyond the passive pumping applications mentioned earlier, the miniaturization of osmotic flows using microfluidic tools has made it possible to quantitatively explore mechanisms of sugar transport in plants. In a simplified way, plants have two vascular systems: the xylem, which allows passive water transport from the roots to the leaves (see Figure 5 and section 3.1), and the phloem, which carries sugars produced by photosynthesis from the source sites (mature leaves) to places where sugars are needed (sinks: fruits, roots, etc.)[66,76,188] The transverse dimensions of the phloem again lie in the microfluidic range, 10–50 μm, and sugars are passively transported by osmotic effects, the so-called Münch mechanism, or the pressure-flow hypothesis shown in Figure 22A. In this mechanism, sugars are first loaded inside the tubular phloem cells at the production organs, creating an osmotic pressure difference with the surrounding environment. This osmotic driving force induces a bulk flow that carries sugars along the phloem, possibly over long distances, to the sink organs where they are discharged.

Microfluidic Münch flows – Since the advent of microfluidic technologies, these have proven to be powerful tools for experimentally testing these transport mechanisms quantitatively, as these are difficult to probe experimentally *in vivo*.[66,76,188] Figure 22B illustrates one of the first works carried out by Jensen et al. in this context[189] (see also ref[190] for a similar study but at larger scales ∼ cm): A dialysis membrane separates two microfluidic channels, one filled with a concentrated solution (sucrose or dextran) and the other with water. Col-

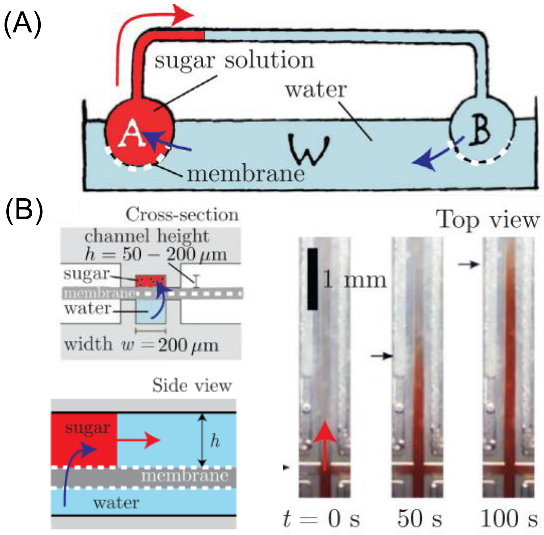

Figure 22: Osmosis-driven sugar transport. (A) Schematic setup used by Münch to demonstrate passive osmotic transport between flasks of high to low sugar concentrations immersed in water. (B) Microfluidic illustration of Münch osmotic transport of sugars along a channel separated by a dialysis membrane from a water channel[189] (top and sectional views). Adapted with permission from ref.[76] Copyright 2016 American Physical Society.

ored dyes then allow observation and measurements of the transport of the osmotic agents along the channel (at velocities ranging from 5 to 15 μm/s), induced by the difference in osmotic pressure across the membrane. In these works, the use of microfluidic tools is key not only to visually highlight the mechanisms of sugar transport in the phloem but also for a quantitative comparison with the models, thus boosting the understanding of these phenomena.[76,188]

These microfluidic illustrations of the Münch mechanism share some similarities with some passive osmotic pumps reviewed in section 3.3.3 but with the fundamental difference that the draw solution is confined in the microfluidic chip. The depleted layer of osmotic agents linked to the flow through the membrane (ECP) is key in this case because it only results from a balance between molecular diffusion and advection induced by the osmotic flow in the microchannel, the so-called *unstirred concentration boundary layer*.[191,192] This case contrasts with the examples mentioned earlier with macroscopic reservoirs of draw solutions, where free convection or even inertial flows are also likely to play a role in the dilutive ECP. In the case of the microfluidic Münch flow, the extent of the unstirred concentration boundary layer (and its variation along the channel) can only be predicted by modeling the shape of the osmotic flow and solute transport using the Stokes and convection-diffusion equations; see refs[191,192] and references therein.

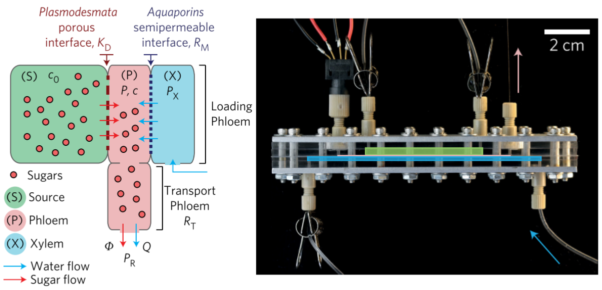

Figure 23: Multilevel chip developed by Comtet et al. to study the coupling between diffusive loading of sugars inside the phloem cells and their passive osmotic transport. Adapted with permission from ref.[193] Copyright 2017 Springer Nature.

Passive sugar loading – The contribution of microfluidics to the understanding of sugar transport in plants has once again been demonstrated by Comtet et al. with a chip allowing for study of the coupling between the long-distance transport of sugars and their passive loading inside the phloem cells by diffusion at the production sites.[193,194] This multilevel microfluidic chip shown in Figure 23 integrates two cellulose ester dialysis membranes with different MWCOs (and thus permeabilities $\mathcal{L}_p$) to induce both a bulk flow similar to that of the Münch mechanism and a resistance to the diffusive loading of the sugars (here dextrans) from the source to the phloem. Here again, the versatility of microfluidic tools in which the different resistances to mass transport can be adjusted (e.g., by playing with the geometry) makes it possible to validate simplified transport models and to highlight the relevant limiting regimes for real trees.[193]

Toward novel membrane integrations? – Importantly, for most of the works mentioned earlier (also including those discussed in sections 3.3.2 and 3.3.3), membrane integration is a critical technological issue due to the poor compatibility between commercial membranes and the standard microfluidic chip materials such as PDMS. Despite their extreme utility, current solutions such as mechanical clamping or the bonding of membranes to prevent leaks deserve a technological breakthrough. There is no doubt that *in situ* manufacturing technologies of nanoporous membranes (see refs[195–200] for some examples using photopolymerization) can allow finer observations of osmosis-induced flows because the membranes can then be integrated transversely to the channels and not as a distinct layer possibly hindering observations.

4 Passive concentration: from dilute to concentrated solutions, and even solids

4.1 Generalities

In section 3, we reviewed works that use osmosis, pervaporation, or evaporation through fixed interfaces for microfluidic passive pumping applications. As shown schematically in Figure 24A, the drop in water potential $\Delta\Psi = \Psi^\star - \Psi_{\text{ext}}$, with $\Psi^\star$ being the water potential upstream of the interface and Ψ_{ext} being the one imposed downstream, drives a net solvent flux J through the interface, either a membrane for osmosis and pervaporation, or a fixed gas/liquid interface for evaporation.

This flux transports by advection the solutes contained in the liquid (from ions to colloidal species) toward the interface, which, in turn, inevitably leads to an increase in the concentration of solutes in the microfluidic chip, as long as they are nonvolatile in the case of evaporation or fully rejected by the membrane for osmosis and pervaporation. As mentioned throughout section 3, the increase of the solute concentration can be a detrimental issue as it can limit the pumping efficiency: fouling of the membranes[71] and concentrative ECP for forward osmosis,[185,186] or even salt crystallization in the case of evaporation-based micropumps.[96,102] Beyond this seemingly harmful problem, section 4 will mainly show how to exploit this same phenomenon to concentrate solutes in a chip, passively and in a controllable way, for many different applications.

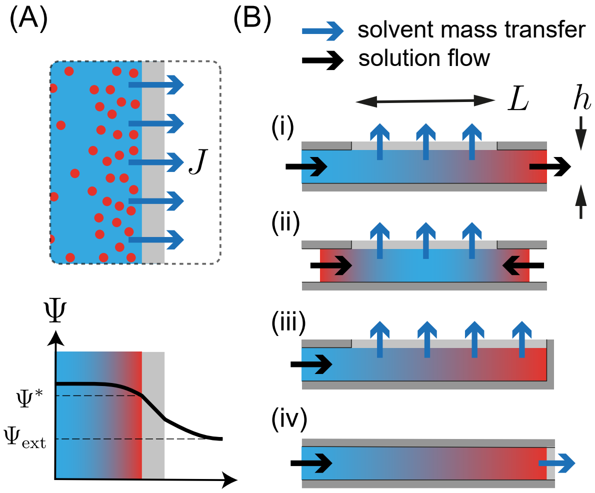

Figure 24: Passive solute accumulation. (A) Solvent flux J across the fixed interface driven by a drop along the water potential profile Ψ. The gray region corresponds to a semipermeable membrane in the case of osmosis and pervaporation or to the gas-liquid interface (including the boundary layer in the gas phase) in the case of evaporation. (B) Different geometrical configurations for microfluidic passive solute concentration. The light gray zones indicate the solvent-permeable interface, and the colors demonstrate the solute concentration. In each case, the dimensions are typical of microfluidic chips: h is in the range 10–100 μm and $L \sim 1$ cm.

The dynamics of the solute concentration in the microfluidic chip depends on several parameters such as (i) the geometry of the device including the interface, (ii) the magnitude of the driving force $\Delta\Psi$, and (iii) the solute transport by diffusion and advection in the liquid phase. As discussed in section 2.2, the driving force depends on the physicochemical properties of the solution: $\propto (a_w - \text{RH})$ for evaporation and pervaporation and $\propto \Delta\Pi$ for osmosis. Table 1, along with the kinetic equations derived in section 2.2, can then be used to predict the flux J. Because solute transport in the liquid phase also depends on the physicochemical properties of the solution, the dynamics of solute accumulation upstream of the interface depends not only on the process but also on the chemical nature of the solute: from molecular species to macromolecules and colloids.

As suggested in the previous paragraph, there are thus multiple ways to classify works on passive solute concentration in a microfluidic chip: according to the process (evaporation, pervaporation, or osmosis), the geometry, the nature of the solutes, or the underlying applications. In this review, we have chosen to sort the different research and applications according to the geometries, as shown in Figure 24B. This choice of classification, possibly surprising at first sight, will allow us to highlight in the following sections, the differences and similarities between the various passive mass transport mechanisms for each geometry, and to underline the importance played by the physicochemical nature of the solutes on their accumulation.

This division into four different geometries also makes it easier to relate the different works listed below to distinct applications. In Figure 24B(i), it is, for example, a matter of the continuous removal of solvent of a liquid phase flowing in a microchannel,[201] mainly for applications concerning the preconcentration of analytes before detection to overcome sensitivity limits.[202] In Figure 24B(ii), the focus is on concentrating microvolumes (e.g., droplets) primarily in this case for applications in the screening of phase diagrams of soft matter systems or protein crystallization conditions. Finally, the configurations shown in Figure 24B(iii,iv) allow the continuous accumulation of solutes in a dead-end microchannel, especially for the engineering of micromaterials, starting from molecular or colloidal building blocks.

Finally, due to the high aspect ratios of the geometries shown in Figure 24B, with height $h \ll$ length L, 1D modeling of transport phenomena is often sufficient to describe the kinetics of solute concentration in these configurations. The following classification into four geometrical configurations, far from being exhaustive, will therefore also allow us to establish parallels between different applications in terms of mass transport modeling.

4.2 Continuous membrane-assisted preconcentration

We first start with the steady configuration shown in Figure 24B(i) for a binary mixture solvent and solute. The solvent is removed through a fixed interface positioned tangentially to the microfluidic channel, increasing the concentration of the solution flowing under the interface, and the solutes are assumed to be fully rejected.

4.2.1 Evaporation

Since the early work of Timmer et al.,[29] this microfluidic configuration has been reported several times for evaporation using membrane-assisted solvent removal,[203,204] a configuration similar to membrane distillation[205] as shown in Figure 25A. Typically, a hydrophobic porous membrane (with pore sizes r_p in the micrometer range) is clamped between two aligned microfluidic channels, leading to an exchange area $\simeq (L \times w)$, with w being the channel width; see Figure 25B for an example.

The membrane acts as a barrier for the liquid phase, provided that the liquid pressure does not exceed the capillary penetration pressure $P_c \sim \gamma/r_p$ ($P_c \sim 100$ kPa for water and pore size $r_p \sim 1$ μm). However, the membrane remains permeable to the vapor phase, mostly by diffusion through its pores, as shown in the inset of Figure 25A. This microfluidic configuration has strong analogies, in terms of both dimensions and mechanisms, with gas-liquid contactors that use hydrophobic porous hollow fibers; see e.g., ref.[207]

In the same context, Zhang et al. developed microfabrication protocols to directly integrate an ultrathin silicon-rich silicon nitride layer (SiRN) with an array of micromachined holes as shown in Figure 25C, thus playing the role of a model membrane with controlled pore size

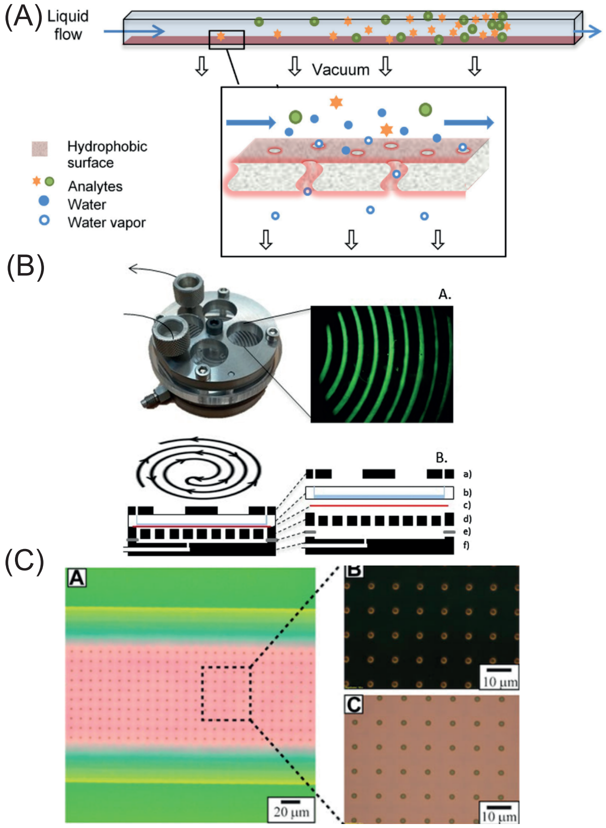

Figure 25: Continuous preconcentration based on evaporation. (A) Analyte concentration using microfluidic membrane-assisted evaporation. (B) Chip developed by Fornells et al. with a spiral-shaped microchannel and observation windows (top). Cross-sectional view (bottom) showing the liquid flow channel (b), the membrane (c), and the air flow channel (d). Adapted with permission from ref.[204] Copyright 2017 Elsevier. (C) Microscopic images (dark and bright fields) of the SiRN membrane developed by Zhang et al. Reproduced with permission from ref.[206] Copyright 2016 John Wiley and Sons.

and density.[206] Continuous solute concentration in the configuration shown in Figure 24B(i) also has been demonstrated without a membrane but using hydrophobic micropillars inside a PDMS microchannel.[208] The array of micropillars is able to fix a gas-liquid interface transversely in the channel, but the relatively large distance between the pillars ($\simeq 50\ \mu$m) narrows the operating pressure range for its stability as compared to microporous membranes.

These microfluidic systems are particularly relevant for preconcentrating analytes when solutions are very dilute in order to meet the sensitivity requirements of analytical tools. For a well-mixed solution at the outlet and assuming that the nonvolatile solutes do not adsorb within the channel, the solution and solute mass balances shown in Figure 26 lead to the following concentration enhancement factor:

$$\frac{C_{\mathrm{out}}}{C_{\mathrm{in}}} = \frac{1}{1 - Q_e/Q_{\mathrm{in}}}\,, \tag{22}$$

where Q_e is the overall solvent flow rate through the interface (m^3/s), Q_{in} is the incoming flow rate, and C_{in} and C_{out} are the incoming and outgoing solute concentrations, respectively. Assuming for simplicity a rectangular channel of cross section $h \times w$ and a uniform solvent flux J (m/s) over the interface $L \times w$, the previous mass balance becomes:

$$\frac{C_{\mathrm{out}}}{C_{\mathrm{in}}} = \frac{1}{1 - (L/h)(J/V_{\mathrm{in}})}\,, \tag{23}$$

with $V_{\mathrm{in}} = Q_{\mathrm{in}}/(hw)$ (m/s) being the inlet flux. This relation highlights the relevance of the tangential microfluidic configuration, $L \gg h$, to obtain the highest enhancement factor.

Most of these works are motivated by an efficient and fast preconcentration of dilute analytes, thus obtaining the highest ratio $C_{\mathrm{out}}/C_{\mathrm{in}}$ even for a large incoming flux V_{in}. Evaporation through the membrane therefore is often improved by heating the device and by an active water vapor removal using either vacuum or a dry sweep gas in the permeate channel, with room for optimization through simulations of vapor transport,[203] for instance.

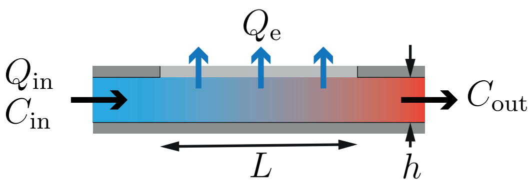

Figure 26: Solute concentration assuming homogeneous concentration over the transverse dimensions of the channel. The gray line corresponds to the evaporation membrane. The other symbols are explained in the text.

Even if not always specified in the earlier-cited works, we estimated from the data that the water flux J through the membrane ranges from 0.1 to 10 μm/s depending on the experimental conditions, and enhancement factors up to $C_{\mathrm{out}}/C_{\mathrm{in}} \simeq 10$ often have been reported. The evaporation driving force remains mostly unaffected by the presence of the solutes in the liquid phase because the solutes are very dilute and the water chemical activity given by eq 3 is $a_w \simeq 1 - V_m C \simeq 1$. On the other hand, adsorption of solutes or other impurities onto the membrane can block its pores[206] or cause water leak by hydrophilization of the hydrophobic membrane.

4.2.2 Pervaporation in PDMS chips

We are not aware of works that use pervaporation across dense PDMS membranes to concentrate analytes in an aqueous solution continuously flowing in a microchannel, as for the applications discussed earlier based on membrane-assisted evaporation; see Figure 25. This is probably due to the fact that the water fluxes are too low, e.g., $J \simeq 30$ nm/s using the 1D model described by eq 18 for a PDMS membrane of thickness $\delta \simeq 30$ μm separating pure water and dry air at room temperature.

However, microfluidic chips using pervaporation through a dense membrane also have been reported multiple times for a closely related application, on-chip continuous removal of volatile organic compounds from aqueous solutions: acetone in ref,[209] ethanol for purification of radiopharmaceutical formulations in ref,[210] and methanol for concentrating hydrogen peroxide solutions in refs.[145,211] In these applications, pervaporation is not used to concentrate solutes in an aqueous phase, which is an unusual experimental configuration for large-scale pervaporation processes, but instead in a standard configuration involving removal of traces of organic compounds from aqueous solutions. Both configurations nevertheless have strong similarities, especially regarding the description of mass transport.

Here, PDMS is a material of choice for the membrane because it is known for its high permeability to certain organic solvents, and Figure 27 shows some typical devices where the membrane is either sandwiched in between two glass microfluidic channels[209] or directly built in during the fabrication of the chip by soft lithography.[145,210,211] As earlier, a dry sweep gas or partial vacuum on the permeate side is used to improve the overall removal rate of the organic solvents.

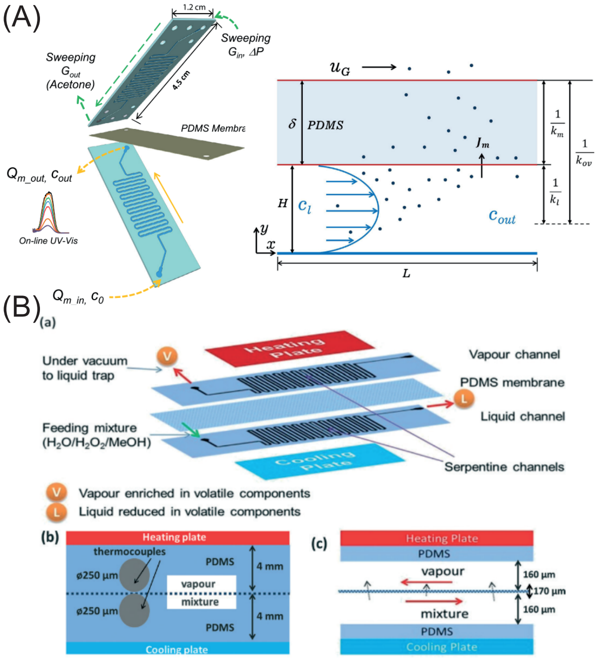

Figure 27: Removal of organic solvents based on pervaporation. (A) (Left) Exploded view of the microfluidic glass device developed by Zhang et al. integrating a PDMS membrane for the removal of acetone from water. (Right) 2D transport showing the resistances to mass transfer: diffusion in the liquid phase and across the membrane. Adapted with permission from ref.[209] Copyright 2016 Elsevier. (B) General overview, cross-sectional view, and side view of the PDMS chip developed by Ziemecka et al. for removing methanol by pervaporation from hydrogen peroxide–water–methanol mixtures. Adapted with permission from ref.[211] Copyright 2015 Royal Society of Chemistry.

The description of the separation efficiency shares *a priori* strong similarities with the membrane-assisted evaporation configurations discussed earlier, and Zhang et al. used a 2D model of solute transport to evaluate the different resistances: solute diffusion across the depleted boundary layer under the membrane and solvent diffusion across the membrane.[209] These works demonstrate that precise control of the channel geometry (including the membrane thickness) and the temperature, coupled with the very high surface/volume ratio and control of the flow, offers the prospect of continuous and miniaturized pervaporation-based separation processes with high yields.

4.2.3 Forward osmosis

Finally, a few publications also report a configuration similar to that described in Figure 24B(i) in the specific case of passive solvent transport caused by an osmotic pressure difference across a semipermeable membrane. Specifically, Skou et al. developed a microfluidic chip integrating a dialysis membrane (MWCO 3.5 kDa) mechanically clamped between two microstructured PDMS layers.[213] Such a chip was developed not only for buffer exchange of protein solutions by dialysis, but also to continuously concentrate protein solutions using forward osmosis and PEG solutions as osmotic agents. Combined UV and small-angle X-ray scattering measurements at the chip outlet demonstrated significant preconcentration of protein samples, paving the way for the study of structural changes of biomolecules by concentration.

Jajack et al. also developed a microfluidic chip, but it incorporated an asymmetric membrane normally used for forward osmosis, covering a serpentine microfluidic channel made by laser cutting in a double-sided tape,[186] as shown in Figure 28A. A macroscopic reservoir (∼ mL) of phosphate-buffered saline (PBS) placed above the membrane played the role of the draw solution. Jajack et al. then demonstrated continuous preconcentration of biologically relevant solutions, glucose and bovine serum albumin, in dilute PBS flowing under the membrane. Their study shows that membrane fouling by biomolecules in this frontal configuration is minimal when the channels are in contact with the thin active layer of the asymmetric membrane and, thus, when the active layer faces the feed solution. Interestingly, and in contrast to the cases discussed earlier using evaporation and pervaporation, the increase in concentration of the PBS solution along the channel can lead to an equilibrium of the osmotic pressures and, thus, to a vanishing driving force $\Delta\Pi$ for the solvent flux. This regime is observed only for low input flow rates, so that the residence time in the chip allows the equilibrium concentration to be reached at a given position along the channel. This picture was validated using a simple transport model (assuming homogeneous concentration over the channel height) and experimental measurements of concentration factors $C_{\text{out}}/C_{\text{in}}$ and of concentration profiles at various input flow rates (using conductimetry and sodium chloride solutions). This feature, specific to the osmotic transport, opens the possibility of quantifiable and continuous preconcentration of liquid samples, only controlled by the osmotic pressure ratio between the reservoir and the sample independently of the input flows, at least for small flow rates.

Jin and Verkman used a similar microfluidic technique, not to preconcentrate a solution, but inversely to estimate the hydraulic permeability $\mathcal{L}_p$ of a monolayer of epithelial cells subjected to an osmotic pressure difference.[212] More precisely, the authors developed a dedicated microfluidic setup, shown in Figure 28B, with a Snapwell insert (a circular plastic cup with a porous filter, pore size 0.4 μm) containing cultured cells overlying a microfluidic channel with a serpentine shape to maximize the surface/volume ratio, see the term L/h in eq 23 ($L = 10$ cm and $h = 20$ μm in ref[212]). An osmotic pressure difference (up to $\Delta\Pi \simeq 10$ MPa) across the epithelial monolayer is imposed by filling the Snapwell compartment with a membrane-impermeant sugar solution (raffinose). The osmotic flow through the cell monolayer is then revealed by the concentration increase along the channel of a cell-impermeant fluorescent dye flowing in the microfluidic channel (typical input flow rates $Q_{\text{in}} \simeq 0.5$–10 μL/h). The measurement of the steady concentration profile of the inert dye makes it possible to precisely estimate the hydraulic permeability of the epithelial mono-

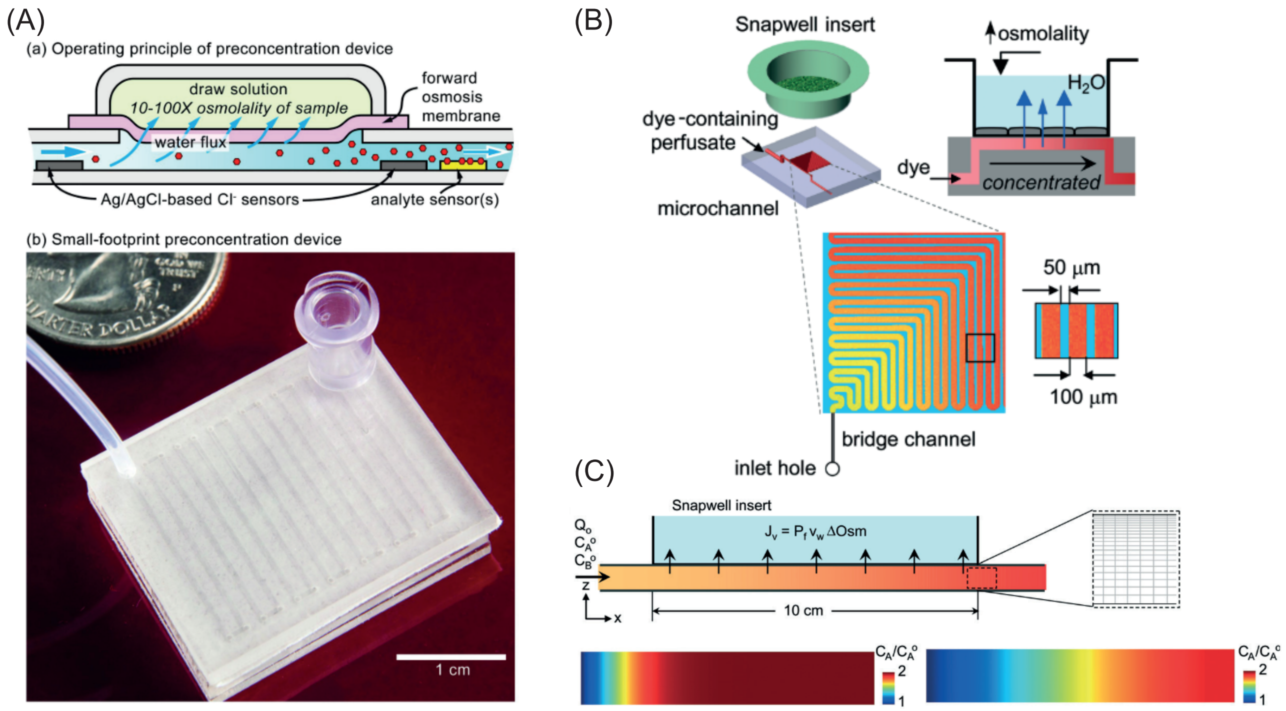

Figure 28: (A) (Top) Principle of preconcentration by forward osmosis through a semipermeable membrane. (Bottom) Microfluidic chip integrating a nanoporous membrane superimposed on a serpentine channel, and covered by the draw solution. Adapted from ref.[186] Copyright 2019 PLoS ONE under CC BY 4.0 license. (B) Microfluidic platform for rapid measurement of transepithelial water transport. Forward osmosis through the epithelial monolayer leads to a concentration increase of a cell-impermeant fluorescent dye flowing in the serpentine channel. (C) Corresponding optimization using 2D modeling of solute transport along the channel. Adapted with permission from ref.[212] Copyright 2017 Royal Society of Chemistry.

layer, and transepithelial water fluxes down to $J \simeq 100$ nm/s could be measured.

As in the case of Jajack et al., the concentration increase along the channel decreases the osmotic driving force $\Delta\Pi$, to possibly reach an osmotic pressure equilibrium for small incoming flow rates and, thus, uniform dye concentration downstream. To fully validate their measurements and in particular to quantify the possible build-up of concentrative CP due to the small diffusion coefficient of the fluorescent dye, Jin and Verkman also performed numerical simulations of the solute transport in the liquid phase (see Figure 28C) similarly to those of Zhang et al. but for pervaporation,[209] as shown in Figure 27A. Such configurations and models also share strong analogies with cross-flow ultrafiltration,[159] a pressure-driven process that is therefore beyond the scope of this review.

4.3 Passive microfluidic concentration in confined volumes

4.3.1 Generalities

We now turn to the geometrical configurations shown in Figure 24B(ii) corresponding to microvolumes of aqueous solutions, 1 nL–10 μL, confined in a microfluidic system; see also Figure 29.

The first configuration corresponds to a fixed volume of solution defined by a dead-end channel, while the second corresponds to a 2D droplet squeezed in a microfluidic chamber. In both cases, solvent passive mass transport occurs through a fixed interface positioned tangentially to the liquid volume, through either evaporation, pervaporation, or osmosis, similarly to the examples discussed in the previous section. In this specific configuration, however, the removal of solvent from the confined volume continuously reduces its volume, thus increasing the concentration of the solutes it contains. Interestingly and as will be discussed later, reversing the imposed driving force is also possible and yields an increase of the volume and thus dilution of the solutes.

Such experimental configurations are easily implemented in microfluidic systems, either using membrane-assisted evaporation in devices similar to those shown in Figure 25 or using two-phase flow microfluidics and PDMS chips. Because PDMS is not permeable to salts and many macromolecules such as polymers and biomolecules, such microfluidic configurations in PDMS chips have proven to be particularly relevant for screening the phase diagrams of soft matters systems or protein crystallization conditions.

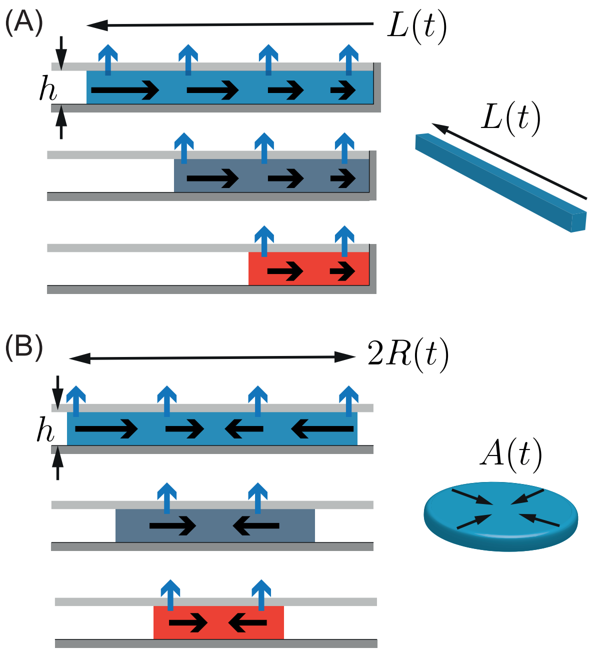

Figure 29: (A) Draining of a dead-end microchannel filled with a solution by passive transport of solvent through the interface (gray). The colors code the continuous increase of solutes trapped in the volume. (B) Similar configuration but for a 2D drop squeezed in a microfluidic chip. Arrows in both cases indicate flows within the confined volume induced by the water flux across the interface.

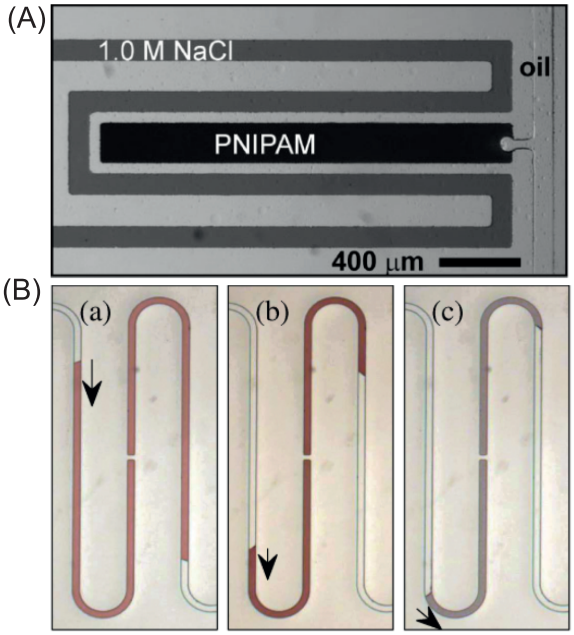

Figure 30: Screening of phase diagrams using confined volumes in dead-end microchannels. (A) Osmosis-induced concentration of an aqueous polymer solution in a microchannel to determine its phase diagram. Adapted with permission from ref.[214] Copyright 2008 John Wiley and Sons. (B) Pervaporation-induced emptying of microchannels (width 50 μm) filled with a dispersion of gold nanoparticles. Homogeneous colors, due to the plasmonic response of the nanoparticles, indicate homogeneous concentration along the channels. In (c), colors turn to gray because of the destabilization of the dispersion. Adapted with permission from ref.[142] Copyright 2015 Royal Society of Chemistry.

4.3.2 Dead-end microchannels

Osmosis – Concerning the linear geometry shown in Figure 29A, Zhou et al. developed a single-layer PDMS chip with a 2 mm long dead-end microchamber ($\simeq$ 40 nL) surrounded by a microchannel (Figure 30A[214]). PDMS is essential not only for its gas permeability to fill the dead-end channel with an aqueous solution but also for its hydrophobic properties to obtain a fixed volume with partial wetting conditions with a flowing inert oil (paraffin in this case). A concentrated salt solution flowing in the channel surrounding this chamber induces forward osmosis through the thin PDMS walls ($\delta \simeq$

50 μm), therefore emptying the microchamber, with the volume of water lost being replaced by oil from a reservoir. Zhou et al. used this setup (on a hot plate) to concentrate aqueous solutions of poly(N-isopropylacrylamide) (PNIPAM) and construct their phase diagrams, concentration versus temperature. Indeed, the average polymer concentration $\langle C \rangle$ is estimated based on solute conservation within the confined volume by measuring its length $L(t)$ using:

$$\langle C \rangle L(t) = C_0 L(t = 0)\,, \tag{24}$$

with C_0 being the initial polymer concentration. Any event happening during the decrease of the volume for instance the occurrence of turbidity due to a phase transition (cloud point) can be related to the polymer concentration simply by the measurement of the length $L(t)$. It is a dynamic exploration of a phase diagram. However, and as mentioned by Zhou et al., the small osmotic driving force imposed using a concentrated sodium chloride solution, and thus with water chemical activity $a_w > 0.75$,[67] prevents rapid exploration of phase diagrams in such PDMS devices, with typical times on the order of 30 h to concentrate solutes only by a factor of 3.[214] This microfluidic device nonetheless allows phase diagrams to be determined with a minimal amount of sample and paves the way for exploring multiple conditions on a single chip using appropriate designs of the microfluidic channel network.

Pervaporation – Later, Ziane et al. developed a similar PDMS chip but for confining two identical volumes ($\simeq$ 20 nL) of aqueous solutions in two facing dead-end microchannels (length 1.5 cm, height $h \simeq 30$ μm) embedded in a thin PDMS layer[142] (Figure 30B). In this case, emptying of the channels with a serpentine shape occurs due to water pervaporation in ambient air of relative humidity RH through the PDMS layer above the channels (thickness $\delta \simeq 30$ μm) and, therefore, at a higher rate than for the osmotic experiments discussed earlier [driving force for pure water $\propto (1 - \text{RH})$]. The typical emptying time of the channel filled with pure water can be estimated by the characteristic time scale $\tau = (hw)/q$, where q (m^2/s) is the pervaporation rate per unit length. Estimates of q given by eq 17 give emptying times on the order of 1–2 h. The volume of water lost by pervaporation is replaced in this case by fluorinated oil from a reservoir connected to the chip. Ziane et al. also recognized that solutes concentrate homogeneously within the confined volumes, even for centimetric $L(t)$ and regardless of the nature of the solutes, from ions to colloids.[142] This feature is not related to molecular diffusion along the channel because the associated time scales $\sim L^2/D$ are too long, with D being the diffusion coefficient of the solute. This result is related to the homogeneous pervaporation rate q along the channel and the relatively fast concentration homogenization by diffusion across the transverse dimensions, which is translated using scaling arguments by:[142]

$$\frac{h^2}{D\tau} \ll 1\,. \tag{25}$$

In this regime, solute concentration is almost homogeneous over the transverse dimensions of the channel, and the pervaporation-induced flow along the channel shown in Figure 29A transports solutes and concentrates them at each location at the same rate.[142] Therefore, eq 24 is strictly valid even with C instead of the average concentration $\langle C \rangle$ because the concentration of solutes remains homogeneous during the emptying of the channel. Beyond the scaling arguments leading to eq 25, a more appropriate description using, for example, a dispersion equation derived using Taylor-like approaches[215] is still needed to fully and quantitatively evaluate the validity domain of this regime.

This specific feature has been exploited to establish the phase diagrams of multicomponent aqueous solutions without any other measurement than the length $L(t)$ of the confined volume (even for centimetric L): measurements of the stability threshold of charge-stabilized dispersions of gold nanoparticles as shown in Figure 30B, stability of carbon nanotubes dispersed in water by copolymers,[216] and liquid–liquid phase separation in aqueous salt/polymer solutions.[142]

Pervaporation in such devices also offers the possibility to explore very concentrated zones of the phase diagrams, even solids, because the driving force for pervaporation $\propto (a_w - \mathrm{RH})$ only vanishes when the water chemical activity a_w of the solution reaches the ambient relative humidity. Solid forms and directional solidification of solutes inside the PDMS microfluidic channel may happen but can induce significant distortion of its shape.[217–219] Determination of the volume solely by measurements of its length $L(t)$ thus can induce misleading values for the concentration C. We will address this question in section 4.4 when examining the fabrication of micromaterials by pervaporation in PDMS chips.

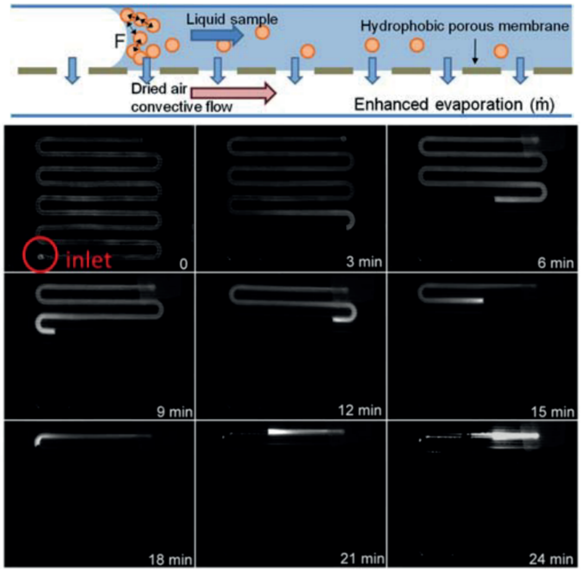

Figure 31: Similar configuration as in Figure 30B but for membrane-assisted evaporation in the context of point-of-care diagnostics. Evaporation-induced emptying of the serpentine channel (width 1.7 mm) concentrates fluorescent tracers. Concentration gradients are evidenced at the moving meniscus. Adapted from ref.[220] Copyright 2013 MDPI under CC BY 4.0 license.

Evaporation – Similar microfluidic setups, shown in Figure 31, were also developed by Zhang et al. but with membrane-assisted evaporation through a microporous hydrophobic membrane instead of pervaporation or osmosis through PDMS.[220,221] The fabrication and operation of such microfluidic chips are also similar to those discussed in section 4.2 for continuous solute concentration, with a dry sweep gas to enhance evaporation on the permeate side. However, no continuous flow is imposed in this case, and the dead-end channel simply drains by evaporation of water through the membrane. Such devices were specifically developed for point-of-care diagnostics to concentrate samples containing bacteria or viruses and detect clinically relevant pathogens. The dynamics of concentration inside the channel *a priori* follows the same mechanisms as those described by Ziane et al. for pervaporation.[142] However, because of the relatively large height of the channel ($h \simeq 200$ μm) and the small diffusion coefficients D for bacteria and viruses, the inequality eq 25 is not fully verified, and molecular diffusion is not strong enough to rapidly homogenize concentrations over the channel transverse dimensions during the emptying of the channel. Concentration gradients superimposed to the homogeneous concentration along the volume therefore are visible at the moving meniscus in this case, as shown in Figure 31. Nonetheless, the portable, disposable devices developed by Zhang et al. allow efficient concentration of viral samples (from $\simeq$ 1 mL to 10 μL) to increase the sensitivity of point-of-care molecular diagnostics.[220] In addition, these devices can achieve high and controlled concentration levels within minutes (as long as the length L is measured), which are major advantages over conventional techniques such as ultracentrifugation, particularly for point-of-care diagnostics.

In such works, solute absorption on the hydrophobic membrane is a critical issue that can prevent optimal operating conditions, and drag forces due to the moving air/solution meniscus play a key role. Similar microfluidic chips have also been developed by Tseng and Van Dam with the same operating conditions but as an alternative to rotary evaporation for concentrating positron emission tomography tracers.[222] In this case, however, a preconcentration step before emptying the channel by evaporation is performed by connecting the channel inlet to the solution reservoir for a given time. We will come back to this concentration mode in detail in section 4.4.

4.3.3 2D squeezed droplets

First demonstration – Regarding the 2D geometry of squeezed droplets shown in Figure 29B, in 2007 Shim et al. developed a multilevel PDMS microfluidic chip that allowed one to explore in a controlled way the phase diagram of multicomponent aqueous solutions.[143] This chip allowed one to generate and store droplets (using two-phase flow microfluidics), in an array of wells located above a thin PDMS membrane separating these droplets from channels in which a solution imposing a given water chemical activity a_w was flowing (Figure 32A). The difference in chemical activity across the membrane caused an osmotic transport of water, resulting in shrinkage or swelling of the drops, thus concentrating or diluting the solutes they contained.

As for the linear geometry discussed earlier (see eq 24), measurements of the drop area $A(t)$ yield estimates of the concentration of any solutes inside the drop, assuming that the latter do not permeate PDMS. As suggested by Ziane et al.,[142] the same mechanisms of homogeneous concentration should also occur *a priori* for the 2D geometry regarless of the diffusion coefficients of the solutes, provided that the water flux on the drop surface is homogeneous and that inequality eq 25 is verified. Assuming 1D mass transfer across the PDMS membrane using the solution-diffusion model (see eq 8, also including water leak through the whole PDMS chip), Shim et al. provided quantitative modeling of the shrinkage/swelling dynamics of the stored drops. Shim et al. then used this chip to quantitatively determine the phase diagram of a polymer/salt mixture showing a liquid-liquid phase separation, as shown in Figure 32B.[143]

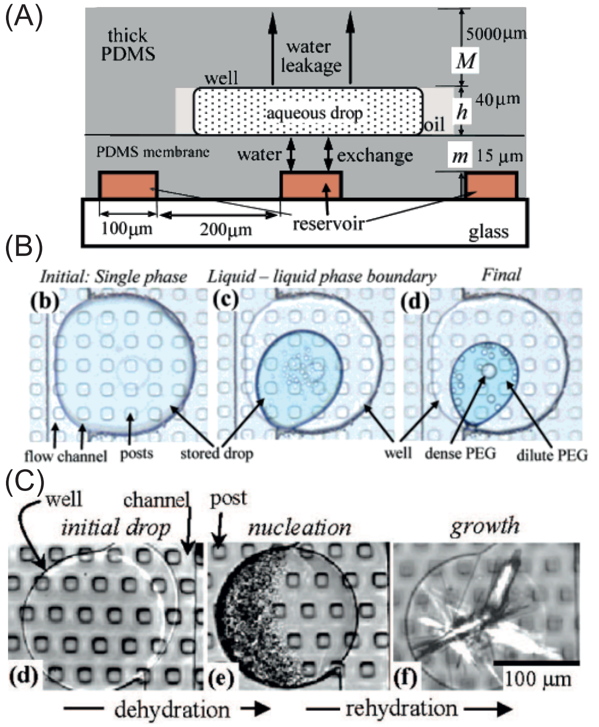

Figure 32: Screening of phase diagrams using 2D droplets and osmosis. (A) Cross-sectional view of the PDMS chip developed by Shim et al. A solution imposing a fixed water activity is flowing in channels (orange cross sections). (B) Top views of a drop of an aqueous mixture evidencing a liquid-liquid phase separation. Adapted with permission from ref.[143] Copyright 2007 American Chemical Society. Solute concentrations are determined by measurements of the drop area $A(t)$. Drops are stored in rectangular chambers, and the PDMS membrane is supported by 30 μm square posts. (C) Same device illustrating how dynamic osmotic control of the drop volume can be exploited to decouple nucleation and growth of protein crystals. Adapted with permission from ref.[223] Copyright 2007 American Chemical Society.

Protein crystallization – Since this pioneering work,[143] many microfluidic chips exploiting osmosis (or pervaporation) through a thin PDMS membrane have been developed for studying protein crystallization in nanoliter droplets. For instance, the possibility of decoupling the nucleation and growth stages of protein crystals was first illustrated by Shim et al.[223] using the dynamical control of the droplet volume offered by osmosis, as shown in Figure 32C. Using a similar microfluidic chip but also integrating capillary valves to store the droplets[224] and cross gradients of temperature and imposed osmotic driving force, Selimović et al. demonstrated fine screening of phase diagrams of aqueous solutions of proteins in the composition versus temperature plane with minute amounts of solutions, $\simeq 1000$ different conditions using only $\simeq 2$ μL of sample.[225] Likewise, Lau et al. developed a platform combining large-scale integration of microvalves, two-phase flow microfluidics, and osmosis through a thin PDMS membrane for high-throughput screening of crystallization conditions, up to 1000 assays/cm^2 in stored drops of a few nanoliters[226] (Figure 33A).

Devices similarly exploiting osmosis through a thin PDMS membrane but working without microvalves and pumps have been also developed by Luo et al.[227] and by Morais et al. to explore the phase diagram of a full-length monoclonal antibody with its crystallizing agents.[228] Hansen et al. also developed a microfluidic device integrating both micromechanical valves and a thin PDMS membrane to add kinetic control by osmosis (or pervaporation) on the diffusive mixing of proteins and precipitants in microvolumes, the so-called free-interface diffusion[229] shown in Figure 33B. In this chip, water mass transport across a thin PDMS membrane from/to an open *osmotic bath* can be used to kinetically optimize protein crystallization.

In the context of protein crystallization using PDMS chips, but without a membrane for osmotic control as earlier, water loss by pervaporation through the PDMS matrix has been recognized as a critical issue for long-term incubation of aqueous solutions in microcompartments or droplets. Mitigation of dehydration has been demonstrated by placing the whole microdevice into a chamber with controlled humidity,[230,231] by integrating a large reservoir in the chip for osmotic control using aqueous solutions,[232,233] or even by using freezing[234] or coatings to suppress pervaporation.[235] Shim et al. also showed that the content of the stored volumes can even be changed by exploiting the permeability of PDMS to small molecules, as demonstrated for ethanol and quorum sensing molecules in ref.[236] We will not present similar works hereafter, because the considered process, which is close to dialysis, does not fit in the framework of this review.

Phase diagram screening without membranes – Since the pioneering works of Shim et al.[143] shown in Figure 32, different groups have also developed similar microfluidic tools to probe phase changes: liquid-liquid phase separation (LLPS) and crystallization in aqueous two-phase systems (ATPS),[237,238] possibly in the context of atmospheric and sea spray aerosols.[239–241] Importantly, these works show that the incorporation of a thin membrane is not necessary, as water pervaporation through the entire PDMS matrix of the chip combined with the possible dissolution of water in the oil phase also allows for the slow shrinkage of the stored droplets. Such devices, however, do not allow dynamic control of the droplet shrinkage dynamics and do not allow one to reinflate the droplets, unless the whole chip is placed in a water bath.[237] In this sense, such devices are similar to other work based on two-phase flow microfluidics and exploiting the solubility of water in the continuous oil phase[242,243] (or even evaporation in an air stream[244]) to concentrate by shrinkage the content of stored drops, especially for the preconcentration of analytes. These processes do not match the scope of this review and we will not go further into their details.

Beyond osmosis/pervaporation through dense membranes? – To conclude this section, we are not aware of any microfluidic experimental work that uses membrane-assisted evaporation to shrink/swell confined 2D droplets in the configuration shown in Figure 29B. Many other works, however, exploited microfluidics to control the rate of water evaporation from drops confined in a chip open to the ambient air, again in the context of crystallization of proteins[245,246] and of pharmaceutical compounds in organic solvents.[247] Again, these configurations are slightly outside the scope of this review, so we will not provide an exhaustive list of these works; we refer the reader to the review in ref[117] on crystallization in confinement, including the case of droplets.

Similarly, we are not aware of any work that uses osmosis through nanoporous membranes

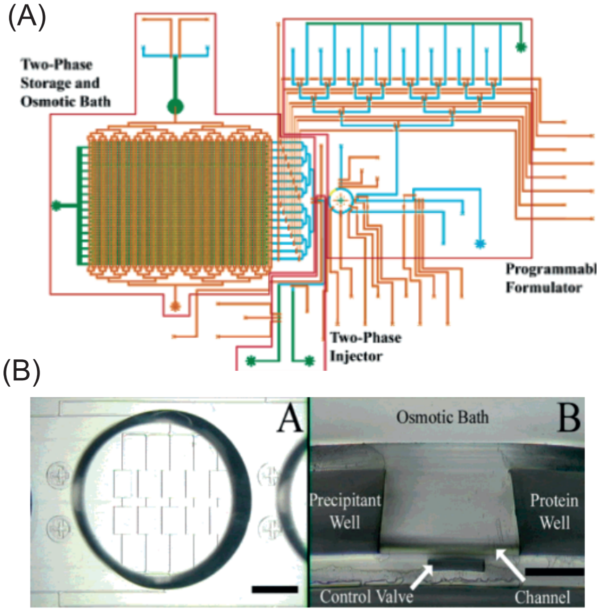

Figure 33: Microfluidic platforms for screening protein crystallization conditions and kinetic optimization of protein crystallization. (A) Arrays of nanoliter droplets stored and solute concentrations in the droplets (as well as their dehydration) controlled by osmosis through a PDMS membrane. Adapted with permission from ref.[226] Copyright 2007 American Chemical Society. (B) Top and cross-sectional views of microfluidic free-interface diffusion coupled with osmosis (or pervaporation) through a thin PDMS membrane. Adapted with permission from ref.[229] Copyright 2006 American Chemical Society.

in the configurations shown in Figure 29, including both 2D droplets and the emptying of dead-end channels. However, such experiments would allow completely new studies, in particular concerning protein solutions or more generally colloidal systems. Indeed, it would be possible to concentrate a protein solution (or a colloidal dispersion) while fixing the chemical potential of molecular species (in particular ionic species) that can cross the membrane. It would then be possible to study the stability of a dispersion at a fixed chemical potential of salts while not also concentrating salts as in Figure 30B or to concentrate proteins while controlling the buffer and salinity.

4.4 Continuous tangential concentration in dead-end geometries

4.4.1 Generalities

We now turn to the geometrical configuration shown in Figure 24B(iii) (see also Figure 34A) corresponding to a dead-end microfluidic geometry supplied by an aqueous solution reservoir. Water transport occurs tangentially along the channel through a fixed interface either by forward osmosis, evaporation, or pervaporation. This net mass transport therefore pumps out the solution from the reservoir and continuously accumulates solutes at the tip of the microfluidic geometry when they are rejected by the interface. Such a configuration is easily achievable for pervaporation in PDMS chips because its gas permeability allows easy filling of dead-end microchannels. As will be discussed later, this configuration also occurs for evaporation in the case of paper-based microfluidic devices connected to a liquid reservoir, and it also resembles pressure-driven ultrafiltration in a dead-end hollow fiber.[159]

4.4.2 Solute accumulation in PDMS dead-end channels

The case of a single dead-end linear channel filled with an aqueous solution is frequently encountered in many microfluidic applications using PDMS soft lithography. As explained in section 3.2.2, water pervaporation along the channel drives a flow from the reservoir with flow rates $Q \simeq L_0 q \simeq 0.2$–$0.7$ nL/min for length $L_0 \simeq 1$ cm. The pervaporation rate per unit length, q (m^2/s), is almost independent of the transverse dimensions of the channel, $h \times w$, as soon as the latter are smaller than the chip thickness; see the 2D picture described by eq 16. To increase the magnitude of these flows, Leng et al. used multilayer soft lithography to integrate a thin PDMS membrane ($\delta \simeq 10$–30 μm) and a channel overlapping the fluid channel with a dry sweep gas as shown in Figure 34B.[135] For such chips, the thin membrane increased the pervaporation flux, and flow rates Q up to a few nL/min were reported for $L_0 \simeq 1$ cm,

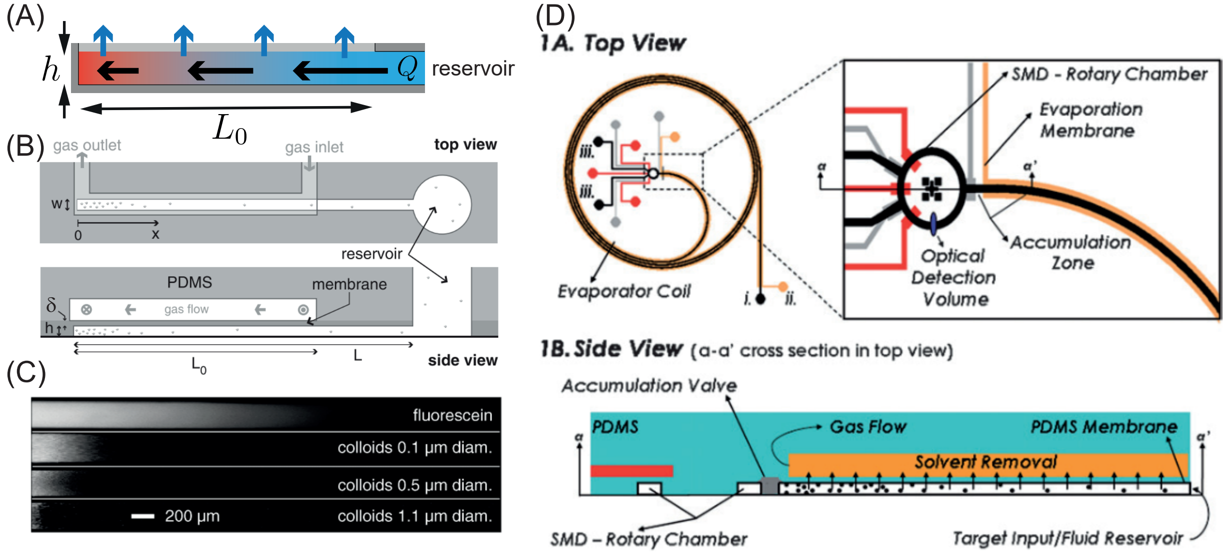

Figure 34: (A) Solute concentration in a dead-end microfluidic geometry. Tangential water transport through the interface (gray) drives a flow within the microfluidic chip, which thus accumulates solutes at the tip (color gradient). (B) Top and side views of a dead-end PDMS chip exploiting pervaporation to concentrate solutes. Typical dimensions: $\delta = 20$ μm, $h = 20$ μm, $w = 100$ μm, and $L_0 = 1$ cm. (C) Fluorescence images showing the solute accumulation zone p at the end of the channel, and highlighting the role of the solute diffusion coefficient D. Adapted with permission from ref.[135] Copyright 2006 American Physical Society. (D) Pervaporation from a long microchannel for high concentration rates (length L_0 up to 2 m in the coil). After sufficient accumulation, the solutes are transferred by diffusion into the circular detection chamber by opening the accumulation valve. Adapted with permission from ref.[248] Copyright 2009 Royal Society of Chemistry.

in agreement with the 1D regime described by eq 18.[135]

As recognized by Verneuil et al.[131] and Randall and Doyle,[132] the pervaporation-induced flow continuously transports any solutes contained in the reservoir up to the tip of the channel where they accumulate. Leng et al. then provided a comprehensive theoretical description of the dynamics of solute concentration induced by pervaporation under dilute solution conditions.[135,249] To summarize, solutes accumulate at the end of the channel in a boundary layer whose extent p depends on the balance between pervaporation-induced advection and molecular diffusion. The size of this accumulation zone scales as $p \propto \sqrt{Dhw/q}$ where D is the solute diffusion coefficient and p typically ranges from a few tens of microns for large colloidal particles ($D \simeq 10^{-13}$ m^2/s) to a few mm for molecular species ($D \simeq 10^{-9}$ m^2/s), as shown in Figure 34C. After a transient, the solute concentration rate at the tip of the channel is finally given by the solute mass balance:

$$phw\frac{\Delta C}{\Delta t} \simeq C_0 L_0 q\,, \tag{26}$$

with C_0 being the solute concentration in the reservoir,[135] and ΔC being the increase in solute concentration during the time interval Δt. Such a description was confirmed by measurements of concentration profiles in microfluidic pervaporation experiments and validated by comparison with numerical resolution of transport equations.[135,249] Equation 26 shows that the concentration rate can be modulated by the geometrical dimensions of the channel ($h \times w \times L_0$), also playing a role on p and q; see eq 17 for a single linear channel.

To obtain high concentration rates $\Delta C/\Delta t$, Puelo and Wang used multilayer soft lithography to make a PDMS microchannel closed at one end by a pneumatically-actuated valve, with a length of up to $L_0 = 2$ m by winding the latter in a loop shape,[248] as shown in

Figure 34D. This channel was also overlapped by a channel with a dry sweep gas to maximize the water transport through the PDMS membrane, and Puelo and Wang demonstrated pervaporation-induced flow rates up to $Q \simeq$ 40 nL/min at room temperature conditions. As discussed in section 3.2.2, it is likely that pervaporation is influenced by channel density due to the large number of turns in the loop shown in Figure 34D. Geometric optimization of the distance between neighboring channels, much larger than the thickness of the PDMS layer following the design rules dictated by Noblin et al.[134] and shown in Figure 14, would likely lead to higher pervaporation rates. These high flow rates Q nevertheless lead to an accumulation of solutes at the tip of the channel at high concentration rates (see eq 26). After sufficient time, the accumulated solutes are then transported by diffusion into a circular nanoliter detection chamber located downstream of the microvalve once it is opened, Figure 34D. An increase in concentration up to 5000 times has been demonstrated using DNA targets, paving the way for detecting rare target biomolecules in the attomolar concentration range.[248]

4.4.3 Screening of phase diagrams

Binary mixtures – The driving force for pervaporation [$\propto (a_w - \mathrm{RH})$] vanishes when the water chemical activity a_w of the concentrated solution exactly balances the imposed relative humidity (RH $\simeq 0$ for a dry sweep gas). Microfluidic pervaporation thus allows one to concentrate solutes to dense or even dry states. As shown in Figure 35A, Leng et al. demonstrated nucleation and growth of crystals in dead-end channels connected to a reservoir of a dilute aqueous potassium chloride solution. Later, similar microfluidic experiments were also performed to explore the phase diagram of surfactant mixtures, from dilute to concentrated self-assembled phases[250,251] as shown in Figure 35B. Combined measurements using birefringence microscopy and *in situ* small-angle X-ray scattering[251] make it possible to probe the succession of self-assembled phases along the surfactant concentration gradient at the channel tip. The possibility of making different channel geometries on the same chip, all connected the same reservoir, as in Figure 35, allows for a screening on the observed phase changes with the solute concentration rate (see eq 26).

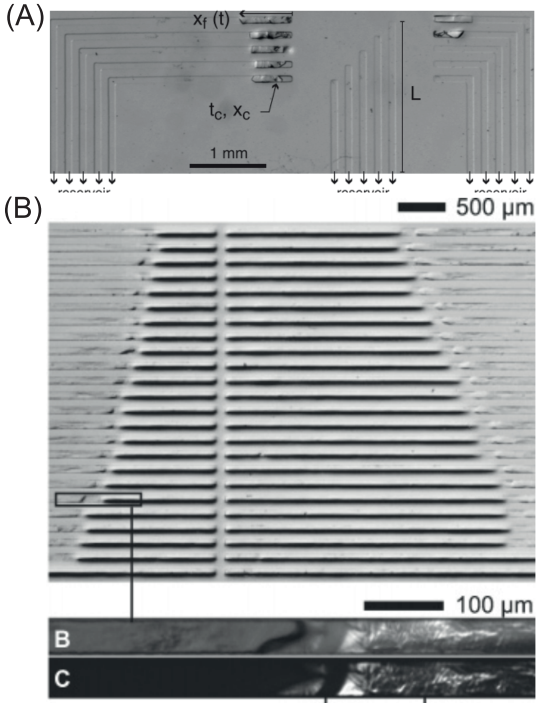

Figure 35: Screening of phase diagrams by pervaporation in PDMS dead-end channels. (A) Crystal growth in channels of different lengths L_0 connected to a reservoir containing a potassium chloride solution. Pervaporation occurs through a thin PDMS membrane above the channels. At this stage, crystals have not yet nucleated in the small channels. Adapted with permission from ref.[135] Copyright 2006 American Physical Society. (B) Forty-eight dead-end channels of different lengths all connected to a reservoir containing a dilute surfactant in water (AOT). Zoomed-in view of the tip of a single channel with bright-field and birefringence microscopy showing a sequence of self-assembled phases. Adapted with permission from ref.[250] Copyright 2007 American Chemical Society.

Schindler and Ajdari provided a comprehensive model based on nonequilibrium thermodynamics to describe the dynamics of the concentration process of a binary mixture (solute+solvent) in such experiments.[252] This model included the dependence of both the water chemical activity a_w and the mutual diffusion coefficient D on the solute concentration C (i.e., the coefficient entering into Fick's law for a binary mixture, also called interdiffusion or collective diffusion coefficient[19,20]) as well as any possible phase transition. This model was used to estimate the mutual diffusion coefficient D (even in concentrated regimes) of aqueous binary solutions[251,253] and colloidal dispersions,[254] from measurements of the solute concentration profiles in microfluidic pervaporation experiments.

Multicomponent mixtures – The theoretical description of the concentration dynamics of multicomponent mixtures is *a priori* a more complex task, preventing the quantitative screening of their phase diagrams using microfluidic pervaporation. This is partly because the size of the accumulation zone $p \propto \sqrt{Dhw/q}$ depends on the nature of the solute through D, as shown in Figure 34C. Moreau et al. demonstrated that it is possible to overcome this problem by connecting the end of the pervaporation channel to a nanoliter-sized storage pool of volume V_p, as shown in Figure 36A, and obtain homogeneous concentration rates inside the pool, regardless of the nature of the solutes. This regime occured when diffusion in the pool was fast enough to homogenize the concentration of the solutes and for $pwh \ll V_p$ to neglect the solute-dependent volume of the accumulation zone upstream of the pool. Such devices were used to quantitatively estimate LLPS in an aqueous polymer/salt solution, starting from dilute homogeneous conditions, as shown in Figure 36B.[255]

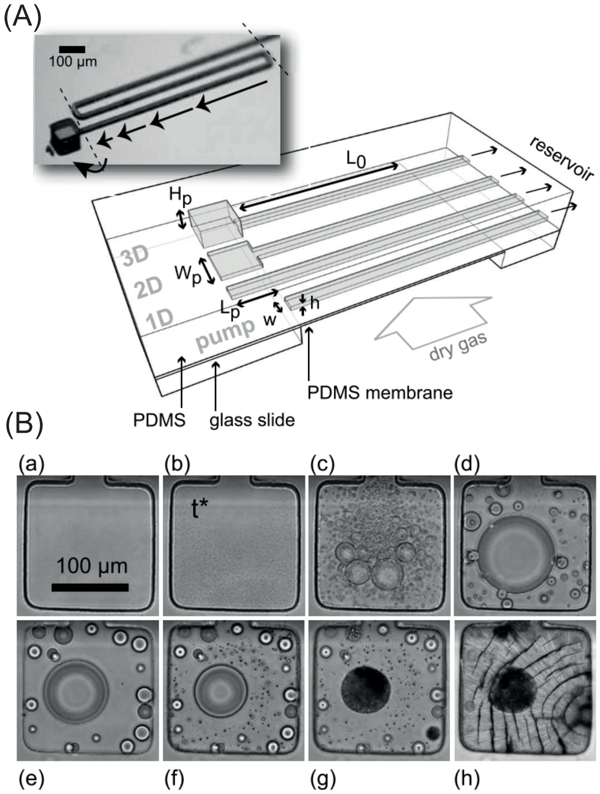

Figure 36: Microfluidic pervaporation to explore multicomponent phase diagrams. (A) Pervaporation of water transports solutes by advection to the pool at the channel end; (inset) SU-8 mold for PDMS casting. (B) Time series of images showing various transitions in an aqueous polymer/salt solution. Adapted with permission from ref.[255] Copyright 2009 American Institute of Physics.

4.4.4 Fabrication of micromaterials

As explained in section 2.2, pervaporation along the channel continuously concentrates solutes at its end, up to possibly dry states, because its driving force [$\propto (a_w - \mathrm{RH})$] only vanishes when the water chemical activity reaches values close to the ambient relative humidity. As recognized by Verneuil et al.[131] and Randall and Dolyle,[132] microfluidic pervaporation therefore can be exploited to shape micromaterials in microfluidic channels from dilute solutions.

Dispersions of hard nanoparticles – As shown in Figure 37, this idea has been used repeatedly with dispersions of hard colloidal particles (radii $\simeq$ 10-500 nm) to form dense, three-dimensional colloidal arrays.[256] The pervaporation-driven flow transports the colloids from the reservoir to the channel tip where they accumulate. The water chemical activity of a dispersion is hardly affected by the presence of the colloids even in concentrated regimes due to the high value of the colloid/water volume ratio. For a dilute dispersion, for example, $a_w \simeq 1 - V_m C = 1 - (V_m/V_c)\varphi \simeq 1$, where $V_c \gg V_m$ is the molar volume of the colloids and φ is the volume fraction of the dispersion. This remains true for concentrated and interacting colloids,[72] and the pervaporation-driven flow concentrates the colloids to form a dense and porous colloidal array through which water can still flow. The growth of the colloidal material therefore does not affect water pervaporation downstream, and the incoming colloid flux remains constant and is given by $C_0Q = C_0L_0q$ for a linear channel of length L_0, with C_0 being the colloid concentration in the reservoir. In this regime, Merlin et al. demonstrated that the growth rate $\dot{x}_d$ (m/s) of the colloidal material is thus given by:

$$hwC_d\dot{x}_d \simeq C_0L_0q\,, \qquad (27)$$

with C_d being its concentration[257] (see Figure 37A and B). Again, the geometrical control of the chip allows one to not only quantitatively predict the growth rate $\dot{x}_d$ of the colloidal material but also adjust it in order to obtain micromaterials in a reasonable time, even from very dilute dispersions ($C_0 \ll C_d$).[256]

Depending on the nature of the colloidal building blocks, in particular their plasmonic properties, such colloidal micromaterials found applications ranging from uniform surface-enhanced Raman spectroscopy (SERS)-active supercrystals,[258–260] microscale electrodes,[261] to metamaterials working in the optical visible range,[262–264] as shown in Figure 37C and D. Similarly, microfluidic pervaporation has also been used to study the hierarchical self-organization of actin in networks of bundles confined in dead-end PDMS microchambers,[265] and to investigate the role of long-range electrostatic repulsions on the solidification and consolidation of charge-stabilized dispersions in a microchannel.[217,254]

Molecular mixtures – For molecular mixtures such as polymer solutions, the water chemical activity a_w can decrease down to 0 with the increase of solute concentration, but microfluidic pervaporation still allows for the fabrication of dense and dry micromaterials with a shape defined by the geometry of the channels. Indeed, solutes are accumulated at the end of the channel by the pervaporation-induced flow, up to forming a dry state (using a dry sweep gas, RH= 0), that locally stops the pervaporation flux across PDMS ($a_w \simeq$ RH). This dry material, however, still invades the channel because it is continuously fed by the incoming solute flux. In this regime, the solute flux is decreased as pervaporation now occurs only on a length $\simeq (L_0 - x_d)$ upstream of the dry material (Figure 37A). In this regime, the solute mass balance gives:

$$hw\varphi_d\dot{x}_d \simeq \varphi_0(L_0 - x_d)q\,, \qquad (28)$$

with φ_0 being the solute volume fraction in the reservoir and φ_d being the solute volume fraction in the dense material given by the balance $a_w(\varphi_d) \simeq$ RH ($\varphi_d \simeq 1$ for RH $= 0$).[256] This exponentially slowed growth, shown in Figure 37B, has been reported multiple times for polymer and surfactant solutions[218,250] as well as for dispersions of small nanoparticles stabilized by a polymer brush.[256,261]

Composite materials with a shape defined by the microfluidic geometry as shown in Figure 38A were fabricated using this technique starting from dilute polymer aqueous solutions[218,266] with applications as polymer microelectromechanical systems.[267] However, the solidification of the solution inside the channel often generates mechanical stresses capable of significantly deforming the microchannel, thus impacting the final shape of the material,[217–219] and limiting the resolution of this technique to approximately 10 μm.[266] To solve this issue, Demko et al. developed a rigid, optically transparent, and solvent-permeable template prepared by solvent casting.[219] With such templates, shown in Figure 38B, pervaporation-induced patterning of polymers and nanoparticles, starting from solutions in organic solvents, has been reported with high spatial resolution (< 1 μm) and high fidelity.

Toward gradient materials – For both colloidal dispersions and polymer solutions, solute mass balances, eqs 27 and 28, allow for quantitatively predicting the growth rate of micromaterials in a given microfluidic perva-

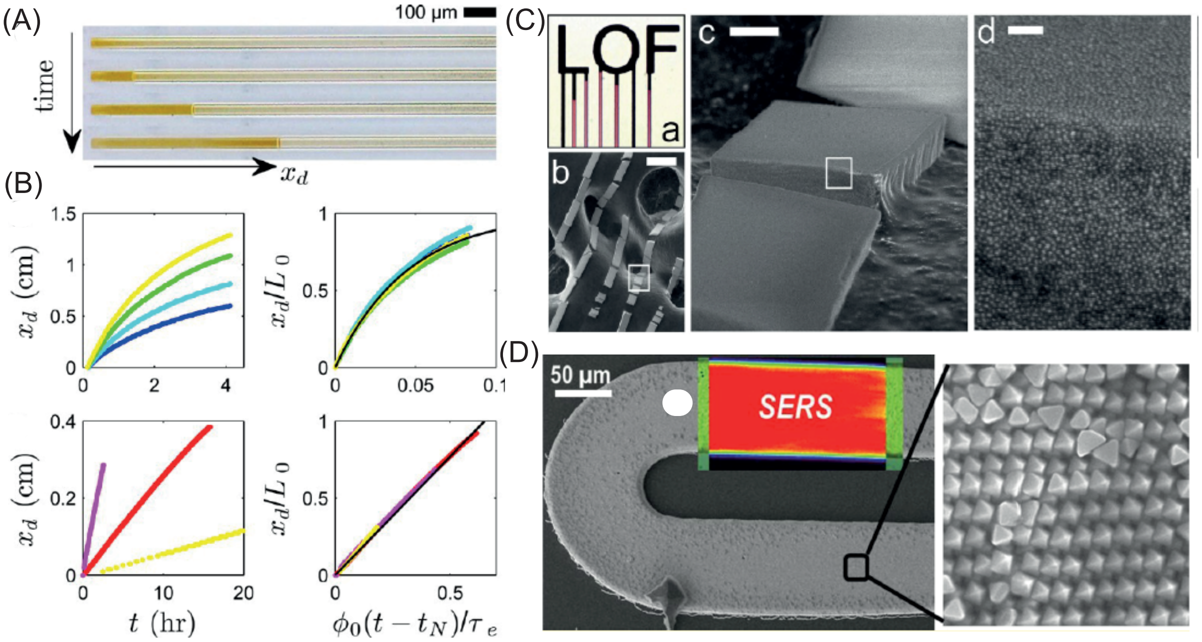

Figure 37: Fabrication of micromaterials by pervaporation. (A) Growth of a dense array of core-shell nanoparticles (silver-silica) by pervaporation in a dead-end PDMS channel. (B) Two growth regimes: (i) exponential slowdown due to the decrease of the pervaporation-driving force and (ii) linear growth when solvent can still flow through the micromaterial. (C) Bright-field (a) and SEM (b-d) images of micromaterials made of gold nanoparticles and obtained by microfluidic pervaporation. In (a) the smallest width of the channels is 20 μm, scale bars of SEM images: 50 (b), 5 (c), and 0.15 μm. Adapted with permission from ref.[256] Copyright 2013 American Chemical Society. (D) SEM image of a SERS-active supercrystal made by gold octahedra. Adapted with permission from ref.[258] Copyright 2015 American Chemical Society.

poration experiment. Laval et al. exploited this control to make microscale materials with programmed composition gradients by combining pneumatically-actuated microvalves and microfluidic pervaporation.[268] As shown in Figure 39A, upstream valves are used to select which solute reservoir is connected to the pervaporation channel and thus which solute enriches the material during its growth. The controlled growth of the material, imparted by the microfluidic pervaporation process, enables one to program spatial composition gradients using appropriate valve actuations; see Figure 39B for an example. For colloidal dispersions, Laval et al. showed programmed composition gradients with spatial modulations down to 50 μm, opening the way for the fabrication of microscale materials with unique properties.

4.4.5 Solute concentration in paper-based microfluidic chips

Beyond pervaporation in dead-end channels, the configuration shown in Figure 34A is also observed in paper-based microfluidic devices but for evaporation. As mentioned in section 3.1, solvent evaporation from paper-based chips cannot be ignored in ambient air, in particular due to the large surface/volume ratio. On the other hand, such devices allow one to easily make passive microfluidic pumps, especially for diagnostic and monitoring applications. As in the pervaporation examples mentioned earlier, paper-based microfluidics should also be able to passively concentrate solutes when connected to a solute reservoir, in a configuration similar to that shown in Figure 34A.

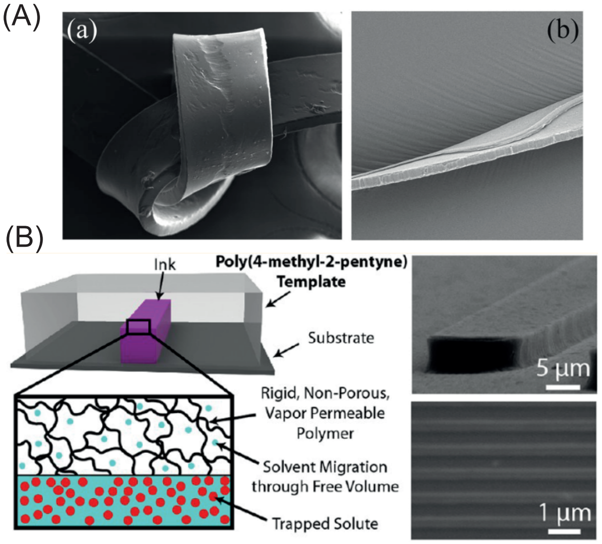

Figure 38: (A) SEM pictures of composite polymer micromaterials made using microfluidic pervaporation. The knot is manually laced from a planar beam (thickness×width = 25×150 μm^2). Reproduced with permission from ref.[218] Copyright 2016 The Royal Society of Chemistry. (B) Highly rigid, chemically robust, optically transparent and vapor-permeable template for pervaporation-induced patterning of polymers and nanoparticles at high resolution, as well as SEM images. Reproduced with permission from ref.[219] Copyright 2012 American Chemical Society.

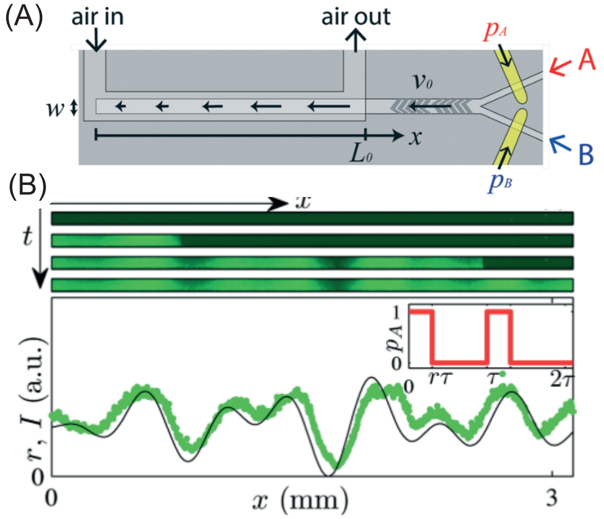

Figure 39: Programmed composition gradients. (A) Schematic top view of pervaporation in a dead-end microchannel fed by two inlets (A and B) addressable by pneumatic microvalves. (B) Snapshots evidencing the growth of a densely-packed bed of colloids from dilute dispersions of fluorescent and nonfluorescent colloids. Temporal modulations of valve actuation (black line) result in controlled spatial modulations of fluorescence along the colloidal micromaterial (green dots). Reproduced with permission from ref.[268] Copyright 2016 Royal Society of Chemistry.

Basic mechanisms – Syms studied this case in detail,[100] and more precisely the configuration shown in Figure 40A of a linear and horizontal paper strip with thickness d connected to an aqueous solution. The paper strip fills with the aqueous solution under the action of capillary forces, and solvent evaporation along the wetted region leads to a flow that is superimposed on the imbibition dynamics. This evaporation-driven flow possibly stops the liquid front at a fixed position H_e smaller than the length of the paper strip. This steady regime occurs when the capillary driving force (capillary pressure P_c) is exactly balanced by the evaporation-induced viscous dissipation in the porous matrix.[100,114,115] The length H_e of the wetted surface in this steady regime is given by:

$$H_e = \sqrt{\frac{2dP_c\kappa}{\eta u_e}}\,, \tag{29}$$

where κ is the permeability (m^2) of the porous layer, η is the viscosity of the liquid, and u_e is the solvent volumetric rate of evaporation per unit area (m/s).[100]

In this regime, evaporation-driven flow along the wetted region continuously pumps the solution in the reservoir, and transports the solutes to the stagnation point. Syms showed, using a 1D model based on mass transport for dilute solutions including solute adsorption on the solid phase,[100] that the dynamics of the solute concentration in the paper strip is exactly the same as that in a PDMS dead-end channel with pervaporation.[135,249] However, a notable difference is that the length H_e of the evaporative pump

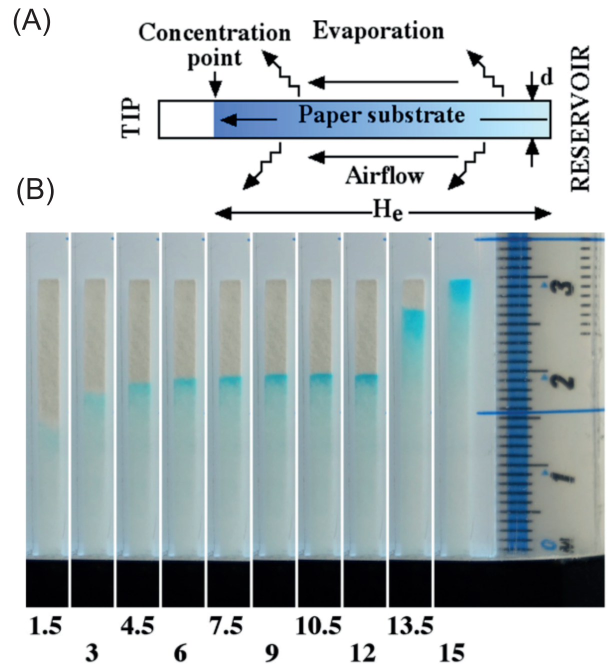

Figure 40: Solute concentration in paper-based microfluidics. (A) Schematic mechanisms for a linear paper strip filled with water on a length H_e and connected to a solute reservoir. Water evaporation from the porous matrix transports the solutes to the stagnation point where they accumulate. (B) Evaporation-driven accumulation of a blue dye at the stagnation point in the paper strip (absolute times in minutes under the snapshots). After 12 min, evaporation is minimized by turning off an air fan that was forcing it before, and the solutes are transported to the end of the strip. Adapted with permission from ref.[100] Copyright 2017 American Institute of Physics.

is related to the evaporation flux u_e through eq 29, unlike in the case of pervaporation for which the length L_0 of the channel is fixed.

Interestingly, modulations of the evaporation conditions, thus impacting the evaporation rate u_e in eq 29, can be used to modulate the length H_e of the wetted region, and thus displace the stagnation point. For example, Figure 40B shows the accumulation of solutes at a stagnation point in a paper strip for a given time, and then their transport to the end of the strip, when evaporation is minimized. With such paper-based microfluidic devices, Syms showed concentration factors up to $\simeq$ 100 in 10 min for molecular dyes, and also demonstrated the possibility to separate solutes as in gel chromatography (in addition to their preconcentration) due to absorption differences on the porous matrix.[100]

Applications – Beyond this detailed description of the dynamics of concentration, Abbas et al.[269] and Yu and White[270] used evaporation in paper-based analytical chips for trace chemical detection. In the example shown in Figure 41, a paper-based chip with a starlike shape was developed as a microfluidic analytical platform for separation, preconcentration, and detection in the subattomolar range.[269] More precisely, the tips of the star allow not only a local increase of the evaporation flux but also a local concentration by evaporation of any solute placed in the liquid phase in the center of the star. As shown in Figure 41, evaporation is even capable of concentrating gold nanorods within the porous paper matrix to the tips. These plasmonic nanostructures are then used as SERS substrates to detect traces of chemicals preconcentrated by the same process at the ends of the star. By pre-exposing the star tips to different polyelectrolytes, Abbas et al. also demonstrated not only evaporation-induced preconcentration of solutes but also separation of complex samples in the different polyelectrolyte-coated fingers.[269]

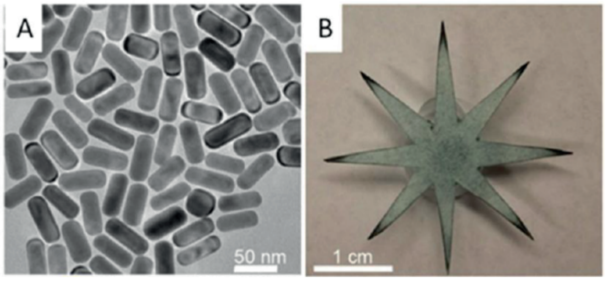

Figure 41: (A) TEM image of the gold nanorods that serve as SERS substrates. (B) Picture of the starlike paper chip evidencing the accumulation of the nanorods at the tips (dark edges). Adapted with permission from ref.[269] Copyright 2013 American Chemical Society.

More recently, Shay et al. developed wearable paper-based microfluidic devices in the context of continuous sweat analysis.[102] Their device is capable of continuously wicking sweatlike fluids over several days thanks to a large custom-designed evaporation zone, as shown in Figure 42A. When analyzing sweat over long periods of time, dissolved salts continuously accumulate at the end of the pad and inevitably precipitate, thus reducing the evaporation surface and the suction pump, as shown in Figure 42B. Shay et al. showed then that both the salt-free evaporative surface and the evaporation-induced flow rate decay exponentially, following similar mechanisms mentioned earlier for pervaporation in dead-end PDMS microfluidic channels; see in particular Figure 35A, Figure 37B, and eq 28. Shay et al. also showed, by connecting the paper device to solutions containing dyes at different concentrations, that the salt deposit retains a quantitative trace of these dyes, paving the way to time-stamped recording of analytes in sweat.[102]

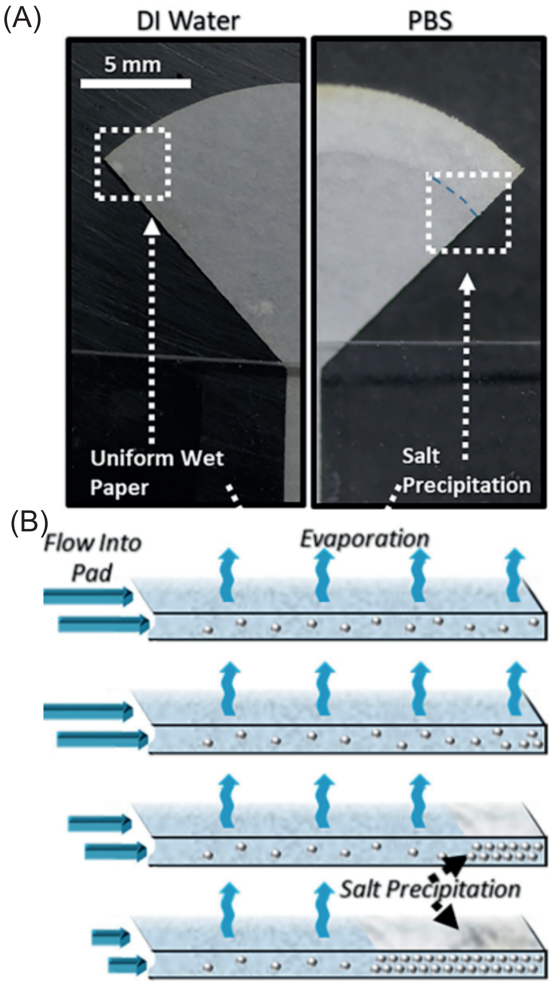

Figure 42: (A) Images of the evaporative pad at the end of the paper-based microfluidic chip connected to a reservoir of deionized water (left) or PBS (right). In the latter case, the continuous accumulation of salt leads to a solid deposit that continuously invades the pad from its edge, following the mechanism schematized in (B). Adapted with permission from ref.[102] Copyright 2020 American Institute of Physics.

4.4.6 Toward continuous solute accumulation with nanoporous membranes

To conclude this section on the configuration shown in Figure 34A, we are not aware of any experiment exploiting such a geometry based on osmosis through nanoporous membranes. Again, we believe it stems from the technical difficulty of inserting nanofiltration or dialysis membranes into microfluidic devices. Such experiments would, however, open many opportunities, in particular the preconcentration of analytes while adding specificity. As mentioned by Puleo and Wang, pervaporation through PDMS (and this remains true for evaporation in paper-based chips) allows one to efficiently preconcentrate the desired analyte but inevitably concentrates any other species also present in solution.[248] The use of nanoporous membranes (especially for ionic species) would allow one to selectively concentrate the targeted macromolecules (e.g., proteins) while maintaining control of the ionic strength and buffer.

The same experiments for the screening of phase diagrams and the fabrication of micromaterials would also allow the concentration of colloidal species and macromolecules while keeping fixed the chemical potential of any other molecular species. It would open the way to the engineering of colloidal micromaterials while controlling stability issues or to innovative studies particularly for soft matter systems, as previously shown in custom-made microfluidic chips without osmosis-induced concentration but with control over the molecular species using dialysis though integrated nanoporous membranes.[271–273]

4.5 Continuous frontal concentration in dead-end geometries

We conclude our panorama of passive microfluidic concentration with the frontal geometry shown in Figure 24B(iv). In this case, passive solvent mass transfer occurs at the tip of a microfluidic channel, and solutes are retained upstream. We are not aware of such a configuration for osmosis or pervaporation, probably because of the technical difficulty of inserting a membrane transversely into the channel to close it, and at any location to facilitate local observations. On the other hand, this configuration is often observed for evaporation from open microchannels, as shown in Figure 43A. This geometrical configuration is the basis for the operation of the micropumps presented in section 3.1.

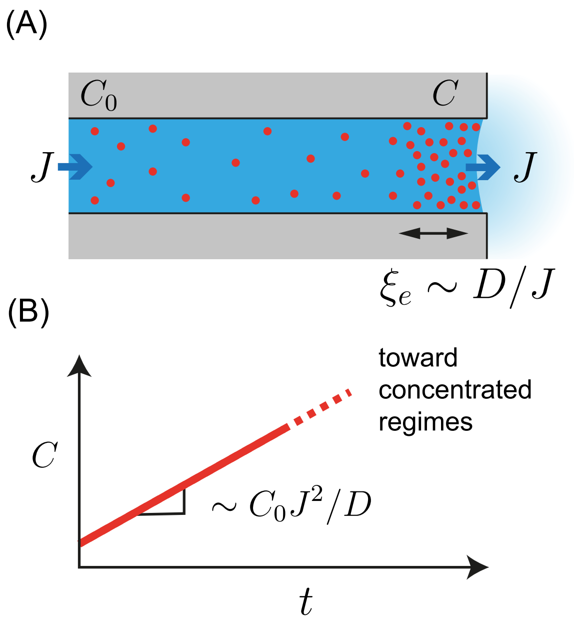

Figure 43: Frontal concentration by evaporation. (A) Evaporation at a rate J from an open microfluidic channel connected to a reservoir of solutes at concentration C_0. Nonvolatile solutes continuously accumulate upstream of the interface in a boundary layer ξ_e. (B) Temporal increase in solute concentration at the channel end from the mass balance eq 31, which is valid for a dilute binary solution.

4.5.1 Basic mechanisms

Water evaporation from the pinned gas/liquid interface continuously pumps the solution within the microchannel, and nonvolatile solutes accumulate upstream of the interface possibly decreasing the water chemical activity at the interface $a_w^\star$ and, thus, the evaporation driving force $\propto (a_w^\star - \mathrm{RH})$. As mentioned in section 3.1, this effect strongly limits the range of use of evaporation-induced micropumps, because many fluids, especially biological ones, contain ionic species in solution that are susceptible to precipitation, blocking evaporation. In contrast, Walker and Beebe suggested early on that these evaporation-induced flows can be advantageously used for sample preconcentration in microfluidic capillary pumps.[88]

To illustrate numerically the relevance of this effect, let us consider the situation shown in Figure 43A for evaporation from a meniscus flush just at the outlet of a cylindrical channel of radius h filled and connected to a dilute aqueous solution for which $a_w \simeq 1$. For diffusion-limited transport in the ambient air of relative humidity RH, the mass transfer coefficient in eq 13 for estimating the magnitude of the evaporation-driven flow rate is $k = 4D_w^{\mathrm{air}}/(\pi h)$ for a flat meniscus.[78] The mean evaporation-induced velocity J (m/s) in the cylindrical channel is thus as follows:

$$J = \frac{4D_w^{\mathrm{air}} c_{\mathrm{sat}}}{\pi \rho_w h}(1 - \mathrm{RH}), \qquad (30)$$

with $J \simeq 20$ μm/s for $h = 15$ μm and $\mathrm{RH} = 0.5$ at $T = 22$°C. Solutes in the channel are transported by this flow, and accumulate upstream of the interface in a boundary layer whose extent ξ_e is given by the balance between evaporation-induced advection and molecular diffusion. For a dilute solution at concentration C_0, the extent of the boundary layer initially follows $\xi_e \propto (Dt)^{1/2}$ and reaches after a transient $\propto D/J^2$ a fixed size given by $\xi_e \propto D/J$ where D is the solute diffusion coefficient.[73,74] With the estimated evaporation-induced flux $J \simeq 20$ μm/s, $\xi_e \propto D/J \simeq 50$ μm for molecular species ($D \simeq 10^{-9}$ m^2/s), and decreases down to 1 μm for macromolecules ($D \leq 10^{-11}$ m^2/s).

At long time scales, the solute mass balance makes it possible to estimate the concentration rate at the tip of the channel driven by evaporation:

$$\xi_e \frac{\Delta C}{\Delta t} \simeq C_0 J \,, \tag{31}$$

see also ref[73,74] for more details including exact formulas. When the density of the solution evolves with C (buoyant solutes), the concentration gradient generates free convection (when it is perpendicular to gravity), possibly impacting the mass transport, and eq 31 is then no longer valid.[74] When solutal free convection can be neglected (see ref[74] for the range of validity of this regime), eq 31 shows that the typical time scale of the dynamics of solute accumulation is $\tau = D/J^2$, and solute concentration at the channel tip increases at long time scales as $C \propto C_0\, t/\tau$ as shown in Figure 43B. For an aqueous sodium chloride solution, the salt diffusion coefficient is $D \simeq 1.5 \times 10^{-9}$ m^2/s, and thus $\tau \simeq 4$ s with the earlier numerical estimate for J. The solute mass balance given by eq 31 shows that the limit of solubility is reached in only a few hours for $C_0 = 5$ mM. For solutions of macromolecules ($D \leq 10^{-11}$ m^2/s), the time scale τ of the concentration process is much smaller, and the accumulation rate at the interface is extremely rapid except for very dilute solutions.

This simplified picture is no longer valid in concentrated regimes, and two limiting cases must be discussed as for microfluidic pervaporation in dead-end channels (section 4.4, Figure 37B): the case of molecular mixtures and that of the dispersion of hard colloidal particles.

4.5.2 Molecular solutions

Phase transition upon accumulation – For molecular mixtures such as solutions of salts, polymers or surfactants, the chemical activity a_w decreases with the solute concentration, and the accumulation of solutes at the interface at concentration $C^\star$ continuously decreases the evaporation driving force $\propto (a_w(C^\star) - \text{RH})$, see eq 7 in section 2.2.2. As mentioned earlier, the evaporation-induced solute accumulation can eventually lead to their crystallization or even to the solidification of the solution. In the context of evaporation in porous media, this leads to efflorescence,[274] i.e., the formation of salt crystals on the surface of a porous medium, and microfluidic tools are key for *in situ* observations of these phenomena; see for instance, refs,[275,276] or ref[277] in the context of saline precipitation hindering carbon capture and storage processes in deep aquifers[277] and also the review in ref[117] on the issue of crystallization in confinement.

The case of amphiphiles/water solutions in the configuration shown in Figure 43A has been recently studied by Roger et al. in the context of water evaporation through mammalian skins.[278,279] In such experiments shown in Figure 44, a microfluidic capillary is connected to a reservoir containing a dilute aqueous solution of amphiphile molecules at concentration C_0. Evaporation in controlled external humidity RH continuously accumulates the solutes at the gas/liquid interface pinned at the outlet of the capillary. At long times, the solute concentration at the interface $C^\star$ asymptotically tends to the concentration C_i corresponding to the balance $a_w(C_i) = \text{RH}$, and there is a build up of a concentration gradient upstream. As for microfluidic pervaporation with similar complex fluids,[250,251] as shown in Figure 35B, evaporation allows a direct reading of the sequence of the self-assembled phases along the gradient, from the dilute concentration C_0 to $C^\star$ at the channel end. Such experiments can also be exploited to extract the mutual diffusion coefficient D of the amphiphiles/water solution, even in the concentrated self-assembled phases,[279] again as for pervaporation in dead-end microchannels with similar systems.[251,253]

Humidity-independent evaporation – Remarkably, Roger et al. also showed that the evaporation-induced flux J in the earlier experiments is almost independent of relative humidity, even over a wide RH range. This feature could furthermore explain the humidity-independent evaporation observed across human stratum corneum.[278] Such a result is due to

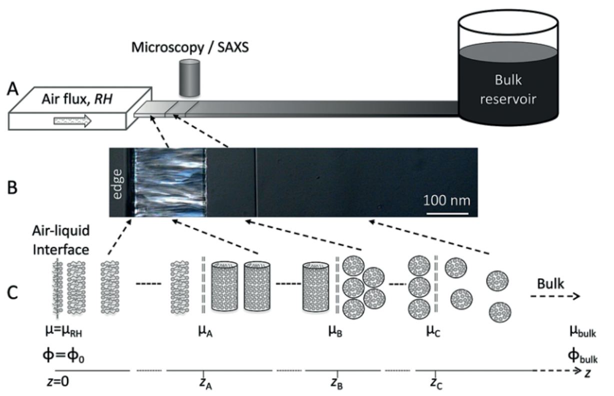

Figure 44: Evaporation-induced concentration of amphiphile molecules in a microcapillary connected to a reservoir. The image obtained using crossed polarizers shows a sequence of self-assembled phases along the concentration gradient (see the corresponding microstructures shown below). Reproduced from ref.[279] Copyright 2018 Royal Society of Chemistry under CC BY 3.0 license.

the presence of a thin layer of a self-assembled phase with low permeability at the channel end.[279] Equivalently, this humidity-insensitive evaporation regime can be explained for any binary mixtures for which both the solvent chemical activity $a_w(C)$ and the mutual diffusion coefficient $D(C)$ decrease strongly at high concentration C.[280]

More precisely, solute concentration at the drying interface $C^\star$ is close, in this regime, to C_i given by $a_w(C_i) = \text{RH}$, and the evaporation-driven flow $J \propto (a_w(C^\star) - \text{RH})$ is thus small. First, variations in RH result in only small changes of C_i due to the abrupt decrease of $a_w(C)$ at high concentration. Furthermore, the sharp decrease of $D(C)$ at high concentration induces a steep concentration gradient at the drying interface, and thus changes in RH affect only a small layer of the concentration profile. These two effects cause the remaining part of the solute concentration profile, which primarily contributes to the evaporation rate J, to be *shielded* from RH variations, and J is thus nearly independent of RH.[279,280]

4.5.3 Colloidal dispersions

Basic mechanisms – For molecular systems, the decay of the evaporation driving force at the interface, $\propto (a_w(C^\star) - \text{RH})$, causes the evaporation-induced flow J to continuously decrease over time, thus preventing the formation of dense materials filling the whole microfluidic channel, unlike in the case of the tangential configuration discussed in section 4.4.

The case of a dispersion of nondeformable colloidal particles is fairly different, as shown in Figure 45 for a dead-end frontal geometry connected to a reservoir of a dilute dispersion. Solvent evaporation from the open end again transports the colloids by advection up to the interface where they accumulate. For these systems, however, the driving force of evaporation $\propto (a_w - \text{RH})$ does not decrease with the accumulation of colloids at the channel end, because the water chemical activity of the dispersion always remains close to that of water, $a_w \simeq 1$. As discussed in section 4.4, this feature is related to the size ratio between the dispersed colloids (diameter $2r \simeq 0.1 - 1$ μm) and the solvent molecules and holds even for concentrated and interacting colloids.[72]

As indicated by eq 31, the scale of the concentration gradient $\xi_e \simeq D/J$ at the channel tip is *a priori* small because of the small diffusion coefficient D of the particles, and evaporation rapidly concentrates the particles up to the formation of a closely-packed array. For nondeformable particles, the accumulated colloids at the channel tip does not block evaporation because water can still flow through the dense but porous assembly. Evaporation of the solvent thus continuously transports the colloids from the reservoir to the colloidal assembly that invades the channel, as shown in Figure 45.

Micromolding in capillaries – As shown in Figure 46A, such features were exploited early on by Kim et al. to obtain crystalline arrays of polymer colloids in PDMS microchannels[281] using the MIMIC technique (MIcro-Molding In Capillaries).[282,283] In this technique, a microstructured PDMS layer is placed in conformal contact with a solid substrate to form

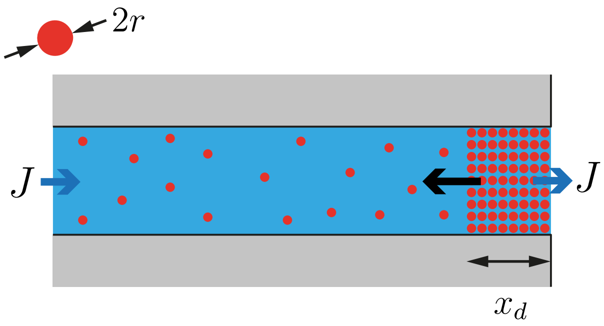

Figure 45: Evaporation-induced growth of a closely-packed array of colloids in a microchannel connected to a reservoir of a dilute dispersion. Solvent evaporation from the outlet transports the colloids by advection at a rate J (m/s) toward the colloidal material that invades the channel at a rate $\dot{x}_d$ (m/s).

a network of microchannels. These channels are then filled by capillary action with either a prepolymer solution or a colloidal dispersion. Solidification inside the mold (e.g., by cross-linking) finally leads to patterned microstructures after the mold is peeled off. In the case of colloidal dispersions, solvent evaporation from the open outlets, as explained schematically in Figure 45, is key for the formation of three-dimensional arrays of microspheres. Although the mechanisms have not been studied in detail in these pioneering works, Kim et al. demonstrated the fabrication of 2D and 3D crystalline colloidal arrays with a shape imparted by the microstructured PDMS stamp, as shown in Figure 46B, starting from a dilute dispersion of polystyrene microspheres.[281]

Similar ideas were exploited later by Zeng and Harrison for producing self-assembled colloidal crystals in PDMS microchannels playing the role of three-dimensional nanofluidic sieves for electrophoretic separation of biomolecules.[284] Ordered colloidal lattices with narrow pore-size distribution were obtained using monodisperse silica particles of different diameters, which allowed optimal protein separation.[285] The same group also demonstrated the fabrication of bidisperse colloidal lattices in PDMS microchannels starting from binary mixtures of polystyrene and silica particles of different diameters, again in the context of on-chip electrophoretic separation of proteins.[286]

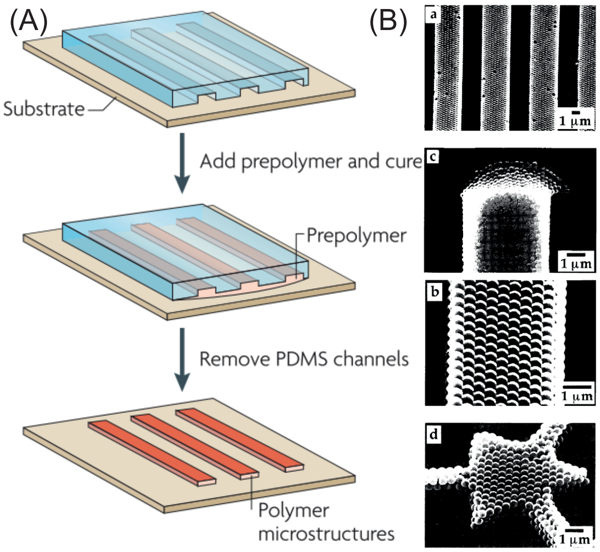

Figure 46: (A) MIMIC technique illustrated here with prepolymers infiltrating a microstructured PDMS stamp (blue) deposited on a solid substrate. Adapted with permission from ref.[283] Copyright 2007 Springer Nature. SEM images of evaporation-induced patterned microstructures obtained using MIMIC and dilute dispersions of microspheres. Adapted with permission from ref.[281] Copyright 1996 John Wiley and Sons.

Colloidal membranes – In these works, capillary action is used to fill the network of channels with a dilute dispersion, and the growth of the colloidal assembly often begins at the outlet of the chip where the air/dispersion interface pins. To make the most of the possibilities offered by microfluidic tools, and particularly the control of geometries, Choi et al. showed that evaporation-induced colloidal assemblies can be fabricated at any location of a PDMS microfluidic chip,[287] using a section of a shallower microchannel (typical heights 5–10 μm) with a specific geometry to play the role of a capillary stop valve as shown in Figure 47.

With this design and dilute colloidal dispersions, Choi et al. demonstrated, using only capillary action, the pinning of the air/dispersion interface at the junction between the shallow and the deep channels and the subsequent

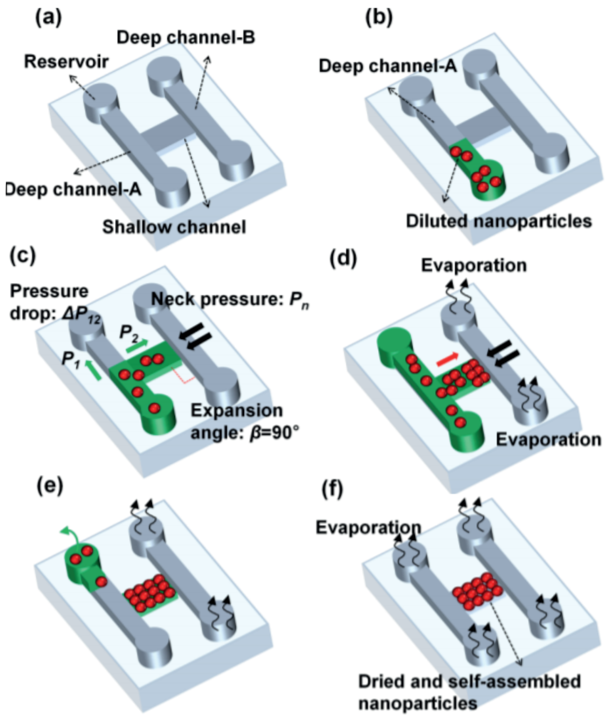

Figure 47: Evaporation-induced assembly of a nanoporous membrane at a specific location in a PDMS microfluidic chip. (a)–(c) Capillary action is used to fill the channels with a dilute dispersion from channel-A, and the air/dispersion interface pins at the junction between the shallow channel and the deep channel-B. (d-f) Evaporation concentrates the colloidal building blocks upstream of the interface, up to the formation of a colloidal membrane with a precise spatial extent. Reproduced with permission from ref.[288] Copyright 2015 Royal Society of Chemistry.

evaporation-driven growth of a porous colloidal array in the shallow portion. These colloidal arrays, whose spatial extent is precisely defined by the geometry of the shallow channels, then act as nanoporous colloidal membranes in the PDMS microchannel. The successive fabrication in the same PDMS chip of multiple colloidal membranes, possibly with different physicochemical functionalities, has opened the way to advanced applications as discussed later.

With standard polystyrene microspheres of micrometer diameter, Choi et al. fabricated $\simeq 300\ \mu$m thick colloidal membranes around a microcompartment in a PDMS chip[287] as shown in Figure 48A. Flows of chemicals in the surrounding channels upstream of the membranes then generate steady gradients inside the central microchamber, allowing for fundamental studies on bacteria chemotaxis with minimized convection.

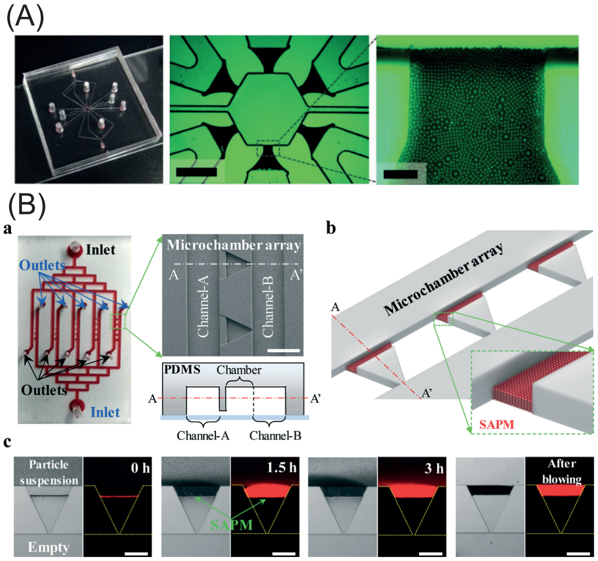

Figure 48: Colloidal membranes. (A) Six nanoporous colloidal membranes surrounding a microcompartment (scale bars: 400 μm and 25 μm) for generating stable gradients in the central chamber using flows of chemicals in the external channels. Adapted with permission from ref.[287] Copyright 2012 Royal Society of Chemistry. (B) Array of triangular chambers with schematic self-assembled particle membranes (SAPMs) (a-b). Build-up of the SAPM in the shallow channels separating channel-A from channel-B (c). Membranes are then used to concentrate cells from channel B by evaporation (air in channel-A), and oil flowing in channel B finally compartmentalizes the triangular chambers for chemostat-like cultivation. Adapted with permission from ref.[289] Copyright 2016 Royal Society of Chemistry.

The same technique with similar colloidal building blocks (polystyrene colloids) has also been used to fabricate self-assembled particle membranes in PDMS chips for studies on bacterial cells in microchambers,[289] as shown in Figure 48B. After fabrication of the colloidal membranes, evaporation downstream of the membrane enhanced by an air stream is used to accumulate bacterial cells upstream. An oil flow then makes it possible to compartmentalize the accumulated cells in a small volume defined by the channels geometry upstream of the membrane; see the triangular chambers in Figure 48B. The colloidal membrane is then used to deliver nutrients to this microfluidic compartment using liquid solutions flowing downstream, as for chemostat-like cultivation in a bioreactor.[289] Arrays of such microfluidic bioreactors (16×4) were also reported recently with the same technique and used for the screening of microbial cells with dynamic programming of cell-culture environments.[290]

These same colloidal membranes have also been used to exploit the properties of their nanoporous interstices as a network of charged nanochannels, the so-called concept of *nanofluidic crystals*.[291] These nanofluidic crystals can then play the role of nanofiltration or ion-exchange membranes. For instance, Syed et al. used evaporation to integrate dense arrays of silica nanoparticles into a PDMS chip thus acting as a cation-selective membrane between two channels, with sub-50 nm junctions.[292] Such colloidal membranes were again fabricated at specific locations of the chip using sections of shallower channels (submicrometer in this case), and capillary trapping of the air/dispersion interface. On-chip electrokinetic preconcentration of biomolecules was then demonstrated with such cation-selective membranes.[292] Similar studies were also reported by Choi et al. with local observations of the ion concentration polarization (ICP) phenomena close to the colloidal membrane using fluorescence microscopy.[293] Using titanium dioxide nanoparticles, Choi et al. also demonstrated the possibility to turn the nature of the colloidal membrane, from cation- to anion-exchange, simply by varying the pH controlling the surface charge of the nanoparticles. In these works, microfluidic tools are key not only to control the location and geometry of the evaporation-driven colloid assembly but also to control the environment and subsequent local analysis of the ionic transport using, for example, fluorescence microscopy.

The same group also reported using the same technique on a reverse electrodialysis (RED) microfluidic platform with a single cation-exchange colloidal membrane separating two PDMS channels,[288] see Figure 49A and ref[294] for a similar concept also based on nanofluidic crystals but fabricated in a micropore through a silicon membrane. Such chips harvest electric energy from the Gibbs free energy associated with the ion concentration gradient across the membrane, the so-called concept of *blue* or *osmotic energy* including both pressure retarded osmosis and RED. To increase the conversion efficiency, Wang et al. then demonstrated a RED nanofluidic platform for energy harvesting, by fabricating alternating stacks of colloidal cation- and anion-exchange membranes in a PDMS chip starting from positively and negatively charged nanoparticles; see Figure 49B.[295]

At large scales, RED offers great potential in terms of energy harvesting, given the abundance of salt and freshwater sources, but remains primarily limited by the low permeability of current ion-exchange membranes.[296] Several works exploiting the most advanced nanofluidic tools have shown how to significantly increase energy conversion using diffusio-osmosis transport through highly charged nanoporous materials; see, e.g., ref.[297] It is possible that the aforementioned techniques for making nanoporous membranes in microfluidic channels starting from tailor-made nanoparticles can be used to screen promising future materials for blue energy harvesting.

To conclude this quick overview of the work on colloidal membranes fabricated by evaporation, Choi et al. also used the same evaporation-based technique to integrate asymmetric colloidal membranes in PDMS chips, ultimately acting as high current ionic diodes.[298] These nonlinear nanofluidic components can also be used for advanced transport of ions and water fluxes in nanoscale channels, and they show promising features to overcome several limitations related to blue energy conversion.[296]

4.5.4 Unidirectional drying

Kinetics of growth – The works cited earlier, from the first demonstration by Kim et al.

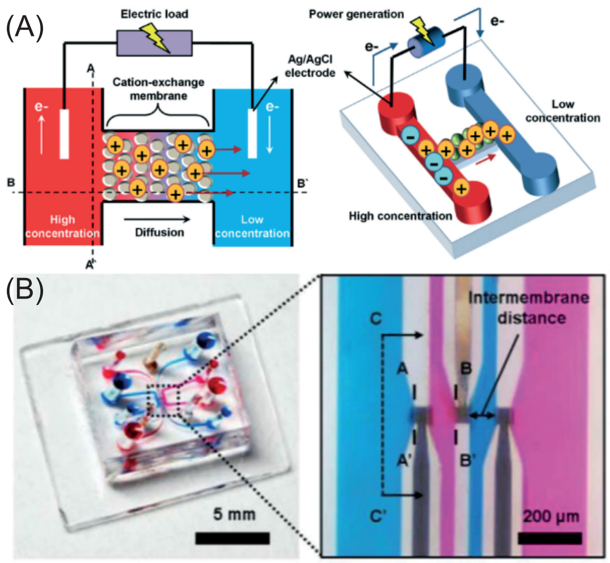

Figure 49: Harvesting energy using colloidal membranes. (A) PDMS chip integrating a cation-exchange nanochannel network membrane separating two parallel channels. This chip is able to harvest electric energy from the salinity gradient across the membrane. Adapted with permission from ref.[288] Copyright 2015 Royal Society of Chemistry. (B) Same technology but with one stack of alternating cation- and anion-exchange nanochannel network membranes fabricated using evaporation-induced assembly. Dyes (blue and pink) allow a better visualization of the fluid channels separated by the colloidal membranes. Adapted with permission from ref.[295] Copyright 2018 Elsevier.

using MIMIC (Figure 46B) to the microfluidic energy harvesting platform developed by Wang et al. (Figure 49A), have primarily focused on the advanced applications offered by the integration of evaporation-induced growth of colloidal micromaterials into microfluidic chips. Many other works, on the other hand, focused on the study of the growth mechanisms of the densely-packed colloidal array. In the simple picture described by Figure 45, often referred to as unidirectional drying, the growth rate of the colloidal micromaterial is *a priori* constant because water can still flow through the interstices of the colloidal material, and the evaporation rate J thus remains constant. The colloid mass balance then indicates the growth rate as follows:

$$C_d \dot{x}_d \simeq C_0 J \,, \tag{32}$$

with C_d being the concentration of the densely-packed colloids. This relation is analogous to eq 27 describing the tangential configuration, except that the evaporation rate J only depends on mass transport in the gas phase upstream of the gas/liquid interface, and thus cannot be geometrically-controlled as for the tangential geometry using pervaporation.

The linear growth predicted by eq 32, $x_d \,\alpha\, t$, was observed only for dispersions of undeformable particles of large diameter (> 100 nm) in experiments using custom-made 1D microfluidic cells or simple capillaries connected to a reservoir (see Figure 44 for a similar setup).[299,300] On the other hand, square root growth, $x_d \,\alpha\, t^{1/2}$, has been reported repeatedly for smaller nanoparticles that are also undeformable.[286,301] This effect has been attributed to the receding of the air/water nanomenisci within the interstices of the dense colloidal array at the channel tip,[302,303] similarly to the drying out of a single capillary discussed in section 3.1 and shown in Figure 5C. As for the case of nanochannels mentioned in section 3.1.7, the decrease of the local partial vapor pressure $p^\star$ in the gas phase due to the strong curvature of the nanomenisci (Kelvin-Laplace equation, eq 12) is also likely to play a role as discussed in ref.[304]

The kinetics of directional drying have also been recently studied for the case of microgel dispersions using the same setup shown in Figure 44.[305] Directional drying concentrates these microgels up to volume fractions higher than the close-packing of hard-spheres due to their ability to deform and interpenetrate. For these highly deformable particles, the mechanisms described in section 4.5.2 for molecular mixtures[279,280] again apply and lead to drying kinetics that are almost independent of the ambient relative humidity, however with the presence of a drying front (at low volume fraction) due to their colloidal nature.

Solidification of colloidal dispersions – Furthermore, the unidirectional drying scenario described by Figure 45 does not include the complexity associated with the solidification of colloidal dispersions, and many groups tested this scenario again using custom-made microfluidic cells or even simple capillaries. These experiments are mainly motivated by fundamental questions concerning the drying of dispersions,[306] particularly of thin colloidal films.[307] Among this wide literature, one can cite fundamental studies on cracks and delamination due to the buildup of tensile stresses during the solidification of the dispersion,[301–303,308–313] or studies on structural anisotropy due to the formation of a colloidal glass before the colloid-close packing.[217,314–316] Other groups also focused on the role of long-range repulsive interactions on mass transport,[254,317,318] or even on solutal free convection due to the presence of horizontal density gradients.[319,320]

Directional drying of colloidal dispersions also often allows one to obtain dense and large arrays with a quasi-perfect crystalline order, which would be difficult to obtain by any other means; see, e.g., Figure 46B. This high degree of ordering can be due to the fact that the flow itself drives the particles toward a denser packing, as shown for weakly Brownian and monodisperse colloids.[321] Colloidal interactions and Brownian motion, however, are also likely to play a role for smaller colloids, as shown recently in a configuration similar to microfluidic directional drying.[322] In any case, a comprehensive understanding of the role of confinement and colloidal interactions (which can also lead to crystalline structures, but in equilibrium) on the degree of ordering of the colloids in the out-of-equilibrium configuration of directional drying is still lacking to this day.

Toward microfluidic screening? – Most of the works mentioned earlier are based on local observations of unidirectional drying of colloidal dispersions in custom-made confined cells or in simple capillaries and thus do not exploit the possibilities offered by the microfabrication tools, especially the simultaneous screening of multiple conditions in networks of channels. Note also that we have not listed closely related works such as drying of colloidal dispersions in confined or sessile drops, see for example refs,[323,324] because the drying interface is no more fixed in these cases, even if the same mechanisms as for unidirectional drying are expected *a priori*. For these reasons, we do not provide a full review of these works, and we believe that the development of dedicated microfluidic chips, allowing in particular for screening different geometries or different evaporation rates on the same chip, would constitute a potential advance in this field. On the other hand, such a technical development must be done with the constraint that these chips would be single use.

5 Conclusion and outlook

In this review, we have provided a comprehensive overview of evaporation, pervaporation and osmosis and their applications in microfluidic devices. As highlighted throughout the text, the unequaled control of transport phenomena and the high surface/volume ratio at the microfluidic scales make it possible to exploit these three processes in the best conditions for applications ranging from passive pumping to solute concentration. One of the goals of this review was to provide a unified and simplistic framework to describe these phenomena, notably solute concentration, using transport equations in 1D geometries. This approach allowed for linking the different applications independently of the process considered, as well as highlighting the importance of the geometry and the physicochemical nature of the solutes, especially molecular solutions versus colloidal dispersions.

In this simplified approach, however, we have not addressed the case of more complex microfluidic geometries, 2D or even 3D, which would require mass transport modeling using specific numerical tools. This would include, for example, flows induced by pervaporation, evaporation, or osmosis in complex channel networks (see for example Figure 15 in the case of pervaporation), or solute accumulation in microfluidic geometries where 3D effects would be non-negligible (e.g., intense tangential flows in the configurations presented in Figure 24B). Beyond this complexity linked to the geometry of microfluidic configurations, which can lead to significant improvements in mass transport, it seems to us that the major problems where advances are expected concern the following: (i) mass transport phenomena in complex fluids and notably their modeling, (ii) the integration of membranes with advanced functionalities into microfluidic devices, and (iii) the bioinspired design of complex passive transport processes, as will be discussed later.

Transport phenomena in complex fluids – As reviewed in section 4, microfluidic evaporation, pervaporation and osmosis have often been exploited beyond applications for fundamental studies on mass transport in complex fluids. However, all the complexity associated with increasing concentration of solutes in a complex fluid up to its solidification has rarely been fully addressed with these microfluidic tools. This is, for instance, the case of multicomponent mixtures where gradients of molecular species,[325] but also of small particles in the case of binary dispersions,[326] can induce diffusio-phoretic transport of large colloidal particles. This interfacially-driven transport can lead to various applications such as membraneless water filtration[327] or removal of particles in dead-end pores.[328] Diffusio-phoresis and diffusio-osmosis undoubtedly play an important role in all the out-of-equilibrium configurations presented in this review when multicomponent mixtures are considered, but these transport phenomena have often been described only for extremely dilute dispersions of large particles in molecular gradients. The microfluidic tools presented throughout section 4, in particular those based on evaporation and pervaporation, could then be cleverly used to study these phenomena but in concentrated complex fluids, a regime for which there is, to our knowledge, no complete theoretical description (role of rheology, coupling with possible phase transitions, etc.). Such knowledge could then be exploited to engineer stratified micromaterials using the microfluidic techniques thoroughly discussed in sections 4.4.4 and 4.5.3, similar to the stratification observed during the drying of polymer/colloid blend films.[329]

Similar issues of advanced transport phenomena also arise in describing the concentration of dispersions of charge-stabilized particles up to their solidification in the microfluidic configurations discussed in section 4. To our knowledge, there is no complete description of the coupled dynamics of colloids/ions in such experiments where electrokinetic effects can occur,[317] as for the nanofluidic crystals[291] mentioned in section 4.5.3. Once again, the microfluidic tools presented in this review could be relevant, especially those integrating nanoporous membranes allowing one to control separately the concentration of colloidal particles from that of ionic species.

The same tools could also prove useful to study the occurrence of mechanical stresses during the solidification of a complex fluid, as mentioned notably in section 4.4.4. For example, the mechanical deformations of the microfluidic chip matrix itself could be used to probe and quantify these mechanical stresses, as demonstrated by Xu et al. in the context of unidirectional drying[311,312] or by Boulogne and Stone for sessile drops deposited on elastomeric sheets.[330] The occurrence of mechanical stresses during 1D drying-induced solidification of a colloidal dispersion has been described theoretically by Style and Peppin by coupling mass transport in the fluid dispersion with linear poroelastic modeling of the colloidal gel that forms during consolidation.[331] However, to our knowledge, there is no complete theoretical description of mass transport allowing one to describe in a continuous way the occurrence of mechanical stresses in the geometries considered in this review for any complex fluid (dispersions, polymer mixtures, etc.), including in particular nonlinear poroelasticity.[332]

Advanced membrane integration – Some of the research avenues mentioned throughout this review are often hampered by the ease of integration of membranes into microfluidic systems. Regarding pervaporation, for example, most of the microfluidic works listed earlier use water permeation through PDMS and therefore do not fully exploit the wide range of membrane materials developed so far,[49] especially for the optimization of the removal of water from organic solvents.[48] The integration of nanoporous membranes with advanced functionalities is another example, and the methods presented in section 4.5.3 based on evaporation-induced fabrication of colloidal membranes have enabled the miniaturization of advanced membrane processes such as energy harvesting by RED.[295] The same colloidal membranes could also be used to screen phase diagrams of complex fluids or to design micromaterials, in a similar way to the methods presented in sections 4.3 and 4.4, but with an additional control on the molecular species because the latter can pass through the nanoporosity of the membrane. In this context, integration of hydrogel-based membranes with controlled nanoporosity[195,198–200] and surface charge density[196,333] could probably help to make similar studies. The nonlinear poroelastic modeling mentioned earlier[332] (see also ref[128]) in the context of the solidification of colloidal dispersions could prove essential for modeling water permeation through possibly highly deformable hydrogel membranes covalently anchored within microfluidic channels.

Further, the recent development of biomimetic membranes integrating either biological channels (e.g., membrane proteins such as aquaporins) or artificial channels (nanotubes, 2D materials, etc.) opens the way to unequaled performances for both permeability and selectivity for numerous applications.[27,50–53] The integration or even fabrication of such membranes within microfluidic devices undoubtedly could considerably improve the processes discussed in this review (e.g., microfluidic osmotic pumping at high rates) but could also open the way to new innovative studies or applications.

Toward bioinspired processes – Throughout this review, we have used the thread of plant physics to illustrate our points about evaporation, pervaporation, and osmosis. These processes have often been considered separately in this review, but it is clear that their coupling on a single microfluidic chip could be relevant. This is notably the case for synthetic trees, for which coupling evaporation and forward osmosis on the same chip could lead to further studies on the possible interplay between evapotranspiration and osmotic transport of sugars in vascular plants.[66,76]

Beyond the physics of plants, the machinery of the living world is another fertile source of inspiration for complex processes. In this context for example, Marbach and Bocquet recently demonstrated using physical arguments that the coupling between osmosis and active membrane transport of ionic species plays a key role in explaining the efficiency of the kidney filtration process.[334] In the living world, osmosis plays a particularly important role: osmotic swelling and bursting of lipid vesicles[335,336] or migration of cells in confined microenvironments,[337] and here again, microfluidic tools have proven essential to probe these phenomena *in situ* and under controlled conditions. In the more specific context of organs-on-chips,[32–34] differences in osmotic pressures can also *a priori* induce osmotic flows across tissue membranes, in configurations sometimes similar to those discussed throughout this review for synthetic membranes (see, e.g., Figure 28B). On the other hand, it is clear that membranes made by tissue engineering present a fascinating complexity (biological functions, deformability, biological development, etc.) that deserves further investigations to go beyond the basic mechanisms discussed in this review. In any case, bioinspired couplings combined with easy integration of advanced membranes, either biomimetic or tissue, into microfluidic systems could probably pave the way for the design of new, efficient, passive mass transport processes.

Author Informations – Biographies

Patrice Bacchin – Patrice Bacchin is a professor at the University of Toulouse (France) since 2008. He works as a researcher at the Laboratoire de Génie Chimique of Toulouse on subjects at the interface between membrane and soft matter sciences. He graduated as a chemical engineer in 1991 and obtained his Ph.D. in

1994 at the Université Paul Sabatier (France). He worked as research officer at the University of Bath in 1995 and for the company Rhône-Poulenc Rorer in 1996 before starting his academic position as associate professor. His current research focuses on the study of the interactions between colloids, biological cells, and membranes that govern physicochemical processes. He develops both experimental and modeling approaches, from microfluidics to process scale, to improve mass transfer efficiency with applications in water treatment, food and pharmaceutical industries, or biomedical processes.

Jacques Leng – Jacques Leng has been working as an academic research scientist (Centre National de la Recherche Scientifique, CNRS) since 2006 at the Laboratory Of the Future (LOF, Pessac, France), a joint team between CNRS, Solvay, and the University of Bordeaux. Previously, he obtained a Ph.D. in chemical-physics at the University of Bordeaux (France) in 1999, and spent 4 years as a research associate at the University of Edinburgh and 2 years as a research engineer for the company Rhodia. He is expert in soft matter and microfluidics with a special focus on functional materials.

Jean-Baptiste Salmon – Jean-Baptiste Salmon obtained his Ph.D. in 2003 at the University of Bordeaux (France) working on the rheology of complex fluids. In 2003, he worked as a postdoctoral researcher (ESPCI, Paris) on reaction-diffusion dynamics in microfluidic channels. Since 2004, he is a CNRS research scientist at LOF (Pessac, France). His current research focuses on mass transport in soft matter systems, including specific microfluidic experiments. In parallel, he uses these same microfluidic tools for applications ranging from protein crystallization to micromaterial engineering as well as to address industrial issues in collaboration with Solvay.

Acknowledgement The authors thank ANR OSMOCHIP (ANR-18-CE06-0021) for funding. This work benefited from meetings within the French working group GDR CNRS 2019 *Solliciter LA Matière Molle* (SLAMM). JBS also thanks O. Vincent for fruitful discussions, especially on evaporation at nanoscale.

References

(1) Whitesides, G. M. The origins and the future of microfluidics. *Nature* **2006**, *442*, 368–373.

(2) Vilkner, T.; Janasek, D.; Manz, A. Micro total analysis systems. Recent developments. *Anal. Chem.* **2004**, *76*, 3373–3385.

(3) Mark, D.; Haeberle, S.; Roth, G.; von Stetten, F.; Zengerle, R. Microfluidic lab-on-a-chip platforms: requirements, characteristics and applications. *Chem. Soc. Rev.* **2010**, *39*, 1153–1182.

(4) Marre, S.; Jensen, K. F. Synthesis of micro and nanostructures in microfluidic systems. *Chem. Soc. Rev.* **2010**, *39*, 1183–1202.

(5) Zhao, C.-X.; Middelberg, A. P. Two-phase microfluidic flows. *Chem. Eng. Sci.* **2011**, *66*, 1394–1411.

(6) Pompano, R. R.; Liu, W.; Du, W.; Ismagilov, R. F. Microfluidics using spatially defined arrays of droplets in one, two, and three dimensions. *Annu. Rev. Anal. Chem.* **2011**, *4*, 59–81.

(7) Nge, P. N.; Rogers, C. I.; Woolley, A. T. Advances in microfluidic materials, functions, integration, and applications. *Chem. Rev.* **2013**, *113*, 2550–2583.

(8) Elvira, K. S.; i Solvas, X. C.; Wootton, R. C. R.; deMello, A. J. The past, present and potential for microfluidic reactor technology in chemical synthesis. *Nat. Chem.* **2013**, *5*, 905–915.

(9) Shang, L.; Cheng, Y.; Zhao, Y. Emerging droplet microfluidics. *Chem. Rev.* **2017**, *117*, 7964–8040.

(10) Convery, N.; Gadegaard, N. 30 years of microfluidics. *Micro. Nano. Eng.* **2019**, *2*, 76–91.

(11) Noviana, E.; Ozer, T.; Carrell, C. S.; Link, J. S.; McMahon, C.; Jang, I.; Henry, C. S. Microfluidic paper-based analytical devices: from design to applications. *Chem. Rev.* **2021**, *121*, 11835–11885.

(12) Stone, H.; Stroock, A.; Ajdari, A. Engineering flows in small devices: microfluidics toward a lab-on-a-chip. *Annu. Rev. Fluid Mech.* **2004**, *36*, 381–411.

(13) Squires, T. M.; Quake, S. R. Microfluidics: fluid physics at the nanoliter scale. *Rev. Mod. Phys.* **2005**, *77*, 977–1026.

(14) Narayanamurthy, V.; Jeroish, Z. E.; Bhuvaneshwari, K. S.; Bayat, P.; Premkumar, R.; Samsuri, F.; Yusoff, M. M. Advances in passively driven microfluidics and lab-on-chip devices: A comprehensive literature review and patent analysis. *RSC Adv.* **2020**, *10*, 11652–11680.

(15) Sten-Knudsen, O. In *Concepts and Models*; Tosteson, D. C., Ed.; Springer Berlin Heidelberg: Berlin, Heidelberg, 1978; pp 5–113.

(16) Velegol, D.; Garg, A.; Guha, R.; Kar, A.; Kumar, M. Origins of concentration gradients for diffusiophoresis. *Soft Matter* **2016**, *12*, 4686–4703.

(17) de Gennes, P.-G.; Brochard-Wyart, F.; Quéré, D. *Capillarity and Wetting Phenomena*; Springer New York: New York, NY, 2004.

(18) Baret, J.-C. Surfactants in droplet-based microfluidics. *Lab Chip* **2012**, *12*, 422–433.

(19) Bird, B. R.; Stewart, E. W.; Lightfoot, E. N. *Transport phenomena*; John Wiley & Sons, New York, 2002.

(20) Cussler, E. L. *Diffusion : Mass Transfer in Fluid Systems*; Cambridge University Press, 1997.

(21) Groot, S. R. D.; Mazur, P. *Non-Equilibrium Thermodynamics*; Dover Publications, 2013.

(22) Peppin, S. S.; Elliott, J. A.; Worster, M. G. Pressure and relative motion in colloidal suspensions. *Phys. Fluids* **2005**, *17*, 053301–053309.

(23) Derjaguin, B.; Dukhin, S.; Koptelova, M. Capillary osmosis through porous partitions and properties of boundary layers of solutions. *J. Colloid Interface Sci.* **1972**, *38*, 584–595.

(24) Anderson, J. L. Colloid transport by interfacial forces. *Ann. Rev. Fluid Mech.* **1989**, *21*, 61–99.

(25) Cath, T.; Childress, A.; Elimelech, M. Forward osmosis: principles, applications, and recent developments. *J. Membr. Sci.* **2006**, *281*, 70–87.

(26) Lee, C.; Cottin-Bizonne, C.; Biance, A. L.; Joseph, P.; Bocquet, L.; Ybert, C. Osmotic flow through fully permeable nanochannels. *Phys. Rev. Lett.* **2014**, *112*, 244501–244505.

(27) Marbach, S.; Bocquet, L. Osmosis, from molecular insights to large-scale applications. *Chem. Soc. Rev.* **2019**, *48*, 3102–3144.

(28) Feng, X.; Huang, R. Y. M. Liquid separation by membrane pervaporation: a review. *Ind. Eng. Chem. Res.* **1997**, *36*, 1048–1066.

(29) Timmer, B. H.; van Delft, K. M.; Olthuis, W.; Bergveld, P.; van den Berg, A. Micro-evaporation electrolyte concentrator. *Sens. Actuators, B* **2003**, *91*, 342–346.

(30) Seemann, R.; Brinkmann, M.; Pfohl, T.; Herminghaus, S. Droplet based microfluidics. *Rep. Prog. Phys.* **2012**, *75*, 016601–016641.

(31) Chen, Z.; Xu, J.; Wang, Y. Gas-liquid-liquid multiphase flow in microfluidic systems - a review. *Chem. Eng. Sci.* **2019**, *202*, 1–14.

(32) Huh, D.; Hamilton, G. A.; Ingber, D. E. From 3D cell culture to organs-on-chips. *Trends Cell Biol.* **2011**, *21*, 745–754.

(33) van der Helm, M. W.; van der Meer, A. D.; Eijkel, J. C. T.; van den Berg, A.; Segerink, L. I. Microfluidic organ-on-chip technology for blood-brain barrier research. *Tissue Barriers* **2016**, *4*, e1142493–13.

(34) Sosa-Hernández, J. E.; Villalba-Rodríguez, A. M.; Romero-Castillo, K. D.; Aguilar-Aguila-Isaías, M. A.; García-Reyes, I. E.; Hernández-Antonio, A.; Ahmed, I.; Sharma, A.; Parra-Saldívar, R.; Iqbal, H. M. N. Organs-on-a-chip module: a review from the development and applications perspective. *Micromachines* **2018**, *9*, 536–555.

(35) Stachowiak, J. C.; Richmond, D. L.; Li, T. H.; Liu, A. P.; Parekh, S. H.; Fletcher, D. A. Unilamellar vesicle formation and encapsulation by microfluidic jetting. *Proc. Natl. Acad. Sci. USA* **2008**, *105*, 4697–4702.

(36) Ota, S.; Yoshizawa, S.; Takeuchi, S. Microfluidic formation of monodisperse, cell-sized, and unilamellar vesicles. *Angew. Chem. Int. Ed.* **2009**, *48*, 6533–6537.

(37) Baker, R. W. *Membrane Technology and Applications*; John Wiley & Sons, Ltd: Chichester, UK, 2012.

(38) Wang, P.-C.; Devoe, D. L.; Lee, C. S. Review integration of polymeric membranes with microfluidic networks for bioanalytical applications. **2001**, *22*, 3857–3867.

(39) de Jong J.,; Lammertink, R. G. H.; Wessling, M. Membranes and microfluidics: a review. *Lab Chip* **2006**, *6*, 1125–1139.

(40) Wijmans, J. G.; Baker, R. W. The solution-diffusion model: a review. *J. Membr. Sci.* **1995**, *107*, 1–21.

(41) Paul, D. Reformulation of the solution-diffusion theory of reverse osmosis. *J. Membr. Sci.* **2004**, *241*, 371–386.

(42) Wang, J.; Dlamini, D. S.; Mishra, A. K.; Pendergast, M. T. M.; Wong, M. C.; Mamba, B. B.; Freger, V.; Verliefde, A. R.; Hoek, E. M. A critical review of transport through osmotic membranes. *J. Membr. Sci.* **2014**, *454*, 516–537.

(43) van Rijn, C. J. M. *Nano and micro engineered membrane technology*; Elsevier, 2004; Vol. Membrane science and technology series.

(44) Lee, K. P.; Arnot, T. C.; Mattia, D. A review of reverse osmosis membrane materials for desalination—Development to date and future potential. *J. Membr. Sci.* **2011**, *370*, 1–22.

(45) Kutowy, O.; Sourirajan, S. Cellulose acetate ultrafiltration membranes. *J. Appl. Polym. Sci.* **1975**, *19*, 1449–1460.

(46) van de Witte, P.; Dijkstra, P. J.; van den Berg, J. W. A.; Feijen, J. Phase separation processes in polymer solutions in relation to membrane formation. *J. Membr. Sci.* **1996**, *117*, 1–31.

(47) Smolders, C. A.; Reuvers, A. J.; Boom, R. M.; Wienk, I. M. Microstructures in phase-inversion membranes. Part 1. Formation of macrovoids. *J. Membr. Sci.* **1992**, *73*, 259–275.

(48) Vane, L. M. Review: membrane materials for the removal of water from industrial solvents by pervaporation and vapor permeation. *J. Chem. Technol. Biotechnol.* **2019**, *94*, 343–365.

(49) Liu, G.; Jin, W. Pervaporation membrane materials: recent trends and perspectives. *J. Membr. Sci.* **2021**, *636*, 119557–119587.

(50) Hélix-Nielsen, C. Biomimetic membranes as a technology platform: challenges and opportunities. *Membranes* **2018**, *8*, 44–59.

(51) Tu, Y.-M.; Song, W.; Ren, T.; Shen, Y.-X.; Chowdhury, R.; Rajapaksha, P.; Culp, T. E.; Samineni, L.; Lang, C.; Thokkadam, A.; et al., Rapid fabrication of precise high-throughput filters from membrane protein nanosheets. *Nat. Mater.* **2020**, *19*, 347–354.

(52) Di Vincenzo, M.; Tiraferri, A.; Musteata, V.-E.; Chisca, S.; Sougrat, R.; Huang, L.-B.; Nunes, S. P.; Barboiu, M. Biomimetic artificial water channel membranes for enhanced desalination. *Nat. Nanotechnol.* **2021**, *16*, 190–196.

(53) Abaie, E.; Xu, L.; Shen, Y.-X. Bioinspired and biomimetic membranes for water purification and chemical separation: a review. *Front. Environ. Sci. Eng.* **2021**, *15*, 124–157.

(54) Duffy, D. C.; McDonald, J. C.; Schueller, O. J.; Whitesides, G. M. Rapid prototyping of microfluidic systems in poly(dimethylsiloxane). *Anal. Chem.* **1998**, *70*, 4974–4984.

(55) Lee, J. N.; Park, C.; Whitesides, G. M. Solvent compatibility of poly(dimethylsiloxane)-based microfluidic devices. *Anal. Chem.* **2003**, *75*, 6544–6554.

(56) Chen, X.; Shen, J.; Hu, Z.; Huo, X. Manufacturing methods and applications of membranes in microfluidics. *Biomed. Microdevices* **2016**, *18*, 104–116.

(57) Chen, X.; Shen, J. Review of membranes in microfluidics. *J. Chem. Technol. Biotechnol.* **2017**, *92*, 271–282.

(58) Bouhid de Aguiar, I.; Schroën, K. Microfluidics used as a tool to understand and optimize membrane filtration processes. *Membranes* **2020**, *10*, 316–335.

(59) Schneider, S.; Gruner, D.; Richter, A.; Loskill, P. Membrane integration into PDMS-free microfluidic platforms for organ-on-chip and analytical chemistry applications. *Lab Chip* **2021**, *21*, 1866–1885.

(60) Duan, C.; Wang, W.; Xie, Q. Review article: fabrication of nanofluidic devices. *Biomicrofluidics* **2013**, *7*, 026501–026541.

(61) Eijkel, J. C. T.; van den Berg, A. Nanofluidics: what is it and what can we expect from it? *Microfluid. Nanofluid.* **2005**, *1*, 249–267.

(62) Sparreboom, W.; van den Berg, A.; Eijkel, J. C. T. Transport in nanofluidic systems: a review of theory and applications. *New J. Phys.* **2010**, *12*, 015004–015026.

(63) Bocquet, L.; Charlaix, E. From microfluidic application to nanofluidic phenomena issue. *Chem. Soc. Rev.* **2010**, *39*, 1073–1095.

(64) Bocquet, L. Nanofluidics coming of age. *Nat. Mater.* **2020**, *19*, 254–256.

(65) Eijkel, J. C.; van den Berg, A. Water in micro- and nanofluidics systems described using the water potential. *Lab Chip* **2005**, *5*, 1202–1209.

(66) Stroock, A. D.; Pagay, V. V.; Zwieniecki, M. A.; Holbrook, N. M. The physicochemical hydrodynamics of vascular plants. *Annu. Rev. Fluid Mech.* **2014**, *46*, 615–642.

(67) Apelblat, A.; Korin, E. The vapour pressures of saturated aqueous solutions of sodium chloride, sodium bromide, sodium nitrate, sodium nitrite, potassium iodate, and rubidium chloride at temperatures from 227 K to 323 K. *J. Chem. Thermodynamics* **1998**, *30*, 59–71.

(68) Kedem, O.; Katchalsky, A. A physical interpretation of the phenomenological coefficients of membrane permeability. *J. Gen. Physiol.* **1961**, *45*, 143–179.

(69) Wexler, A. Vapor pressure formulation for water in range 0 to 100 C. A revision. *J. Res. Natl. Bur. Stand., Sect. A* **1976**, *80A*, 775–785.

(70) Massman, W. J. A review of the molecular diffusivities of H2O, CO2, CH4, CO, O3, SO2, NH3, N2O, NO, and NO2 in air, O2 and N2 near STP. *Atmos. Environ.* **1998**, *32*, 1111–1127.

(71) Bacchin, P.; Si-Hassen, D.; Starov, V.; Clifton, M. J.; Aimar, P. A unifying model for concentration polarization, gel-layer formation and particle deposition in cross-flow membrane filtration of colloidal suspensions. *Chem. Eng. Sci.* **2002**, *57*, 77–91.

(72) Russel, W. B.; Saville, D. A.; Schowalter, W. R. *Colloidal dispersions*; Cambridge University Press, 1989.

(73) Fedorchenko, A.; Chernov, A. Exact solution of the problem of gas segregation in the process of crystallization. *Int. J. Heat Mass Transf.* **2003**, *46*, 915–919.

(74) Salmon, J.-B.; Doumenc, F. Buoyancy-driven dispersion in confined drying of liquid binary mixtures. *Phys. Rev. Fluids* **2020**, *5*, 024201–024219.

(75) Mcelrone, A. J.; Choat, B.; Gambetta, G. A.; Brodersen, C. R. Water uptake and transport in vascular plants. *Nat. Edu. Know.* **2013**, *6*, 6–18.

(76) Jensen, K. H.; Berg-Sørensen, K.; Bruus, H.; Holbrook, N. M.; Liesche, J.; Schulz, A.; Zwieniecki, M. A.; Bohr, T. Sap flow and sugar transport in plants. *Rev. Mod. Phys.* **2016**, *88*, 035007–035069.

(77) Dixon, H. H.; Joly, J. On the ascent of sap. *Philos. Trans. R. Soc. Lond. B* **1896**, *186*, 563–576.

(78) Cazabat, A. M.; Guéna, G. Evaporation of macroscopic sessile droplets. *Soft Matter* **2010**, *6*, 2591–2612.

(79) Lehmann, P.; Assouline, S.; Or, D. Characteristic lengths affecting evaporative drying of porous media. *Phys. Rev. E* **2008**, *77*, 056309–056324.

(80) Chauvet, F.; Duru, P.; Geoffroy, S.; Prat, M. Three periods of drying of a single square capillary tube. *Phys. Rev. Lett.* **2009**, *103*, 124502–124505.

(81) Namasivayam, V.; Handique, K.; Burke, D.; Larson, R. G.; Burns, M. A. A microfabricated valveless pump for delivering non-pulsatile flow. *Proc. SPIE* **2000**, *4177*, 206–214.

(82) Namasivayam, V.; Larson, R. G.; Burke, D. T.; Burns, M. A. Transpiration-based micropump for delivering continuous ultra-low flow rates. *J. Micromech. Microeng.* **2003**, *13*, 261–271.

(83) Goedecke, N.; Eijkel, J.; Manz, A. Evaporation driven pumping for chromatography application. *Lab Chip* **2002**, *2*, 219–223.

(84) Cesaro-Tadic, S.; Dernick, G.; Juncker, D.; Buurman, G.; Kropshofer, H.; Michel, B.; Fattinger, C.; Delamarche, E. High-sensitivity miniaturized immunoassays for tumor necrosis factor α using microfluidic systems. *Lab Chip* **2004**, *4*, 563–569.

(85) Lynn, N. S.; Dandy, D. S. Passive microfluidic pumping using coupled capillary/evaporation effects. *Lab Chip* **2009**, *7*, 3422–3429.

(86) Lynn, N. S.; Henry, C. S.; Dandy, D. S. Evaporation from microreservoirs. *Lab Chip* **2009**, *9*, 1780–1788.

(87) Walker, G. M.; Beebe, D. J. A passive pumping method for microfluidic devices. *Lab Chip* **2002**, *2*, 131–134.

(88) Walker, G. M.; Beebe, D. J. An evaporation-based microfluidic sample concentration method. *Lab Chip* **2002**, *2*, 57–61.

(89) Zimmermann, M.; Bentley, S.; Schmid, H.; Hunziker, P.; Delamarche, E. Continuous flow in open microfluidics using controlled evaporation. *Lab Chip* **2005**, *5*, 1355–1359.

(90) Juncker, D.; Schmid, H.; Drechsler, U.; Wolf, H.; Wolf, M.; Michel, B.; De Rooij, N.; Delamarche, E. Autonomous microfluidic capillary system. *Anal. Chem.* **2002**, *74*, 6139–6144.

(91) Berthier, E.; Warrick, J.; Yu, H.; Beebe, D. J. Managing evaporation for more robust microscale assays: part 1. Volume loss in high throughput assays. *Lab Chip* **2008**, *8*, 852–859.

(92) Berthier, E.; Warrick, J.; Yu, H.; Beebe, D. J. Managing evaporation for more robust microscale assays: part 2. Characterization of convection and diffusion for cell biology. *Lab Chip* **2008**, *8*, 860–864.

(93) Zhang, A.; Zha, Y.; Zhang, J. A surface acoustic wave micropump to pump fluids from a droplet into a closed microchannel using evaporation and capillary effects. *AIP Adv.* **2014**, *4*, 127144–127151.

(94) Xu, Q.; Chen, R.; Wang, H.; Zhu, X.; Liao, Q.; He, X. IR laser induced meniscus evaporation from a microchannel. *Chem. Eng. Sci.* **2015**, *130*, 31–40.

(95) Dollet, B.; Boulogne, F. Natural convection above circular disks of evaporating liquids. *Phys. Rev. Fluids* **2017**, *2*, 053501–053510.

(96) Effenhauser, C. S.; Harttig, H.; Krämer, P. An evaporation-based disposable micropump concept for continuous monitoring applications. *Biomed. Microdevices* **2002**, *4*, 27–32.

(97) Guan, Y. X.; Xu, Z. R.; Dai, J.; Fang, Z. L. The use of a micropump based on capillary and evaporation effects in a microfluidic flow injection chemiluminescence system. *Talanta* **2006**, *68*, 1384–1389.

(98) Xu, Z. R.; Zhong, C. H.; Guan, Y. X.; Chen, X. W.; Wang, J. H.; Fang, Z. L. A microfluidic flow injection system for DNA assay with fluids driven by an on-chip integrated pump based on capillary and evaporation effects. *Lab Chip* **2008**, *8*, 1658–1663.

(99) Chen, K. Y.; Chen, K. E.; Wang, K. A flexible evaporation micropump with precision flow rate control for microfluidic systems. 2012 7th IEEE International Conference on Nano/Micro Engineered and Molecular Systems, NEMS 2012. 2012; pp 653–656.

(100) Syms, R. Rapid evaporation-driven chemical pre-concentration and separation on paper. *Biomicrofluidics* **2017**, *11*, 044116–044132.

(101) Agrawal, P.; Gandhi, P. S.; Majumder, M.; Kumar, P. Insight into the design and fabrication of a leaf-mimicking micropump. *Phys. Rev. Appl.* **2019**, *12*, 031002–031006.

(102) Shay, T.; Saha, T.; Dickey, M. D.; Velev, O. D. Principles of long-term fluids handling in paper-based wearables with capillary-evaporative transport. *Biomicrofluidics* **2020**, *14*, 034112–034123.

(103) Crawford, R.; Murphy, T. E.; Da Silva, A. K.; Berberoglu, H. Experimental characterization of the effects of geometric parameters on evaporative pumping. *Exp. Therm. Fluid Sci.* **2013**, *51*, 183–188.

(104) Zhou, T.; Yang, J.; Zhu, D.; Zheng, J.; Handschuh-Wang, S.; Zhou, X.; Zhang, J.; Liu, Y.; Liu, Z.; He, C.; et al., Hydrophilic sponges for leaf-inspired continuous pumping of liquids. *Adv. Sci.* **2017**, *4*, 1700028–1700033.

(105) Li, J. M.; Liu, C.; Xu, Z.; Zhang, K. P.; Ke, X.; Li, C. Y.; Wang, L. D. A bio-inspired micropump based on stomatal transpiration in plants. *Lab Chip* **2011**, *11*, 2785–2789.

(106) Nie, C.; Frijns, A. J. H.; Mandamparambil, R.; den Toonder, J. M. A microfluidic device based on an evaporation-driven micropump. *Biomed. Microdevices* **2015**, *17*, 47–58.

(107) Borno, R. T.; Steinmeyer, J. D.; Maharbiz, M. M. Charge-pumping in a synthetic leaf for harvesting energy from evaporation-driven flows. *Appl. Phys. Lett.* **2009**, *95*, 013705–013707.

(108) Kim, H.; Kim, K.; Lee, S. J. Compact and thermosensitive nature-inspired micropump. *Sci. Rep.* **2016**, *6*, 36085–36095.

(109) Zhang, Z.; Li, X.; Yin, J.; Xu, Y.; Fei, W.; Xue, M.; Wang, Q.; Zhou, J.; Guo, W. Emerging hydrovoltaic technology. *Nat. Nanotechol.* **2018**, *13*, 1109–1119.

(110) Kokalj, T.; Park, Y.; Vencelj, M.; Jenko, M.; Lee, L. P. Self-powered imbibing microfluidic pump by liquid encapsulation: SIMPLE. *Lab Chip* **2014**, *14*, 4329–4333.

(111) Sotoudegan, M. S.; Mohd, O.; Ligler, F. S.; Walker, G. M. Paper-based passive pumps to generate controllable whole blood flow through microfluidic devices. *Lab Chip* **2019**, *19*, 3787–3795.

(112) Wang, X.; Hagen, J. A.; Papautsky, I. Paper pump for passive and programmable transport. *Biomicrofluidics* **2013**, *7*, 014107–014117.

(113) Mendez, S.; Fenton, E. M.; Gallegos, G. R.; Petsev, D. N.; Sibbett, S. S.; Stone, H. A.; Zhang, Y.; Lopez, G. P. Imbibition in porous membranes of complex shape: quasi-stationary flow in thin rectangular segments. *Langmuir* **2010**, *26*, 1380–1385.

(114) Fries, N.; Odic, K.; Conrath, M.; Dreyer, M. The effect of evaporation on the wicking of liquids into a metallic weave. *J. Colloid Interface Sci.* **2008**, *321*, 118–129.

(115) Liu, Z.; Hu, J.; Zhao, Y.; Qu, Z.; Xu, F. Experimental and numerical studies on liquid wicking into filter papers for paper-based diagnostics. *Appl. Therm. Eng.* **2015**, *88*, 280–287.

(116) Sonner, Z.; Wilder, E.; Heikenfeld, J.; Kasting, G.; Beyette, F.; Swaile, D.; Sherman, F.; Joyce, J.; Hagen, J.; Kelley-Loughnane, N.; et al., The microfluidics of the eccrine sweat gland, including biomarker partitioning, transport, and biosensing implications. *Biomicrofluidics* **2015**, *9*, 031301–031319.

(117) Meldrum, F. C.; O'Shaughnessy, C. Crystallization in confinement. *Adv. Mater.* **2020**, *32*, 2001068–2001131.

(118) Vincent, O.; Szenicer, A.; Stroock, A. D. Capillarity-driven flows at the continuum limit. *Soft Matter* **2016**, *12*, 6656–6661.

(119) Shi, W.; Dalrymple, R. M.; McKenny, C. J.; Morrow, D. S.; Rashed, Z. T.; Surinach, D. A.; Boreyko, J. B. Passive water ascent in a tall, scalable synthetic tree. *Sci. Rep.* **2020**, *10*, 230–238.

(120) Wheeler, T. D.; Stroock, A. D. The transpiration of water at negative pressures in a synthetic tree. *Nature* **2009**, *455*, 208–212.

(121) Vincent, O.; Marmottant, P.; Quinto-Su, P. A.; Ohl, C. D. Birth and growth of cavitation bubbles within water under tension confined in a simple synthetic tree. *Phys. Rev. Lett.* **2012**, *108*, 184502–184506.

(122) Wheeler, T. D.; Stroock, A. D. Stability limit of liquid water in metastable equilibrium with subsaturated vapors. *Langmuir* **2009**, *25*, 7609–7622.

(123) Bruning, M. A.; Ohl, C.-D.; Marin, A. Soft cavitation in colloidal droplets. *Soft Matter* **2021**, *17*, 1861–1872.

(124) Choi, Y. H.; Lee, S. S.; Chung, K. H. Microfluidic actuation and sampling by dehydration of hydrogel. *BioChip J.* **2010**, *4*, 63–69.

(125) Li, J. M.; Liu, C.; Zhang, K. P.; Ke, X.; Xu, Z.; Li, C. Y.; Wang, L. D. A micropump based on water potential difference in plants. *Microfluid. Nanofluid.* **2011**, *11*, 717–724.

(126) Jingmin, L.; Chong, L.; Zheng, X.; Kaiping, Z.; Xue, K.; Liding, W. A microfluidic pump/valve inspired by xylem embolism and transpiration in plants. *PLoS ONE* **2012**, *7*, e50320.

(127) Lee, M.; Lim, H.; Lee, J. Fabrication of artificial leaf to develop fluid pump driven by surface tension and evaporation. *Sci. Rep.* **2017**, *7*, 14735–14742.

(128) Bertrand, T.; Peixinho, J.; Mukhopadhyay, S.; MacMinn, C. W. Dynamics of swelling and drying in a spherical gel. *Phys. Rev. Appl.* **2016**, *6*, 064010–064028.

(129) Shi, W.; Vieitez, J. R.; Berrier, A. S.; Roseveare, M. W.; Surinach, D. A.; Srijanto, B. R.; Collier, C. P.; Boreyko, J. B. Self-stabilizing transpiration in synthetic leaves. *ACS Appl. Mater. Interfaces* **2019**, *11*, 13768–13776.

(130) Eijkel, J. C.; Bomer, J. G.; van den Berg, A. Osmosis and pervaporation in polyimide submicron microfluidic channel structures. *Appl. Phys. Lett.* **2005**, *87*, 114103.

(131) Verneuil, E.; Buguin, A.; Silberzan, P. Permeation-induced flows: consequences for silicone-based microfluidics. *Europhys. Lett.* **2004**, *68*, 412–418.

(132) Randall, G. C.; Doyle, P. S. Permeation-driven flow in poly(dimethylsiloxane) microfluidic devices. *Proc. Natl. Acad. Sci. USA* **2005**, *102*, 10813–10818.

(133) Dollet, B.; Louf, J.-F.; Alonzo, M.; Jensen, K.; Marmottant, P. Drying of channels by evaporation through a permeable medium. *J. R. Soc. Interface* **2019**, *16*, 20180690–20180701.

(134) Noblin, X.; Mahadevan, L.; Coomaraswamy, I. A.; Weitz, D. A.; Holbrook, N. M.; Zwieniecki, M. A. Optimal vein density in artificial and real leaves. *Proc. Natl. Acad. Sci. USA* **2008**, *105*, 9140–9144.

(135) Leng, J.; Lonetti, B.; Tabeling, P.; Joanicot, M.; Ajdari, A. Microevaporators for kinetic exploration of phase diagrams. *Phys. Rev. Lett.* **2006**, *96*, 084503–084506.

(136) Harley, S. J.; Glascoe, E. A.; Maxwell, R. S. Thermodynamic study on dynamic water vapor sorption in sylgard-184. *J. Phys. Chem. B* **2012**, *116*, 14183–14190.

(137) Watson, J. M.; Baron, M. G. Precise static and dynamic permeation measurements using a continuous-flow vacuum cell. *J. Membr. Sci.* **1995**, *106*, 259–268.

(138) Watson, J. M.; Baron, M. G. The behaviour of water in

poly(dimethylsiloxane). *J. Membr. Sci.* **1996**, *110*, 47–57.

(139) Favre, E.; Schaetzel, P.; Nguygen, Q. T.; Clément, R.; Néel, J. Sorption, diffusion and vapour permeation of various penetrants through dense poly(dimethylsiloxane membranes : a transport analysis. *J. Membr. Sci.* **1994**, *92*, 169–184.

(140) Dollet, B.; Chagua Encarnación, K. N.; Gautier, R.; Marmottant, P. Drying by pervaporation in elementary channel networks. *J. Fluid Mech.* **2021**, *A6*, 906–932.

(141) Chagua Encarnación, K. N.; Marmottant, P.; Dollet, B. Pervaporation-induced drying in networks of channels of variable width. *Microfluid. Nanofluid.* **2021**, *25*, 71.

(142) Ziane, N.; Guirardel, M.; Leng, J.; Salmon, J.-B. Drying with no concentration gradient in large microfluidic droplets. *Soft Matter* **2015**, *11*, 3637–3642.

(143) Shim, J.; Cristobal, G.; Link, D. R.; Thorsen, T.; Jia, Y.; Piattelli, K.; Fraden, S. Control and measurement of the phase behavior of aqueous solutions using microfluidics. *J. Am. Chem. Soc.* **2007**, *129*, 8825–8835.

(144) Bell, C. M.; Gerner, F. J.; Strathmann, H. Selection of polymers for pervaporation membranes. *J. Membr. Sci.* **1988**, *36*, 315–329.

(145) Ziemecka, I.; Haut, B.; Scheid, B. Continuous separation, with microfluidics, of the components of a ternary mixture: from vacuum to purge gas pervaporation. *Microfluid. Nanofluid.* **2017**, *21*, 84–96.

(146) Barrie, J. A. In *Diffusion in Polymers*; Crank, J., Park, G. S., Eds.; Academic Press, London and New York, 1968.

(147) Lamberti, A.; Marasso, S. L.; Cocuzza, M. PDMS membranes with tunable gas permeability for microfluidic applications. *RSC Adv.* **2014**, *4*, 61415–61419.

(148) Chang, W. J.; Akin, D.; Sedlak, M.; Ladisch, M. R.; Bashir, R. Poly(dimethylsiloxane) (PDMS) and silicon hybrid biochip for bacterial culture. *Biomed. Microdevices* **2003**, *5*, 281–290.

(149) Markov, D. A.; Lillie, E. M.; Garbett, S. P.; McCawley, L. J. Variation in diffusion of gases through PDMS due to plasma surface treatment and storage conditions. *Biomed. Microdevices* **2014**, *16*, 91–96.

(150) Barrière, B.; Leibler, L. Permeation of a solvent mixture through an elastomeric membrane. The case of pervaporation. *J. Polym. Sci., Part B: Polym. Phys.* **2003**, *41*, 183–193.

(151) Zhang, Q.; Li, H.; Liu, X.; Zhao, W.; Zong, C.; Gai, H. A self-driven miniaturized liquid fuel cell. *Chem. Commun.* **2016**, *52*, 12068–12071.

(152) Wei, J.; Qiu, C.; Tang, C. Y.; Wang, R.; Fane, A. G. Synthesis and characterization of flat-sheet thin film composite forward osmosis membranes. *J. Membr. Sci.* **2011**, *372*, 292–302.

(153) Crestel, E.; Kvasničková, A.; Santanach-Carreras, E.; Bibette, J.; Bremond, N. Motion of oil in water induced by osmosis in a confined system. *Phys. Rev. Fluids* **2020**, *5*, 104003–104021.

(154) Aldousary, S.; Kovscek, A. R. The diffusion of water through oil contributes to spontaneous emulsification during low salinity waterflooding. *J. Pet. Sci. Eng.* **2019**, *179*, 606–614.

(155) Mohammadi, M.; Mahani, H. Direct insights into the pore-scale mechanism of low-salinity waterflooding in carbonates

using a novel calcite microfluidic chip. *Fuel* **2020**, *260*, 116374–116386.

(156) Werber, J. R.; Osuji, C. O.; Elimelech, M. Materials for next-generation desalination and water purification membranes. *Nat. Rev. Mater.* **2016**, *1*, 16018–16033.

(157) Jiao, Y.; Zhao, C.; Kang, Y.; Yang, C. Microfluidics-based fundamental characterization of external concentration polarization in forward osmosis. *Microfluid. Nanofluid.* **2019**, *23*, 36–45.

(158) McCutcheon, J. R.; Elimelech, M. Influence of concentrative and dilutive internal concentration polarization on flux behavior in forward osmosis. *J. Membr. Sci.* **2006**, *284*, 237–247.

(159) Belfort, G.; Davis, R. H.; Zydney, A. L. The behavior of suspensions and macromolecular solutions in crossflow microfiltration. *J. Membr. Sci.* **1994**, *96*, 1–58.

(160) Bacchin, P.; Snisarenko, D.; Stamatialis, D.; Aimar, P.; Causserand, C. Combining fluorescence and permeability measurements in a membrane microfluidic device to study protein sorption mechanisms. *J. Membr. Sci.* **2020**, *614*, 118485–118495.

(161) Bacchin, P.; Aimar, P.; Field, R. W. Critical and sustainable fluxes: theory, experiments and applications. *J. Membr. Sci.* **2006**, *281*, 42–69.

(162) Theeuwes, F.; Yum, S. I. Principles of the design and operation of generic osmotic pumps for the delivery of semisolid or liquid drug formulations. *Ann. Biomed. Eng.* **1976**, *4*, 343–353.

(163) Jannasch, H. W.; Johnson, K. S.; Sakamoto, C. M. Submersible, osmotically pumped analyzer for continuous determination of nitrate in situ. *Anal. Chem.* **1994**, *66*, 3352–3361.

(164) Bruhn, B. R.; Schroeder, T. B.; Li, S.; Billeh, Y. N.; Wang, K. W.; Mayer, M. Osmosis-based pressure generation: dynamics and application. *PLoS ONE* **2014**, *9*, e91350–e91359.

(165) Prasoon, P.; Ramya Devi, D.; Vedha Hari, B. N. Push-pull osmotic tablets - an overview with its commercial significance. *Res. J. Pharm., Biol. Chem. Sci.* **2014**, *5*, 12–25.

(166) Herrlich, S.; Spieth, S.; Messner, S.; Zengerle, R. Osmotic micropumps for drug delivery. *Adv. Drug Delivery Rev.* **2012**, *64*, 1617–1627.

(167) Su, Y. C.; Lin, L.; Pisano, A. P. A water-powered osmotic microactuator. *J. Microelectromech. Syst.* **2002**, *11*, 736–742.

(168) Su, Y. C.; Lin, L. A water-powered micro drug delivery system. *J. Microelectromech. Syst.* **2004**, *13*, 75–82.

(169) Good, B. T.; Bowman, C. N.; Davis, R. H. A water-activated pump for portable microfluidic applications. *J. Colloid Interface Sci.* **2007**, *305*, 239–249.

(170) Chen, Y. C.; Kang, T. H.; Ingram, P. N.; Cheng, Y. H.; Yoon, E. Osmotically actuated micropumps and control valves for point-of-care applications. *J. Microelectromech. Syst.* **2015**, *24*, 982–989.

(171) Peng, P. J.; Su, Y. C. Preprogrammed, rate-switchable osmotic pumping on a chip. *Microfluid. Nanofluid.* **2015**, *18*, 267–277.

(172) Good, B. T.; Bowman, C. N.; Davis, R. H. Modeling and verification of fluid-responsive polymer pumps for microfluidic systems. *Chem. Eng. Sci.* **2004**, *59*, 5967–5974.

(173) Dong, L.; Jiang, H. Autonomous microfluidics with stimuli-responsive hydrogels. *Soft Matter* **2007**, *3*, 1223–1230.

(174) Eddington, D. T.; Beebe, D. J. A valved responsive hydrogel microdispensing device with integrated pressure source. *J. Microelectromech. Syst.* **2004**, *13*, 586–593.

(175) Richter, A.; Klatt, S.; Paschew, G.; Klenke, C. Micropumps operated by swelling and shrinking of temperature-sensitive hydrogels. *Lab Chip* **2009**, *9*, 613–618.

(176) Kwon, G. H.; Jeong, G. S.; Park, J. Y.; Moon, J. H.; Lee, S.-H. A low-energy-consumption electroactive valveless hydrogel micropump for long-term biomedical applications. *Lab Chip* **2011**, *11*, 2910–2915.

(177) Akyazi, T.; Tudor, A.; Diamond, D.; Basabe-Desmonts, L.; Florea, L.; Benito-Lopez, F. Driving flows in microfluidic paper-based analytical devices with a cholinium based poly(ionic liquid) hydrogel. *Sens. Actuators, B* **2018**, *261*, 372–378.

(178) Seo, J.; Wang, C.; Chang, S.; Park, J.; Kim, W. A hydrogel-driven microfluidic suction pump with a high flow rate. *Lab Chip* **2019**, *19*, 1790–1796.

(179) Park, J. Y.; Hwang, C. M.; Lee, S. H.; Lee, S. H. Gradient generation by an osmotic pump and the behavior of human mesenchymal stem cells under the fetal bovine serum concentration gradient. *Lab Chip* **2007**, *7*, 1673–1680.

(180) Park, J. Y.; Kim, S. K.; Woo, D. H.; Lee, E. J.; Kim, J. H.; Lee, S. H. Differentiation of neural progenitor cells in a microfluidic chip-generated cytokine gradient. *Stem Cells* **2009**, *27*, 2646–2654.

(181) Park, J. Y.; Yoo, S. J.; Hwang, C. M.; Lee, S. H. Simultaneous generation of chemical concentration and mechanical shear stress gradients using microfluidic osmotic flow comparable to interstitial flow. *Lab Chip* **2009**, *9*, 2194–2202.

(182) Jun, Y.; Lee, J.; Choi, S.; Yang, J. H.; Sander, M.; Chung, S.; Lee, S.-H. In vivo–mimicking microfluidic perfusion culture of pancreatic islet spheroids. *Sci. Adv.* **2019**, *5*, eaax4520.

(183) Kim, S. H.; Kim, K.; Go, M.; Park, J. Y. Stand-alone external power-free microfluidic fuel cell system harnessing osmotic pump for long-term operation. *J. Micromech. Microeng.* **2018**, *28*, 125005–125014.

(184) Chuang, C. H.; Chiang, Y. Y. Bio-o-pump: a novel portable microfluidic device driven by osmotic pressure. *Sens. Actuators, B* **2019**, *284*, 736–743.

(185) Xu, Z. R.; Yang, C. G.; Liu, C. H.; Zhou, Z.; Fang, J.; Wang, J. H. An osmotic micro-pump integrated on a microfluidic chip for perfusion cell culture. *Talanta* **2010**, *80*, 1088–1093.

(186) Jajack, A.; Stamper, I.; Gomez, E.; Brothers, M.; Begtrup, G.; Heikenfeld, J. Continuous, quantifiable, and simple osmotic preconcentration and sensing within microfluidic devices. *PloS ONE* **2019**, *14*, e0210286–0210301.

(187) Shay, T.; Dickey, M. D.; Velev, O. D. Hydrogel-enabled osmotic pumping for microfluidics: Towards wearable human-device interfaces. *Lab Chip* **2017**, *17*, 710–716.

(188) Knoblauch, M.; Peters, W. S. Münch, morphology, microfluidics - our structural problem with the phloem. *Plant, Cell Environ.* **2010**, *33*, 1439–1452.

(189) Jensen, K. H.; Lee, J.; Bohr, T.; Bruus, H. Osmotically driven flows in microchannels separated by a semipermeable membrane. *Lab Chip* **2009**, *9*, 2093–2099.

(190) Jensen, K. H.; Rio, E.; Hansen, R.; Clanet, C.; Boht, T. Osmotically driven pipe flows and their relation to sugar

transport in plants. *J. Fluid Mech.* **2009**, *636*, 371–396.

(191) Jensen, K. H.; Bohr, T.; Bruus, H. Self-consistent unstirred layers in osmotically driven flows. *J. Fluid Mech.* **2010**, *662*, 197–208.

(192) Haaning, L. S.; Jensen, K. H.; Hélix-Nielsen, C.; Berg-Sorensen, K.; Bohr, T. Efficiency of osmotic pipe flows. *Phys. Rev. E* **2013**, *87*, 053019–53025.

(193) Comtet, J.; Jensen, K. H.; Turgeon, R.; Stroock, A. D.; Hosoi, A. E. Passive phloem loading and long-distance transport in a synthetic tree-on-a-chip. *Nat. Plants* **2017**, *3*, 17032–17039.

(194) Comtet, J. In *Phloem. Methos and Protocols*; Liesche, J., Ed.; Humana, New York, NY., 2019; pp 397–408.

(195) Song, S.; Singh, A. K.; Shepodd, T. J.; Kirby, B. J. Microchip dialysis of proteins using in situ photopatterned nanoporous polymer membranes. *Anal. Chem.* **2004**, *76*, 2367–2373.

(196) Kim, H.; Kim, J.; Kim, E.-G.; Heinz, A. J.; Kwon, S.; Chun, H. Optofluidic in situ maskless lithography of charge selective nanoporous hydrogel for DNA preconcentration. *Biomicrofluidics* **2010**, *4*, 043014–043022.

(197) Davies, R. T.; Kim, J.; Jang, S. C.; Choi, E.-J.; Gho, Y. S.; Park, J. Microfluidic filtration system to isolate extracellular vesicles from blood. *Lab Chip* **2012**, *12*, 5202–5211.

(198) Paustian, J. S.; Azevedo, R. N.; Lundin, S. T. B.; Gilkey, M. J.; Squires, T. M. Microfluidic microdialysis: spatiotemporal control over solution microenvironments using integrated hydrogel membrane microwindows. *Phys. Rev. X* **2013**, *3*, 41010–41022.

(199) Decock, J.; Schlenk, M.; Salmon, J.-B. In situ photo-patterning of pressure-resistant hydrogel membranes with controlled permeabilities in PEGDA microfluidic channels. *Lab Chip* **2018**, *18*, 1075–1083.

(200) Nguyen, H. T.; Massino, M.; Keita, C.; Salmon, J.-B. Microfluidic dialysis using photo-patterned hydrogel membranes in PDMS chips. *Lab Chip* **2020**, *20*, 2383–2393.

(201) Fornells, E. F., E.and Hilder; Breadmore, M. C. Preconcentration by solvent removal: techniques and applications. *Anal. Bioanal. Chem.* **2019**, *411*, 1715–1727.

(202) Lin, C.-C.; Hsu, J.-L.; Lee, G.-B. Sample preconcentration in microfluidic devices. *Microfluid. Nanofluid.* **2011**, *10*, 481–511.

(203) Sharma, N. R.; Lukyanov, A.; Bardell, R. L.; Seifried, L.; Shen, M. Development of an evaporation-based microfluidic sample concentrator. *Proc. SPIE 6886, Microfluidics, BioMEMS, and Medical Microsystems VI* **2008**, 68860R.

(204) Fornells, E.; Barnett, B.; Bailey, M.; Shellie, R. A.; Hilder, E. F.; Breadmore, M. C. Membrane assisted and temperature controlled on-line evaporative concentration for microfluidics. *J. Chromatogr. A* **2017**, *1486*, 110–116.

(205) Zhang, Y.; Kato, S.; Anazawa, T. Vacuum membrane distillation by microchip with temperature gradient. *Lab Chip* **2010**, *10*, 899–908.

(206) Zhang, H.; Tiggelaar, R. M.; Schlautmann, S.; Bart, J.; Gardeniers, H. In-line sample concentration by evaporation through porous hollow fibers and micromachined membranes embedded in microfluidic devices. *Electrophoresis* **2016**, *37*, 463–471.

(207) Albrecht, W.; Hilke, R.; Kneifel, K.; Weigel, T.; Peinemann, K.-V. Selection of microporous hydrophobic membranes for use in gas/liquid contactors: an experimental approach. *J. Membr. Sci.* **2005**, *263*, 66–76.

(208) Choi, J. W.; Hosseini Hashemi, S. M.; Erickson, D.; Psaltis, D. A micropillar array for sample concentration via in-plane evaporation. *Biomicrofluidics* **2014**, *8*, 044108–044116.

(209) Zhang, Y.; Benes, N. E.; Lammertink, R. G. H. Performance study of pervaporation in a microfluidic system for the removal of acetone from water. *Chem. Eng. J.* **2016**, *284*, 1342–1347.

(210) Zizzari, A.; Bianco, M.; Perrone, E.; Manera, M. G.; Cellamare, S.; Ferorelli, S.; Purgatorio, R.; Scilimati, A.; Tolomeo, A.; Dimiccoli, V.; et al., Microfluidic pervaporation of ethanol from radiopharmaceutical formulations. *Chem. Eng. Process.* **2019**, *141*, 107539–107545.

(211) Ziemecka, I.; Haut, B.; Scheid, B. Hydrogen peroxide concentration by pervaporation of a ternary liquid solution in microfluidics. *Lab Chip* **2015**, *15*, 504–511.

(212) Jin, B. J.; Verkman, A. S. Microfluidic platform for rapid measurement of transepithelial water transport. *Lab Chip* **2017**, *17*, 887–895.

(213) Skou, M.; Skou, S.; Jensen, T. G.; Vestergaard, B.; Gillilan, R. E. In situ microfluidic dialysis for biological small-angle X-ray scattering. *J. Appl. Cryst.* **2014**, *47*, 1355–1366.

(214) Zhou, X.; Li, J.; Wu, C.; Zheng, B. Constructing the phase diagram of an aqueous solution of poly(N-isopropyl acrylamide) by controlled microevaporation in a nanoliter microchamber. *Macromol. Rapid Commun.* **2008**, *29*, 1363–1367.

(215) Young, W. R.; Jones, S. Shear dispersion. *Phys. Fluids A* **1991**, *3*, 1087–1101.

(216) Yao, S.; Bethani, A.; Ziane, N.; Brochon, C.; Fleury, G.; Hadziioannou, G.; Poulin, P.; Salmon, J.-B.; Cloutet, E. Synthesis of a conductive copolymer and phase diagram of its suspension with single-walled carbon nanotubes by microfluidic technology. *Macromolecules* **2015**, *48*, 7473–7480.

(217) Ziane, N.; Salmon, J.-B. Solidification of a charged colloidal dispersion investigated using microfluidic pervaporation. *Langmuir* **2015**, *31*, 7943–7952.

(218) Laval, C.; Poulin, P.; Salmon, J.-B. Investigation of the dynamics of growth of polymer materials obtained by combined pervaporation and micro-moulding. *Soft Matter* **2016**, *12*, 1810–1819.

(219) Demko, M. T.; Cheng, J. C.; Pisano, A. P. Rigid, vapor-permeable poly(4-methyl-2-pentyne) templates for high resolution patterning of nanoparticles and polymers. *ACS Nano* **2012**, *6*, 6890–6896.

(220) Zhang, J.; Mahalanabis, M.; Liu, L.; Chang, J.; Pollock, N.; Klapperich, C. A disposable microfluidic virus concentration device based on evaporation and interfacial tension. *Diagnostics* **2013**, *3*, 155–169.

(221) Zhang, J. Y.; Do, J.; Premasiri, W. R.; Ziegler, L. D.; Klapperich, C. M. Rapid point-of-care concentration of bacteria in a disposable microfluidic device using meniscus dragging effect. *Lab Chip* **2010**, *10*, 3265–3270.

(222) Tseng, W. Y.; Van Dam, R. M. Compact microfluidic device for rapid concentration of PET tracers. *Lab Chip* **2014**, *14*, 2293–2302.

(223) Shim, J.; Cristobal, G.; Link, D. R.; Thorsen, T.; Fraden, S. Using microfluidics to decouple nucleation and growth

of protein crystals. *Cryst. Growth Des.* **2007**, *7*, 2192–2194.

(224) Boukellal, H.; Selimović, S.; Jia, Y.; Cristobal, G.; Fraden, S. Simple, robust storage of drops and fluids in a microfluidic device. *Lab Chip* **2009**, *9*, 331–338.

(225) Selimović, S.; Gobeaux, F.; Fraden, S. Mapping and manipulating temperature-concentration phase diagrams using microfluidics. *Lab Chip* **2010**, *10*, 1696–1699.

(226) Lau, B. T.; Baitz, C. A.; Dong, X. P.; Hansen, C. L. A complete microfluidic screening platform for rational protein crystallization. *J. Am. Chem. Soc.* **2007**, *129*, 454–455.

(227) Luo, Y. H.; Li, G.; Chen, Q.; Zhao, J. L. Microfluidic device for automated high-throughput protein crystallization screening by osmotic dewatering. *Chem. Res. Chin. Univ.* **2012**, *33*, 2178–2183.

(228) Morais, S.; Clisson, G.; Mastropietro, T. F.; Briuglia, M. L.; Ter Horst, J. H.; Leng, J.; Salmon, J.-B. An easy to use osmosis-based microfluidic chip for protein crystallization: application to a monoclonal antibody. *Cryst. Growth Des.* **2021**, *21*, 3469–3476.

(229) Hansen, C. L.; Classen, S.; Berger, J. M.; Quake, S. R. A microfluidic device for kinetic optimization of protein crystallization and in situ structure determination. *J. Am. Chem. Soc.* **2006**, *128*, 3142–3143.

(230) Yu, Y.; Wang, X.; Oberthür, D.; Meyer, A.; Perbandt, M.; Duan, L.; Kang, Q. Design and application of a microfluidic device for protein crystallization using an evaporation-based crystallization technique. *J. Appl. Cryst* **2012**, *45*, 53–60.

(231) Lounaci, M.; Rigolet, P.; Abraham, C.; Berre, M. L.; Chen, Y. Microfluidic device for protein crystallization under controlled humidity. *Microelectron. Eng.* **2007**, *84*, 1758–1761.

(232) Longuet, C.; Yamada, A.; Chen, Y.; Baigl, D.; Fattaccioli, J. Spatially-controlled protein crystallization in microfluidic chambers. *J. Cryst. Growth* **2014**, *386*, 179–182.

(233) Yamada, A.; Barbaud, F.; Cinque, L.; Wang, L.; Zeng, Q.; Chen, Y.; Baigl, D. Oil microsealing: a robust micro-compartmentalization method for on-chip chemical and biological assays. *Small* **2010**, *6*, 2169–2175.

(234) Weibel, D. B.; Siegel, A. C.; Lee, A.; George, A. H.; Whitesides, G. M. Pumping fluids in microfluidic systems using the elastic deformation of poly(dimethylsiloxane). *Lab Chip* **2007**, *7*, 1832–1836.

(235) Heo, Y. S.; Cabrera, L. M.; Song, J. W.; Futai, N.; Tung, Y.-C.; Smith, G. D.; Takayama, S. Characterization and resolution of evaporation-mediated osmolality shifts that constrain microfluidic cell culture in poly(dimethylsiloxane) devices. *Anal. Chem.* **2007**, *79*, 1126–1134.

(236) Shim, J. U.; Patil, S. N.; Hodgkinson, J. T.; Bowden, S. D.; Spring, D. R.; Welch, M.; Huck, W. T.; Hollfelder, F.; Abell, C. Controlling the contents of microdroplets by exploiting the permeability of PDMS. *Lab Chip* **2011**, *11*, 1132–1137.

(237) Bleier, B. J.; Anna, S. L.; Walker, L. M. Microfluidic droplet-based tool to determine phase behavior of a fluid system with high composition resolution. *J. Phys. Chem. B* **2018**, *122*, 4067–4076.

(238) Bremer, A.; Mittag, T.; Heymann, M. Microfluidic characterization of macromolecular liquid-liquid phase separation. *Lab Chip* **2020**, *20*, 4225–4234.

(239) Nandy, L.; Dutcher, C. S. Phase behavior of ammonium sulfate with organic acid solutions in aqueous aerosol mimics using microfluidic traps. *J. Phys. Chem. B* **2018**, *122*, 3480–3490.

(240) Nandy, L.; Liu, S.; Gunsbury, C.; Wang, X.; Pendergraft, M. A.; Prather, K. A.; Dutcher, C. S. Multistep phase transitions in sea surface microlayer droplets and aerosol mimics using microfluidic wells. *ACS Earth Space Chem.* **2019**, *3*, 1260–1267.

(241) Roy, P.; Mael, L. E.; Makhnenko, I.; Martz, R.; Grassian, V. H.; Dutcher, C. S. Temperature-dependent phase transitions of aqueous aerosol droplet systems in microfluidic traps. *ACS Earth Space Chem.* **2020**, *4*, 1527–1539.

(242) Chen, H.; Fang, Q.; Yin, X. F.; Fang, Z. L. Microfluidic chip-based liquid-liquid extraction and preconcentration using a subnanoliter-droplet trapping technique. *Lab Chip* **2005**, *5*, 719–725.

(243) Kopp, M. R. G.; Linsenmeier, M.; Hettich, B.; Prantl, S.; Stavrakis, S.; Leroux, J.-C.; Arosio, P. Microfluidic shrinking droplet concentrator for analyte detection and phase separation of protein solutions. *Anal. Chem.* **2020**, *92*, 5803–5812.

(244) i Solvas, X. C.; Turek, V.; Prodromakis, T.; Edel, J. B. Microfluidic evaporator for on-chip sample coneentration. *Lab Chip* **2012**, *12*, 4049–4054.

(245) Talreja, S.; Kim, D. Y.; Mirarefi, A. Y.; Zukoski, C. F.; Kenis, P. J. A. Screening and optimization of protein crystallization conditions through gradual evaporation using a novel crystallization platform. *J. Appl. Cryst.* **2005**, *38*, 988–995.

(246) Goh, L.; Chen, K.; Bhamidi, V.; He, G.; Kee, N. C. S.; Kenis, P. J. A.; Zukoski, C. F.; Braatz, R. D. A stochastic model for nucleation kinetics determination in droplet-based microfluidic systems. *Cryst. Growth Des.* **2010**, *10*, 2515–2521.

(247) Goyal, S.; Thorson, M. R.; Schneider, C. L.; Zhang, G. Z. Z.; Gong, Y.; Kenis, P. J. A microfluidic platform for evaporation-based salt screening of pharmaceutical parent compounds. *Lab Chip* **2013**, *13*, 1708–1723.

(248) Puleo, C. M.; Wang, T. H. Microfluidic means of achieving attomolar detection limits with molecular beacon probes. *Lab Chip* **2009**, *9*, 1065–1072.

(249) Salmon, J.-B.; Leng, J. Application of microevaporators to dynamic exploration of the phase diagram. *J. Appl. Phys.* **2010**, *107*, 084905–084914.

(250) Leng, J.; Joanicot, M.; Ajdari, A. Microfluidic exploration of the phase diagram of a surfactant/water binary system. *Langmuir* **2007**, *23*, 2315–2317.

(251) Daubersies, L.; Leng, J.; Salmon, J.-B. Steady and out-of-equilibrium phase diagram of a complex fluid at the nanolitre scale: combining microevaporation, confocal Raman imaging and small angle X-ray scattering. *Lab Chip* **2013**, *13*, 910–919.

(252) Schindler, M.; Ajdari, A. Modeling phase behavior for quantifying micropervaporation experiments. *Eur. Phys. J E* **2009**, *28*, 27–45.

(253) Bouchaudy, A.; Loussert, C.; Salmon, J.-B. Steady microfluidic measurements of mutual diffusion coefficients of liquid binary mixtures. *AIChE* **2018**, *64*, 358–366.

(254) Merlin, A.; Angly, J.; Daubersies, L.; Madeira, C.; Schöder, S.; Leng, J.; Salmon, J.-B. Time-resolved microfocused small-angle X-ray scattering investigation of the microfluidic concentration

of charged nanoparticles. *Eur. Phys. J. E* **2011**, *34*, 58–64.

(255) Moreau, P.; Dehmoune, J.; Salmon, J.-B.; Leng, J. Microevaporators with accumulators for the screening of phase diagrams of aqueous solutions. *Appl. Phys. Lett.* **2009**, *95*, 033108–033110.

(256) Angly, J.; Iazzolino, A.; Salmon, J.-B.; Leng, J.; Chandran, S.; Ponsinet, V.; Desert, A.; Beulze, A. L.; Mornet, S.; Treguer-Delapierre, M.; et al., Microfluidic-induced growth and shape-up of three-dimensional extended arrays of densely packed nanoparticles. *ACS Nano* **2013**, *7*, 6465–6477.

(257) Merlin, A.; Salmon, J.-B.; Leng, J. Microfluidic-assisted growth of colloidal crystals. *Soft Matter* **2012**, *8*, 3526–3537.

(258) Gómez-Graña, S.; Fernandez-Lopez, C.; Polavarapu, L.; Salmon, J.-B.; Leng, J.; Pastoriza-Santos, I.; Pérez-Juste, J. Gold nanooctahedra with tunable size and microfluidic-induced 3D assembly for highly uniform SERS-active supercrystals. *Chem. Mater* **2015**, *27*, 8310–8317.

(259) García-Lojo, D.; Gómez-Graña, S.; Martín, V.; Solís, D. M.; Taboada, J. M.; Pérez-Juste, J.; Pastoriza-Santos, I. Integrating plasmonic supercrystals in microfluidics for ultrasensitive, label-free, and selective surface-enhanced raman spectroscopy Detection. *ACS Appl. Mater. Interfaces* **2020**, *12*, 46557.

(260) García-Lojo, D.; Modin, E.; Gómez-Graña, S.; Impéror-Clerc, M.; Chuvilin, A.; Pastoriza-Santos, I.; Pérez-Juste, J.; Constantin, D.; Hamon, C. Structure and formation kinetics of millimeter-size single domain supercrystals. *Adv. Funct. Mater.* **2021**, 2101869–2101876.

(261) Demko, M. T.; Cheng, J. C.; Pisano, A. P. High-resolution direct patterning of gold nanoparticles by the microfluidic molding process. *Langmuir* **2010**, *26*, 16710–16714.

(262) Gomez-Grana, S.; Beulze, A. L.; Treguer-Delapierre, M.; Mornet, S.; Duguet, E.; Grana, E.; Cloutet, E.; Hadziioannou, G.; Leng, J.; Salmon, J.-B.; et al., Hierarchical self-assembly of a bulk metamaterial enables isotropic magnetic permeability at optical frequencies. *Mater. Horiz.* **2016**, *3*, 596–601.

(263) Massé, P.; Mornet, S.; Tréguer-Delapierre, M.; Ravaine, S.; Iazzolino, A.; Salmon, J.-B.; Leng, J. Synthesis of size-monodisperse spherical AgSiO2 nanoparticles and 3-D assembly assisted by microfluidics. *Langmuir* **2013**, *29*, 1790–1795.

(264) Baron, A.; Iazzolino, A.; Ehrhardt, K.; Salmon, J.-B.; Aradian, A.; Kravets, V.; Grigorenko, A. N.; Leng, J.; Beulze, A. L.; Tréguer-Delapierre, M.; et al., Bulk optical metamaterials assembled by microfluidic evaporation. *Opt. Mat. Express.* **2013**, *3*, 1792–1797.

(265) Deshpande, S.; Pfohl, T. Hierarchical self-assembly of actin in micro-confinements using microfluidics. *Biomicrofluidics* **2012**, *6*, 034120–034132.

(266) Demko, M. T.; Brackbill, T. P.; Pisano, A. P. Simultaneous patterning of nanoparticles and polymers using an evaporation driven flow in a vapor permeable template. *Langmuir* **2012**, *28*, 9857–9863.

(267) Thuau, D.; Laval, C.; Dufour, I.; Poulin, P.; Ayela, C.; Salmon, J.-B. Engineering polymer MEMS using combined microfluidic pervaporation and micro-molding. *Microsyst. Nanoeng.* **2018**, *4*, 15–22.

(268) Laval, C.; Bouchaudy, A.; Salmon, J.-B. Fabrication of microscale materials with programmable composition gradients. *Lab Chip* **2016**, *16*, 1234–1242.

(269) Abbas, A.; Brimer, A.; Slocik, J. M.; Tian, L.; Naik, R. R.; Singamaneni, S. Multifunctional analytical platform on a paper strip: separation, preconcentration, and subattomolar detection. *Anal. Chem.* **2013**, *85*, 3977–3983.

(270) Yu, W. W.; White, I. M. Inkjet-printed paper-based SERS dipsticks and swabs for trace chemical detection. *Analyst* **2013**, *138*, 1020–1025.

(271) Hesse, H. C.; Beck, R.; Ding, C.; Jones, J. B.; Deek, J.; MacDonald, N. C.; Li, Y.; Safinya, C. R. Direct imaging of aligned neurofilament networks assembled using in situ dialysis in microchannels. *Langmuir* **2008**, *24*, 8398–8401.

(272) Kornreich, M.; Heymann, M.; Fraden, S. Cross polarization compatible dialysis chip. *Lab Chip* **2014**, *14*, 3700–3704.

(273) Balchunas, A. J.; Cabanas, R. A.; Zakhary, M. J.; Gibaud, T.; Fraden, S.; Sharma, P.; Hagan, M. F.; Dogic, Z. Equation of state of colloidal membranes. *Soft Matter* **2019**, *15*, 6791–6802.

(274) Veran-Tissoires, S.; Marcoux, M.; Prat, M. Discrete salt crystallization at the surface of a porous medium. *Phys. Rev. Lett.* **2012**, *108*, 054502–054505.

(275) Naillon, A.; Joseph, P.; Prat, M. Direct observation of pore collapse and tensile stress generation on pore walls due to salt crystallization in a PDMS channel. *Soft Matter* **2019**, *15*, 4562–4569.

(276) Liefferink, R. W.; Naillon, A.; Bonn, D.; Prat, M.; Shahidzadeh, N. Single layer porous media with entrapped minerals for microscale studies of multiphase flow. *Lab Chip* **2018**, *18*, 1094–1104.

(277) Ho, T.-H. M.; Tsai, P. A. Microfluidic salt precipitation: implications for geological CO 2 storage. *Lab Chip* **2020**, *20*, 3806–3814.

(278) Roger, K.; Liebi, M.; Heimdal, J.; Pham, Q.; Spaar, E. Controlling water evaporation through self-assembly. *Proc. Natl. Acad. Sci. USA* **2016**, *113*, 10275–10280.

(279) Roger, K.; Sparr, E.; Wennerström, H. Evaporation, diffusion and self-assembly at drying interfaces. *Phys. Chem. Chem. Phys.* **2018**, *20*, 10430–10438.

(280) Salmon, J.-B.; Doumenc, F.; Guerrier, B. Humidity-insensitive water evaporation from molecular complex fluids. *Phys. Rev. E* **2017**, *96*, 032612–032625.

(281) Kim, E.; Xia, Y.; Whitesides, G. M. Two- and three-dimensional crystallization of polymeric microspheres by micromolding in capillaries. *Adv. Mater.* **1996**, *8*, 245–247.

(282) Kim, E.; Xia, Y.; Whitesides, G. M. Micromolding in capillaries: applications in materials science. *J. Am. Chem. Soc.* **1996**, *118*, 5722–5731.

(283) Weibel, D. B.; DiLuzio, W. R.; Whitesides, G. M. Microfabrication meets microbiology. *Nat. Rev. Microbiol.* **2007**, *5*, 209–218.

(284) Zeng, Y.; Harrison, D. J. Self-assembled colloidal arrays as three-dimensional nanofluidic sieves for separation of biomolecules on microchips. *Anal. Chem.* **2007**, *79*, 2289–2295.

(285) Azim, M.; Malekpourkoupaei, A.; Ye, W.; Jemere, A. B.; Harrison, D. J. Evaluation of protein separation mechanism and pore size distribution in colloidal self-assembled nanoparticle sieves for on-chip protein sizing. *Electrophoresis* **2017**, *38*, 342–349.

(286) Malekpourkoupaei, A.; Kostiuk, L. W.; Harrison, D. J. Fabrication of binary opal lattices in microfluidic devices. *Chem. Mater.* **2013**, *25*, 3808–3815.

(287) Choi, E.; Chang, H. K.; Lim, C. Y.; Kim, T.; Park, J. Concentration gradient generation of multiple chemicals using spatially controlled self-assembly of particles in microchannels. *Lab Chip* **2012**, *12*, 3968–3975.

(288) Choi, E.; Kwon, K.; Kim, D.; Park, J. Tunable reverse electrodialysis microplatform with geometrically controlled self-assembled nanoparticle network. *Lab Chip* **2015**, *15*, 168–178.

(289) Lee, J.; Kim, M.; Park, J.; Kim, T. Self-assembled particle membranes for in situ concentration and chemostat-like cultivation of microorganisms on a chip. *Lab Chip* **2016**, *16*, 1072–1080.

(290) Lee, J.; Park, J.; Kim, T. Dynamic culture and selective extraction of target microbial cells in self-assembled particle membrane-integrated microfluidic bioreactor array. *Anal. Chem.* **2019**, *91*, 6162–6171.

(291) Ouyang, W.; Han, J.; Wang, W. Nanofluidic crystals: nanofluidics in a close-packed nanoparticle array. *Lab Chip* **2017**, *17*, 3006–3025.

(292) Syed, A.; Mangano, L.; Mao, P.; Han, J.; Song, Y. A. Creating sub-50 nm nanofluidic junctions in a PDMS microchip via self-assembly process of colloidal silica beads for electrokinetic concentration of biomolecules. *Lab Chip* **2014**, *14*, 4455–4460.

(293) Choi, E.; Kwon, K.; Kim, D.; Park, J. An electrokinetic study on tunable 3D nanochannel networks constructed by spatially controlled nanoparticle assembly. *Lab Chip* **2015**, *15*, 512–523.

(294) Ouyang, W.; Wang, W.; Zhang, H.; Wu, W.; Li, Z. Nanofluidic crystal: a facile, high-efficiency and high-power-density scaling up scheme for energy harvesting based on nanofluidic reverse electrodialysis. *Nanotechnology* **2013**, *24*, 345401–345409.

(295) Wang, C.; Choi, E.; Park, J. High-voltage nanofluidic energy generator based on ion-concentration-gradients mimicking electric eels. *Nano Energy* **2018**, *43*, 291–299.

(296) Siria, A.; Bocquet, M.-L.; Bocquet, L. New avenues for the large-scale harvesting of blue energy. *Nat. Rev. Chem.* **2017**, *1*, 0091–0099.

(297) Siria, A.; Poncharal, P.; Biance, A.-L.; Fulcrand, R.; Blase, X.; Purcell, S. T.; Bocquet, L. Giant osmotic energy conversion measured in a single transmembrane boron nitride nanotube. *Nature* **2013**, *494*, 455–458.

(298) Choi, E.; Wang, C.; Chang, G. T.; Park, J. High current ionic diode using homogeneously charged asymmetric nanochannel network membrane. *Nano Lett.* **2016**, *16*, 2189–2197.

(299) Inasawa, S.; Oshimi, Y.; Kamiya, H. Formation kinetics of particulate films in directional drying of a colloidal suspension. *Soft Matter* **2016**, *12*, 6851–6857.

(300) Abe, K.; Inasawa, S. A quantitative study of enhanced drying flux from a narrow liquid-air interface of colloidal suspensions during directional drying. *Phys. Chem. Chem. Phys.* **2018**, *20*, 8935–8942.

(301) Dufresne, E. R.; Corwin, E. I.; Greenblatt, N. A.; Ashmore, J.; Wang, D. Y.; Dinsmore, A. D.; Cheng, J. X.; Xie, X.; Hutchinson, J. W.; Weitz, D. A. Flow and fracture in drying nanoparticle suspensions. *Phys. Rev. Lett.* **2003**, *91*, 224501–224504.

(302) Dufresne, E. R.; Stark, D. J.; Greenblatt, N. A.; Cheng, J. X.; Hutchinson, J. W.; Mahadevan, L.; Weitz, D. A. Dynamics of fracture in drying suspensions. *Langmuir* **2006**, *22*, 7144–7147.

(303) Wallenstein, K. J.; Russel, W. B. The theory of delamination during drying of

confined colloidal suspensions. *J. Phys.: Condens. Matter* **2011**, *23*, 194104–194109.

(304) Lidon, P.; Salmon, J.-B. Dynamics of unidirectional drying of colloidal dispersions. *Soft Matter* **2014**, *10*, 4151–4161.

(305) Roger, K.; Crassous, J. J. How the interplay of molecular and colloidal scales controls drying of microgel dispersions. *Proc. Natl. Acad. Sci. USA* **2021**, doi: 10.1073/pnas.2105530118.

(306) Bacchin, P.; Brutin, D.; Davaille, A.; Di Giuseppe, E.; Chen, X. D.; Gergianakis, I.; Giorgiutti-Dauphiné, F.; Goehring, L.; Hallez, Y.; Heyd, R.; et al., Drying colloidal systems: laboratory models for a wide range of applications. *Eur. Phys. J. E* **2018**, *41*, 94–127.

(307) Routh, A. F. Drying of thin colloidal films. *Rep. Prog. Phys.* **2013**, *76*, 046603–046632.

(308) Allain, C.; Limat, L. Regular patterns of cracks formed by directional drying of a collodial suspension. *Phys. Rev. Lett.* **1995**, *74*, 2981–2984.

(309) Gauthier, G.; Lazarus, V.; Pauchard, L. Alternating crack propagation during directional drying. *Langmuir* **2007**, *23*, 4715–4718.

(310) Inasawa, S.; Yamaguchi, Y. Self-organized pattern formation of cracks perpendicular to the drying direction of a colloidal suspension. *Soft Matter* **2012**, *8*, 2416–2422.

(311) Xu, Y.; Engl, W.; Jerison, E. R.; Wallenstein, K. J.; Hyland, C.; Wilen, L. A.; Dufresne, E. R. Imaging in-plane and normal stresses near an interface crack using traction force microscopy. *Proc. Natl. Acad. Sci. USA* **2010**, *107*, 14964–14967.

(312) Xu, Y.; German, G. K.; Mertz, A. F.; Dufresne, E. R. Imaging stress and strain in the fracture of drying colloidal films. *Soft Matter* **2013**, *9*, 3735–3740.

(313) Sarkar, A.; Tirumkudulu, M. S. Delamination of drying nanoparticle suspensions. *Soft Matter* **2011**, *7*, 8816–8822.

(314) Boulogne, F.; Pauchard, L.; Giorgiutti-Dauphiné, F.; Botet, R.; Schweins, R.; Sztucki, M.; Li, J.; Cabane, B.; Goehring, L. Structural anisotropy of directionally dried colloids. *Europhys. Lett.* **2014**, *105*, 38005–38010.

(315) Kiatkirakajorn, P.; Goehring, L. Formation of shear bands in drying colloidal dispersions. *Phys. Rev. Lett.* **2015**, *115*, 088302–088306.

(316) Yang, B.; Smith, N. D.; Johannes, A.; Burghammer, M.; Smith, M. Shear bands and the evolving microstructure in a drying colloidal film studied with scanning µ-SAXS. *Sci. Rep.* **2018**, *8*, 12979–12987.

(317) Sarkar, A.; Tirumkudulu, M. S. Consolidation of charged colloids during drying. *Langmuir* **2009**, *25*, 4945–4953.

(318) Goehring, L.; Li, J.; Kiatkirakajorn, P.-C. Drying paint: from micro-scale dynamics to mechanical instabilities. *Phil. Trans. R. Soc. A* **2017**, *375*, 20160161–20160183.

(319) Inoue, K.; Inasawa, S. Drying-induced back flow of colloidal suspensions confined in thin unidirectional drying cells. *RSC Adv.* **2020**, *10*, 15763–15768.

(320) Pradhan, T. K.; Panigrahi, P. K. Evaporation-induced natural convection of a liquid slug of binary mixture inside a microchannel: effect of confinement. *Microfluid. Nanofluid.* **2016**, *20*, 115–128.

(321) Noirjean, C.; Marcellini, M.; Deville, S.; Kodger, T. E.; Monteux, C. Dynamics and ordering of weakly Brownian particles in directional drying. *Phys. Rev. Mater.* **2017**, *1*, 065601–065610.

(322) Mokrane, M. L.; Desclaux, T.; Morris, J. F.; Joseph, P.; Liot, O. Microstructure of the near-wall layer of filtration-induced colloidal assembly. *Soft Matter* **2020**, *16*, 9726–9737.

(323) Giorgiutti-Dauphiné, F.; Pauchard, L. Drying drops containing solutes: from hydrodynamical to mechanical instabilities. *Eur. Phys. J. E* **2018**, *41*, 32–46.

(324) Bouchaudy, A.; Salmon, J.-B. Drying-induced stresses before solidification in colloidal dispersions:: in situ measurements. *Soft Matter* **2019**, *15*, 2768–2781.

(325) Abécassis, B.; Cottin-Bizonne, C.; Ybert, C.; Ajdari, A.; Bocquet, L. Boosting migration of large particles by solute contrasts. *Nat. Mater.* **2008**, *7*, 785–789.

(326) Sear, R. P.; Warren, P. B. Diffusiophoresis in nonadsorbing polymer solutions: the Asakura-Oosawa model and stratification in drying films. *Phys. Rev. E* **2017**, *96*, 062602–062612.

(327) Shin, S.; Shardt, O.; Warren, P. B.; Stone, H. A. Membraneless water filtration using CO2. *Nat. Commun.* **2017**, *8*, 15181–15186.

(328) Shin, S.; Warren, P. B.; Stone, H. A. Cleaning by surfactant gradients: particulate removal from porous materials and the significance of rinsing in laundry detergency. *Phys. Rev. Appl.* **2018**, *9*, 034012–034017.

(329) Schulz, M.; Smith, R. W.; Sear, R. P.; Brinkhuis, R.; Keddie, J. L. Diffusiophoresis-driven stratification of polymers in colloidal films. *ACS Macro Lett.* **2020**, *9*, 1286–1291.

(330) Boulogne, F.; Stone, H. A. Self-crumpling elastomers: bending induced by the drying stimulus of a nanoparticle suspension. *Europhys. Lett.* **2014**, *108*, 19001–19005.

(331) Style, R. W.; Peppin, S. S. Crust formation in drying colloidal suspensions. *Proc. R. Soc. A* **2011**, *467*, 174–193.

(332) MacMinn, C. W.; Dufresne, E. R.; Wettlaufer, J. S. Large Deformations of a Soft Porous Material. *Phys. Rev. Applied* **2016**, *5*, 044020–044048.

(333) Gumuscu, B.; Haase, A. S.; Benneker, A. M.; Hempenius, M. A.; van den Berg, A.; Lammertink, R. G. H.; Eijkel, J. C. T. Desalination by electrodialysis using a stack of patterned ion-selective hydrogels on a microfluidic device. *Adv. Funct. Mater.* **2016**, *26*, 8685–8693.

(334) Marbach, S.; Bocquet, L. Active osmotic exchanger for efficient nanofiltration inspired by the kidney. *Phys. Rev. X* **2016**, *6*, 031008–031017.

(335) Oglecka, K.; Sanborn, J.; Parikh, A. N.; Kraut, R. S. Osmotic gradients induce bio-reminiscent morphological transformations in giant unilamellar vesicles. *Front. Physiol.* **2016**, *3*, 120–131.

(336) Chabanon, M.; Ho, J. C. S.; Liedberg, B.; Parikh, A. N.; Rangamani, P. Pulsatile lipid vesicles under osmotic stress. *Front. Physiol.* **2016**, *112*, 1682–1691.

(337) Stroka, K. M.; Jiang, H.; Chen, S.-H.; Tong, Z.; Wirtz, D.; Sun, S. X.; Konstantopoulos, K. Water Permeation Drives Tumor Cell Migration in Confined Microenvironments. *Cell* **2014**, *157*, 611–623.